PHD

Nonlinear Dynamics of Neural Circuits

Taylor, Joseph

Award date:
2020

Awarding institution:
University of Bath

Nonlinear Dynamics of Neural Circuits

Joseph D. Taylor

A thesis presented for the degree of Doctor of Philosophy

Department of Physics
University of Bath
United Kingdom
November 2020

Declaration of authorship

I am the author of this thesis, and the work described therein was carried out by myself personally, with the exception of contributions noted in the acknowledgements.

Candidate's signature:

Abstract

This thesis describes the development of a data assimilation methodology for building single-neuron conductance models. Data assimilation seeks to determine unmeasured states and parameters of experimental systems from observable macroscopic quantities. Here, we attempt to estimate parameters governing unobserved ionic transport at the molecular level from observed membrane voltage recordings. We implement a variational assimilation method that uses constrained nonlinear optimization to synchronize the output of neuron models to observed time series data.

When using real-world data, measurement noise and model error can impede the identification of the optimal parameter solution. We present a regularization method that improves convergence towards this optimal solution when data are imperfect and the model is unknown, and derive the conditions under which this optimal solution is obtainable. This method is then applied to the construction of hardware neuron models comprising equations of intracellular currents embodied in analog solid-state electronics. We successfully transfer the complete dynamics of hippocampal and respiratory neurons into silicon devices which are found to respond nearly identically to their biological counterparts under a wide range of current stimulation protocols.

These solid-state models are used to construct inhibitory neural circuits, and the dependence of network dynamics on synaptic parameters in these circuits is quantitatively characterised. The single-neuron parameter estimation developed in the first part of the thesis is finally extended to the construction of inhibitory neuronal networks. To overcome the challenges associated with optimizing a whole-network model, we develop a novel phase reduction approach that allows each neuron in the network to be optimized individually. This work further expands the applicability of variational assimilation to complex neuronal systems.

Acknowledgements

First, many thanks go to my supervisor Alain Nogaret for the dedicated guidance and support. His feedback throughout the project, including on this thesis, was invaluable. Thank you to the EPSRC, to the Department of Physics, and to the University of Bath for making this work possible.

Sincere thanks go to to my co-workers and friends at the University of Bath: members of my research group, other graduate students and postdoctoral researchers, whose good humour and great company have made the Ph.D. journey such a blast. Many of the collaborators who worked on the research presented here are cited in the publications list, but special thanks must go to Ashok Chauhan, Kamal Abu-Hassan, and Paul Morris, whose fun and productive collaborations were central to obtaining much of the data required for this work.

Finally, and above all, heartfelt thanks to the Taylor family for your eternal support. This thesis is dedicated to Grandma Pat, whose love and encouragement in all my endeavours was a source of motivation to the end.

Contents

List of Abbreviations and Glossary of Terms

Abbreviations

aCSF artificial cerebrospinal fluid

AHP afterhyperpolarization

CaT T-type calcium current

CMOS complementary metal-oxide-semiconductor

CPG central pattern generator

DAQ data acquisition

ECG electrocardiogram

FS fast-spiking interneuron

GHK Goldman-Hodgkin-Katz

HCN hyperpolarization-activated cyclic nucleotide–gated

HCO half-center oscillator

HH Hodgkin-Huxley

ING interneuron network gamma

ISI inter-spike interval

ML Morris-Lecar model

MOSFET metal-oxide semiconductor field-effect transistor

NaP persistent sodium current

NaT transient sodium current

NMRSD normalized root-mean-squared deviation

P postnatal day

PDF posterior distribution function

PING pyramidal interneuronal network gamma

RN respiratory neuron

RSA respiratory sinus arrythmia

RVLM rostral ventrolateral medulla

SOM somatostatin-expressing neuron

SSN solid-state neuron

VLSI very large-scale integration

Glossary of Terms

Action potential: a sudden and transitory rise and fall in the voltage across the neuron membrane due to transmembrane ion flow.

Attractor: a stable fixed point in the state space of a dynamical system towards which system trajectories tends to evolve.

Central pattern generator: a neuronal network that produces an oscillating, rhythmic output even in the absence of sensory feedback.

Cost function: a function that measures the misfit of a model to the target data. Data assimilation seeks minima of the cost function.

Data assimilation: a method in which observed data are combined with the output of a numerical model to produce an optimal estimate of the underlying evolving state of the system.

Depolarization: a positive change in membrane potential resulting either from increased permeability to ions or to positive injected current.

Global / local minima: a local minimum of a function is a point where the function is smaller than at all neighboring points. The lowest possible value of the function is called the global minimum.

Hodgkin-Huxley model: a mathematical model of ion current flow through selective channels in the neuron membrane.

Hyperpolarization: a negative change in membrane potential resulting either from increased permeability to ions or to negative injected current.

Identifiability: a model is identifiable if it is theoretically possible to identify the true values of the model parameters from a observations of the model output.

Inhibition: a synaptic mechanism in which a presynaptic neuron makes a postsynaptic neuron less likely to generate an action potential.

Inverse problem: a problem that consists in using the results of measured observations to infer the values of the parameters characterizing a system.

Ion channel: pore-forming proteins that allow selected ions to pass through the neuron membrane.

Lagrangian multipliers: constants λ used to find extrema of a multivariate cost function $f(x)$ subject to constraints $g(x)$. The minimum of $f(x)$ will always correspond to saddle points of the Lagrangian function $\mathcal{L}(x, \lambda) = f(x) - \lambda g(x)$.

Lorenz system: a toy model of the Rayleigh-Bénard convection. A canonical chaotic dynamical system.

Lyapunov exponent: characterises the average exponential rate of divergence of arbitrarily close trajectories in the state space of a dynamical system.

Membrane potential: the difference in electrical potential between the inside and outside of a neuron.

Morris-Lecar model: a two-dimensional reduced neuron model comprising two non-inactivating voltage-sensitive conductances and a passive leakage current.

Neuromorphic engineering: the field of research that attempts to build biologically realistic models of neural systems in electronic circuits. Often implemented using VLSI technology.

Non-convex optimization: the problem of maximizing or minimizing a non-convex function over a potentially non-convex set. Unlike in convex optimization, local minima are not necessarily global minima.

Observability: a measure of the extent to which internal dynamical states of a system can be inferred from observations of the model output.

Phase resetting curve: a function that tabulates how much a perturbing input advances or delays the next cycle length of a running oscillator as a function of where in the cycle it is received.

Regularization: a method used for smoothing the surface of a cost function through the addition of penalty terms to the optimization problem.

Respiratory sinus arrhythmia: a physiological phenomenon in which heart-rate varies in synchrony with the respiratory cycle.

Reversal potential: the equilibrium potential difference generated by differential concentrations of an ion on either side of a membrane that is perfectly selective for that ion.

Saddle-node bifurcation: a quantitative change in the state space of a dynamical system caused by the collision and disappearance of two equilibria.

Sloppiness: the extent to which model behaviour is insensitive to changes in the values of its underlying parameters.

Synapse: the signalling junction between two neurons where nerve impulses are transmitted and received by diffusion of a neurotransmitter.

Takens' Theorem: delay embedding theorem stating that information about hidden states of a dynamical system can be preserved in a time series output.

Chapter 1

Introduction

The aim of this chapter is to highlight the most important concepts that form the motivation for the work presented in this thesis. In particular, we discuss the difficulties associated with parameter estimation of neuron models and give a brief overview of the state of the art in the field. We describe how the results in each chapter of this thesis address several open questions in the neuroscience literature, and give a brief outline of the techniques that we have developed to overcome these challenges. Finally, we present a road map for the rest of the thesis.

1.1 Motivation

Neurons in the brain communicate with each other by transmitting sequences of electrical pulses called ‘spikes’ or ‘action potentials’, a rapid rise and fall in the voltage across the neuron membrane [1]. The effort to understand the mechanisms underlying these complex patterns of spiking activity remains one of the major challenges of neuroscience today [2]. The scientific understanding of neurons and of nervous system function became increasingly precise during the 20th century. In 1952, Alan Lloyd Hodgkin and Andrew Huxley presented a mathematical model for transmission of electrical signals in neurons of the giant axon of the squid, for which they received the Nobel Prize in Physiology or Medicine in 1963 [3, 4]. The Hodgkin–Huxley model gave the first quantitative description of how action potentials were initiated and propagated through the interaction of sodium and potassium currents crossing the cell membrane [5]. In recent years, this model has been generalised to comprise the wider family of ‘conductance-based models’ which may now consider as many as tens of interacting ionic currents [6–8].

Building complex neuron models typically involves a trade-off between biological realism and tractability: the more accurate the neuron model, the more difficult the computational task of tuning the model parameters becomes [9, 10]. The number of interacting parameters can increase into the hundreds for biophysically realistic conductance models, making hand-tuning a near impossible task [11, 12]. Instead, this process must be automated and often involves optimizing an objective function that measures the accuracy of the model as compared to observed data [13, 14]. The choice of criteria by which model performance is judged is user-specific, and can range from correct prediction of spike height or spike width [13, 15, 16] to accurately reproducing the neuron firing rate or precise spike timing [17–19]. Recent work has compared electrophysiological traces in a more direct manner, seeking the global minimum of a least-squares objective function describing the difference between the data and the model membrane voltage traces [20–23]. This approach is underpinned by the Takens-Mañé theorem which states that under certain conditions the full dynamical state of a model may be reconstructed from scalar measurements of the model output alone [24, 25]. The challenging nature of this high-dimensional, simultaneous parameter estimation problem is well known [26–28], and arises due to two primary factors: nonlinearity of the system of equations describing the dynamics of the model; and non-convexity of the least-squares objective function used to describe goodness of fit, which can result in an abundance of sub-optimal local minima in the large parameter space [29, 30]. A further complication relates to the observation that conductance-based neuron models with substantially different sets of parameters may display very similar membrane voltage waveforms under normal conditions [12, 31–33]. It has recently been argued that is therefore impossible to obtain a single set of parameters that“perfectly” replicate experimental data [31, 34, 35]. These observations then raise the question of whether neurons with similar parameters can nonetheless be forced to respond differently with sufficiently discriminating stimulation. In Chapter 3, we address these issues. We use nonlinear optimization to successfully infer the parameters of complex conductance-based models, and demonstrate that the optimal solution, among all others producing equivalent model output, can be identified under appropriate external stimulation. We also explore the effects of experimental error and model error on the parameter solutions, and show that measurement noise can be harnessed to improve convergence to the global minimum of the objective function. In doing so, we improve on both the success rate and on the accuracy of previously-reported parameter estimation of numerical conductance-based neuron models [23].

Neuron models are typically formulated as sets of coupled differential equations whose size is a function of model complexity [36]. For simpler models, their quantitative behaviour can easily be simulated numerically [37, 38], but in the case of more complex models, or large networks of neurons, the computation necessary for simulation can quickly become intractable [39, 40]. The field of neuromorphic engineering seeks an alternative approach, mimicking the structure and emulating the function of neural systems in a physical, typically silicon, form [41–43]. Hardware implementations of neuron models, unlike numerical simulations, operate in real-time and are highly scalable, removing the need for compromise on model complexity or network size [44, 45]. However, complex hardware models face similar challenges associated with estimating optimal parameters, which has driven the use of simplified models in the field [46–49]. Although these models are less exact from a biophysical point of view, they have fewer parameters, rendering parameter estimation feasible [50, 51]. However, bioelectronic medicine is now driving the need for neuromorphic microcircuits that integrate real-time biofeedback and respond identically to biological neurons, a task which demands neuron models that emulate the complex dynamics of particular cells [52–54]. In Chapter 4, we answer this need by designing a biophysically plausible hardware neuron. We derive the equations of intracellular currents and membrane voltages that this silicon model embodies, then use the parameter estimation approaches developed in Chapter 3 to transfer the complete dynamics of a hippocampal and a respiratory neuron in-silico. The solid-state neurons respond nearly identically to their biological counterparts.

In Chapter 5, we provide an example of how the development of neuromorphic systems can answer outstanding questions in experimental neuroscience. Synchronized firing activity has been observed in many central nervous systems, but its underpinning mechanisms and neurobiological function remain a topic of debate [55, 56]. Experimental studies continue to provide growing evidence of a close relationship between synchronous firing activity in the brain and a wide range of cognitive functions [57] including focused attention [58, 59], maintenance of contents in short term memory [60], and the integration of sensory input [61, 62]. Many neuronal populations have been observed to host synchronized firing behaviour [63–65], with associated studies showing that this coherence is primarily due either to excitatory synaptic coupling or to electrical coupling mediated by gap junctions [66]. Indeed, *inhibitory* synaptic connectivity has classically been considered as a mechanism promoting antisynchronous firing [67, 68]. Recent work, however, has found synchronous networks of interneurons in the hippocampus and the cortex that are coupled purely by inhibitory synapses [69, 70], experimentally confirming the existence of inhibition-driven synchrony. In this chapter, we build small networks of inhibitory silicon neurons and explore the underlying mechanisms that may give rise to inhibitory-based synchronization. By making use of the real-time behaviour of neuromorphic devices, we are able to simulate hundreds of network configurations across a wide range of parameters. The use of experimental networks allows us to demonstrate the robustness of synchronized network states to noise, and we find that delays in synaptic inhibition act to stabilise these states, a result which is consistent with observed transmission line delays in synchronizing cortical networks [71]. Furthermore, we conclude that the dynamics of mutually inhibitory neuronal networks are fiercely dependent on synaptic parameters, a fact which explains the challenging nature of parameter estimation for neural circuits [72].

This final point motivates the last results chapter of this thesis. Chapter 6 focuses on the estimation of circuit parameters in networks known as central pattern generators (CPGs). The neurons in these networks produce precisely-timed electrical bursts that are phase-locked with one another and typically drive rhythmic motor behaviors such as respiration and heartbeat [73, 74]. The study of CPGs constitutes an active area of research [75, 76] which has confirmed that the relationships among neuron and synapse parameters in these networks are highly nonlinear [77]. This particular fact constitutes a major obstacle to designing artificial CPGs with desired phase lags. In this chapter, we propose a solution to this challenge by describing a novel parameter estimation method that first reduces the constituent neurons of the CPG to their individual phase resetting curves (PRCs) [78]. PRCs keeps track of how much a synaptic input advances or delays the next burst in an oscillating neuron as a function of where in the burst cycle the input is received [79]. We show that problems concerning phase-lags between the neurons in the network can be reduced to problems concerning individual neuron PRCs. This reduction technique allows each oscillator to be optimized entirely separately such that it possesses the required PRC, enabling the estimation of all neuron and synapse parameters of the network while avoiding the challenges associated with searching the high-dimensional parameter space of a whole-network model.

1.2 Thesis structure

Chapter 2 covers the theoretical background needed to arrive at the results presented in the thesis, beginning with an overview of neuron electrophysiology and conductance-based neuron models. This is followed by a description of the parameter estimation approach used throughout this work. Chapters 3-6 of the thesis are organised into two main parts on the basis of general themes. Part I (Chapters 3-4) covers the optimization of neuron models at the single-neuron level. The first chapter discusses parameter estimation of biophysical conductance-based models, while the subsequent chapter utilises a similar approach to build predictive solid-state neurons. Part II of the thesis (Chapters 5-6) concerns neuronal dynamics at the network level. Chapter 5 uses solid-state neurons to probe the dynamics of small inhibitory neuronal networks, and Chapter 6 applies the parameter estimation methods developed in Part I to the construction of small network models. Finally, Chapter 7 presents some general conclusions and suggests some potential research directions for future work.

1.3 Papers and presentations

The work detailed in this thesis has contributed to four published papers and two conference presentations. The papers are:

- *Dual mechanism for the emergence of synchronization in inhibitory neural networks* (2018) by A.S. Chauhan, J.D. Taylor, and A Nogaret, published in *Scientific Reports* [80]

- *Optimal solid state neurons* (2019) by K. Abu-Hassan, J.D. Taylor, P.G. Morris, E. Donati, Z.A. Bortolotto, G. Indiveri, J.F.R. Paton, and A. Nogaret, published in *Nature Communications* [81]

- *Estimation of neuron parameters from imperfect observations* (2020) by J.D. Taylor, S. Winnall, and A. Nogaret, published in *PLOS Computational Biology* [23].

- *Robust design of inhibitory neuronal networks displaying rhythmic activity.* (2021) by J.D. Taylor, K. Abu-Hassan, J.J.A. van Bavel, M.A. Vos, and A. Nogaret, published in *Dynamical Systems Theory and Applications* (*in preparation*).

Posters were presented and presentations given at the Conference for Complex Systems 2019 meeting (NUT, Singapore) and the 2019 Dynamical Systems - Theory and Applications conference (Łodz, Poland).

Chapter 2

Background and Methods

A primary focus of this thesis is the construction of conductance-based neuron models whose free parameters need to be constrained using empirical data. In this chapter, we begin with an overview of the biophysics of neuron membranes, highlighting the parameters of interest that we seek to estimate, before introducing the Hodgkin-Huxley model and its subsequent extensions. The second part of the chapter expands on the methodology underlying data assimilation, the parameter estimation approach used to constrain these models, and outlines some of the challenges posed by nonlinear inverse problems in neuroscience. The chapter ends with details of the assimilation implementation that we use throughout the thesis to build predictive neuron models, highlighting some improvements on previously reported methods.

2.1 Neurobiology background

2.1.1 Neuron membranes

The fundamental unit of electrical signalling in the nervous system is the action potential, an abrupt spike in the membrane voltage of the neuron. These electrical pulses are generated by ion flow across the membrane of the cell body or 'soma'. Neuron membranes, like those of other cells, act to separate the cell interior and its external environment. Both the intracellular and extracellular fluid contain high concentrations of dissolved ions such as sodium (Na^+), potassium (K^+), calcium

(Ca^{2+}), and chloride (Cl^-), but the concentration of each ion species inside the cell is different to that in the surrounding liquid [82]. In mammalian neurons, the extracellular medium typically has a high concentration of positively charged Na^+ and Ca^{2+} ions, and a high concentration of negatively charged Cl^- ions. The intracellular fluid, on the other hand, has a high concentration of positively charged K^+ ions [83]. These differentials cause concentration gradients to form across the cell membrane, which acts as a leaky capacitor: while the membrane itself is a nearly perfect electrical insulator - a lipid bilayer with a typical resistance of 100-300 MΩs [84] - large proteins embedded in the membrane form pores connecting the cell interior and exterior [85]. These proteins act as ion gates, allowing specific ions to pass from one side of the membrane to the other. Some of these gates, known as ion pumps, maintain the ion concentrations on either side of the cell membrane through the active transport of ions across it [86]. A second type of ion gate, known as an ion channel, facilitates passive transport, and can be in either an 'open' or a 'closed' state [82]. When in the 'open' state, they allow ions to diffuse across the cell membrane (Fig. 2.1). Ion channels have the important property of being 'ion-selective'; that is, they only allow a restricted class of ions to pass. They are generally named according to this selectivity; for example, channels that allow only Na^+ diffusion are referred to as being 'Na^+-selective'. Many kinds of ion channels have been identified [87], and the expression of particular channels may vary widely even among cells of the same type [88, 89]. It is not generally possible to know *a priori* which ion channels are present in a given cell. This fact informs a large part of the discussion in Chapter 4, where we estimate the parameters of a conductance model using real, biological neurons from the hippocampus and the brain stem. A useful advantage of the data assimilation approach that we describe in this thesis is that it automatically assigns a null value to the conductances of any channels in the model that are not present in the neuron [21, 22]. We find that a generic conductance model can therefore be used to fit the behavior of different classes of neurons, removing the requirement of prior information and biological intuition of previous approaches [90].

There are two primary forces that drive diffusion through ion channels: concentration gradients and electrical potential gradients. Ions tend to flow down their concentration gradients, from regions of high concentration to regions of low

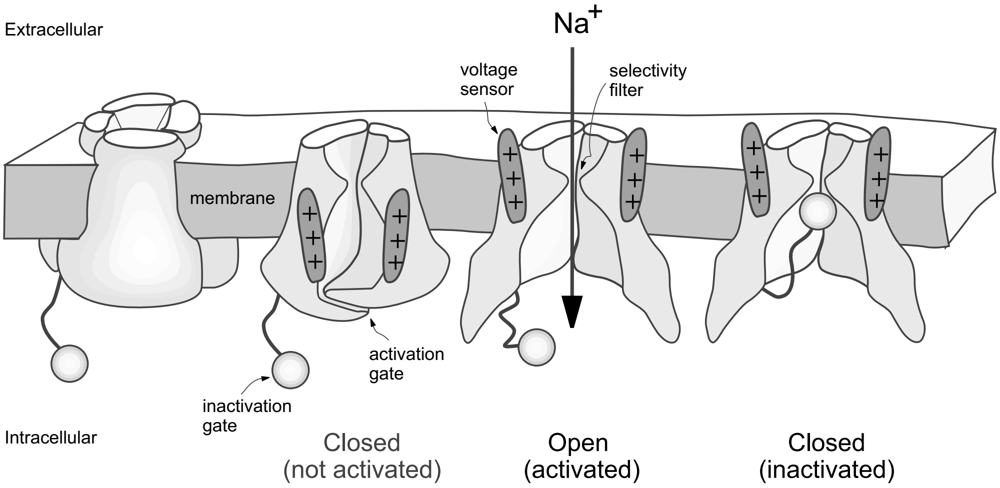

Figure 2.1: Voltage-gated ion channels. When the membrane potential is at the threshold voltage for the channel, an activation gate opens and allows particular ions to flow through the channel down their electrochemical gradients. After a delay determined by the ion channel kinetics, an inactivation gate blocks the channel. (Modified from Ref. [91])

concentration. Table 2.1 shows some typical ionic concentrations across a neuron membrane. Positive charges outside the cell and the negative charges inside the cell accumulate on opposite sides of the neuron membrane, creating an electrical potential gradient across it. We call this the transmembrane potential, or *membrane voltage*, denoted V. At rest, most mammalian neurons sit at a membrane voltage of ~ -70 mV. We shall see in Chapter 4 that this value varies across neuron types, and is one of the defining properties of a neuron that we seek to estimate. For a given ionic species, ion flow across the membrane will continue until the driving force of the concentration gradient is counterbalanced by the electric potential gradient provided by the membrane voltage, upon which an equilibrium is reached. The membrane voltage corresponding to this equilibrium depends on the ion species in question, and is given by the Nernst equation [92, 93]:

$$E_{\text{ion}} = \frac{RT}{zF} \ln \frac{[\text{Ion}]_{\text{o}}}{[\text{Ion}]_{\text{i}}} \qquad (\text{mV}) \tag{2.1}$$

where R is the universal gas constant (8.3145 J$\cdot mol^{-1}\cdot$K^{-1}); T is temperature in Kelvin; F is Faraday's constant (96,485 C$\cdot mol^{-1}$); z is the valence of the ion

Table 2.1: Typical ion concentrations and reversal potentials in mammalian neurons [82].

Ion	Extracellular Concentration (mM)	Intracellular concentration (mM)	$[\text{Ion}]_\text{o}/[\text{Ion}]_\text{i}$	Equilibrium potential (mV)
Na^+	145	12	12	+67
K^+	4	155	0.026	-98
Ca^{2+}	1.5	100 nM	15,000	+129
Cl^-	123	4.2	29	-90[a]

---

[a] Reversal potentials were calculated using the Nernst potential equation (Eq. 2.1)

species; and $[\text{Ion}]_\text{o}$ and $[\text{Ion}]_\text{i}$ are the concentrations of the ion species outside and inside the neuron, respectively. In summary, the Nernst, or reversal, potential for a given ion species is the value of voltage across the membrane that exactly balances the concentration gradient of the ion species. In reality, cell membranes are permeable to many species of ion. Typical Nernst potentials E_Na, E_K, E_Ca, and E_Cl for mammalian neurons are summarized in Table 2.1.

It is worth noting that the parameters described in this section correspond to passive properties of the neuron membrane. While reversal potentials, membrane capacitance, and leakage properties of the cell can be characterised with electrophysiology, there have been a number of successful attempts to infer these parameter values from the membrane voltage observations alone. Estimating these particular parameters, however, is a linear problem. Indeed, in Chap. 3, we find that these are the parameters that are best-constrained by our data assimilation approach. The more difficult nonlinear problem of estimating the parameters governing ion channel kinetics has historically proven challenging [94, 95]. However, in later chapters we demonstrate the ability of our approach to correctly identify these parameters, too. We quantify the error on these estimates, finding the parameters governing ion channel kinetics to be the least well-constrained. In the next section, we discuss the function of these nonlinear parameters in detail.

2.1.2 Ionic channels and currents

The flow of ionic currents across the membrane is governed by a number of factors: the membrane voltage, the reversal potentials of the ion species, and the conductance of their associated ion channels. The net transmembrane current for a given ion species at any given moment can be calculated using the following equation:

$$I_{\text{ion}} = g_{\text{ion}}(V - E_{\text{ion}}), \tag{2.2}$$

where the quantity $(V - E_{\text{ion}})$ is referred to as the driving force, and g_{ion} (mS/cm^2) is the conductance of the neuron membrane with respect to that ion. Generally speaking, these conductances are not constant, but rather time- and voltage-dependent. It is this property in particular that enables the neuron membrane to generate information-encoding electrical pulses. The conductance of an individual channel is controlled by particles called 'gates' which switch the channel between these open and closed states (Fig. 2.1). Depending on the type of gating particle present, these channels can be sensitive to any of the following factors:

- **Membrane potential**: these channels are typically described as being 'voltage-gated'. Their open-closed state is determined by the value of the neuron membrane potential. The two most common channel types in mammalian neurons are voltage-gated Na^+ and K^+ channels.

- **Intracellular chemicals**: the state of these channels is determined by the presence of particular chemical agents inside the cell. One example is the class of Ca^{2+}-gated K^+ channels, which transition from a closed to an open state in the presence of intracellular calcium.

- **Extracellular chemicals**: these channels are described as being 'ligand-gated'. They open in response to the binding of a chemical messenger (or 'ligand'), such as a neurotransmitter.

Even though any individual ion channel may only be either open or closed, the net current flowing through a large population of identical channels may be described as $I = \bar{g}p(V - E)$, where p is the fraction of channels in the population that are in the open state, $\bar{g}$ is the *maximal conductance* of the ensemble, i.e., the conductance when *all* channels are in the open state ($p = 1$), and E is the reversal potential for the current. The gates that determine the transition of these channels from the closed state to the open state are divided into two kinds: *activation* gates, and *inactivation* gates. We denote the probability of an activation gate being in the open state by the variable m, and denote the probability of an inactivation gate being in the open state by h. The fraction of open channels in a large ensemble is therefore given by $p = m^a h^b$, where a corresponds to the number of activation gates per channel and b to the number of inactivation gates. It should be noted that some classes of ion channel do not inactivate ($b = 0$) and their associated currents are termed *persistent*. Ionic currents associated with channels that do inactivate are termed *transient*. The dynamics of the (in)activation variables $x \in \{m, h\}$ are described by a first-order differential equation:

$$\dot{x} = (x_\infty(V) - x)/\tau_x(V), \tag{2.3}$$

where $x_\infty(V)$ is a voltage-dependent steady-state function which gives the asymptotic value of x for a given membrane potential, and $\tau_x(V)$ is the time constant which determines the speed with which x tends towards the asymptotic value. Smaller values of the time constant $\tau_x(V)$ result in faster current activation. The steady-state function is sigmoidal in shape, while the time constant follows a bell-curve (Fig. 2.2). The exact form of these steady-state and time course curves can be measured experimentally and incorporated into neuron models [97]. Traditionally, this has been done using voltage-clamp electrophysiology, in which a variety of pharmacological blockers are applied to groups of neurons in order to tease out intrinsic currents that contribute to neuron signalling [98, 99]. Due to the pharmacological manipulations required, it is typically the case that a single neuron provides information on only one current, requiring that models built using these data take parameter values averaged over a population of cells. Averages of measured parameters in nonlinear systems often give rise to non-observed behavior, since average values may not be valid parameter combinations themselves [100]. Furthermore, outside of a few well-studied classes of neurons, these parameters have not yet been measured. The slopes and magnitudes of the curves in Fig. 2.2 vary between ion channel types and across individual neurons, and in the later

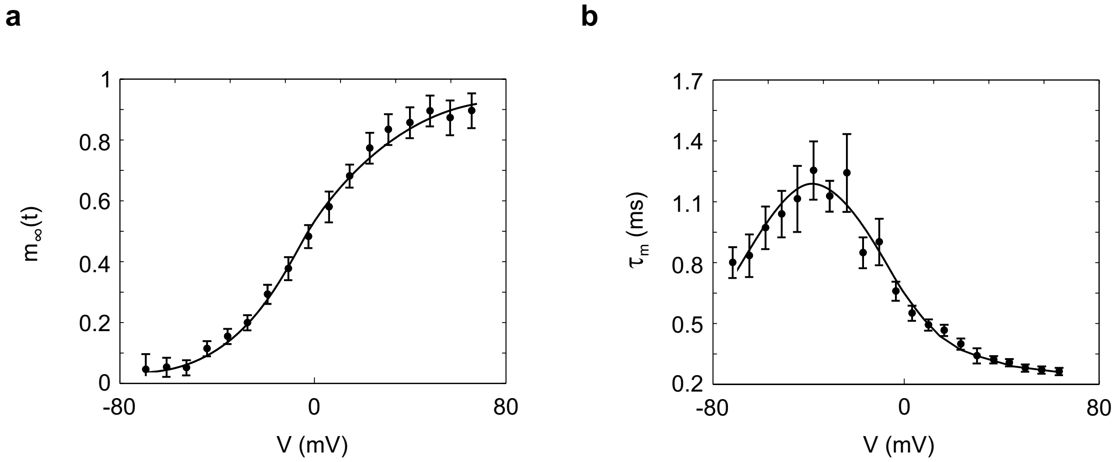

Figure 2.2: Experimentally-derived activation function $m_\infty(V)$ and time constant $\tau_m(V)$ of the fast transient K^+ current in layer 5 neocortical pyramidal neurons. These data are obtained from voltage-clamp measurements in which additional currents have been pharmacologically blocked. (Data from Ref. [96].)

chapters of this thesis, our goal is to estimate these quantities from observations of the membrane voltage alone, which, unlike channel parameters, is a relatively trivial quantity to measure. Many recent attempts to estimate these nonlinear parameters from membrane voltage observations have been limited to small conductance models that often fail to give better predictions than phenomenological models [19, 101]. In contrast, the nonlinear optimization approach detailed in this thesis has been shown to be effective at inferring parameter values for both linear and nonlinear parameters [20, 22, 23].

2.2 Conductance-based neuron models

Conductance-based neuron models are derived from an equivalent circuit representation of a cell membrane in which its protein molecule ion channels are represented by conductances and its lipid bilayer by a capacitor [3]. In these models, the soma of the neuron is represented by a single isopotential electrical compartment whose membrane potential changes as a function of transmembrane currents. According to Kirchhoff's current conservation law, the total current, I, flowing across a neuron membrane is equal to the sum of the ionic currents ($I_{\rm Na}$, $I_{\rm K}$, $I_{\rm Ca}$, $I_{\rm Cl}\ldots$)

and the displacement current $C\dot{V}$ (the current associated with the charging of the membrane), or equivalently

$$I = C\dot{V} + I_{\mathrm{Na}} + I_{\mathrm{Ca}} + I_{\mathrm{K}} + I_{\mathrm{Cl}} + \ldots, \tag{2.4}$$

where C is the specific membrane capacitance (1.0 μF/cm^2). The quantity I denotes all non-ionic currents flowing across the cell membrane, such as current injected via an electrode, synaptic currents, or currents leaking from other compartments of the neuron.

2.2.1 Hodgkin-Huxley model

The first conductance-based model was formulated by researchers Alan Hodgkin and Andrew Huxley [3] to explain the ionic mechanisms underlying the initiation and propagation of action potentials in the squid giant axon. The Hodgkin-Huxley model incorporates three types of ion current, a transient Na$^+$ current, a persistent K$^+$ current, and a leak current consisting mainly of Cl$^-$ ions, each of which has a corresponding ion channel. Using voltage-clamping techniques, Hodgkin and Huxley found that the states of the Na$^+$ channels in the squid axon were controlled by three activation gates (m^3) and a single inactivation gate (h), while the states of the persistent K$^+$ channels were controlled by four activation gates (n^4). The leak current was found to flow through passive (non-dynamic) channels. The state of the neuron in this model is therefore described by the values of four time-dependent variables: the membrane voltage V, the sodium activation gate m, the sodium inactivation gate h, and the potassium activation gate n. The evolution of this system is described by the following set of equations:

$$C\dot{V} = I - \overbrace{\bar{g}_{\mathrm{Na}} m^3 h (V - E_{\mathrm{Na}})}^{I_{\mathrm{Na}}} - \overbrace{\bar{g}_{\mathrm{K}} n^4 (V - E_{\mathrm{K}})}^{I_{\mathrm{K}}} - \overbrace{g_L (V - E_{\mathrm{L}})}^{I_{\mathrm{L}}} \tag{2.5}$$

$$\begin{aligned} \dot{m} &= (m_\infty - m)/\tau_m(V) \\ \dot{h} &= (h_\infty - h)/\tau_h(V) \\ \dot{n} &= (n_\infty - n)/\tau_n(V) \end{aligned} \tag{2.6}$$

where

$$\alpha_\infty = \frac{1}{2}\left(1 + \tanh\frac{V - V_{t\alpha}}{\delta V_\alpha}\right), \qquad \tau_\alpha = t_\alpha + \epsilon\left(1 - \tanh^2\frac{V - V_{t\alpha}}{\delta V_{\tau\alpha}}\right) \tag{2.7}$$

for the gating variables $\alpha \in \{m, h, n\}$. C is the specific membrane capacitance, and I is the external injected current (nA/cm^2). The shapes of the steady-state curves (Fig. 2.2a) are determined by the parameters $V_{t\alpha}$ and δV_α, which correspond to the threshold and the slope of the sigmoid function, respectively. The time constant bell-curve (Fig. 2.2b) is determined by the parameters $V_{t\alpha}$ and $\delta V_{\tau\alpha}$ - which correspond to the center and half-width-at-half-maximum of the curve, respectively - in addition to the parameters t_α and ϵ_α which determine the magnitude of the time constant. Fig. 2.3 shows some time series associated with the dynamics of the Hodgkin-Huxley model. If a small amount of current $I(t)$ (positive charge) is injected into the neuron via an electrode, the membrane potential can be raised (depolarized). This raising of the membrane potential causes a small efflux of current from the cell, which counteracts the injected current, and pulls the cell back to the resting potential (repolarization). Larger injected currents, however, activate voltage-sensitive ionic currents, which in turn raises the membrane potential further. This positive feedback loop causes the membrane potential to deviate considerably from the resting potential, V_{rest}. This momentary spike in membrane voltage is the action potential, or spike.

2.2.2 Model extensions

Since the publication of the Hodgkin-Huxley model, this general framework has been extended to accommodate the wide variety of ion current types found in biological nervous systems [102, 103], incorporating as many different ion channel types as necessary for the particular cell being modeled. Most biological cells display more complex behaviours than the tonic spiking observed in the Hodgkin-Huxley model, and in the later chapters of this thesis, we model two primary classes of neuron: pyramidal cells in the hippocampus [104], and respiratory cells in the brain stem [105]. In Fig. 2.4, we demonstrate some of the complex behaviours that we observed when recording from these cells, including spike-frequency adapta-

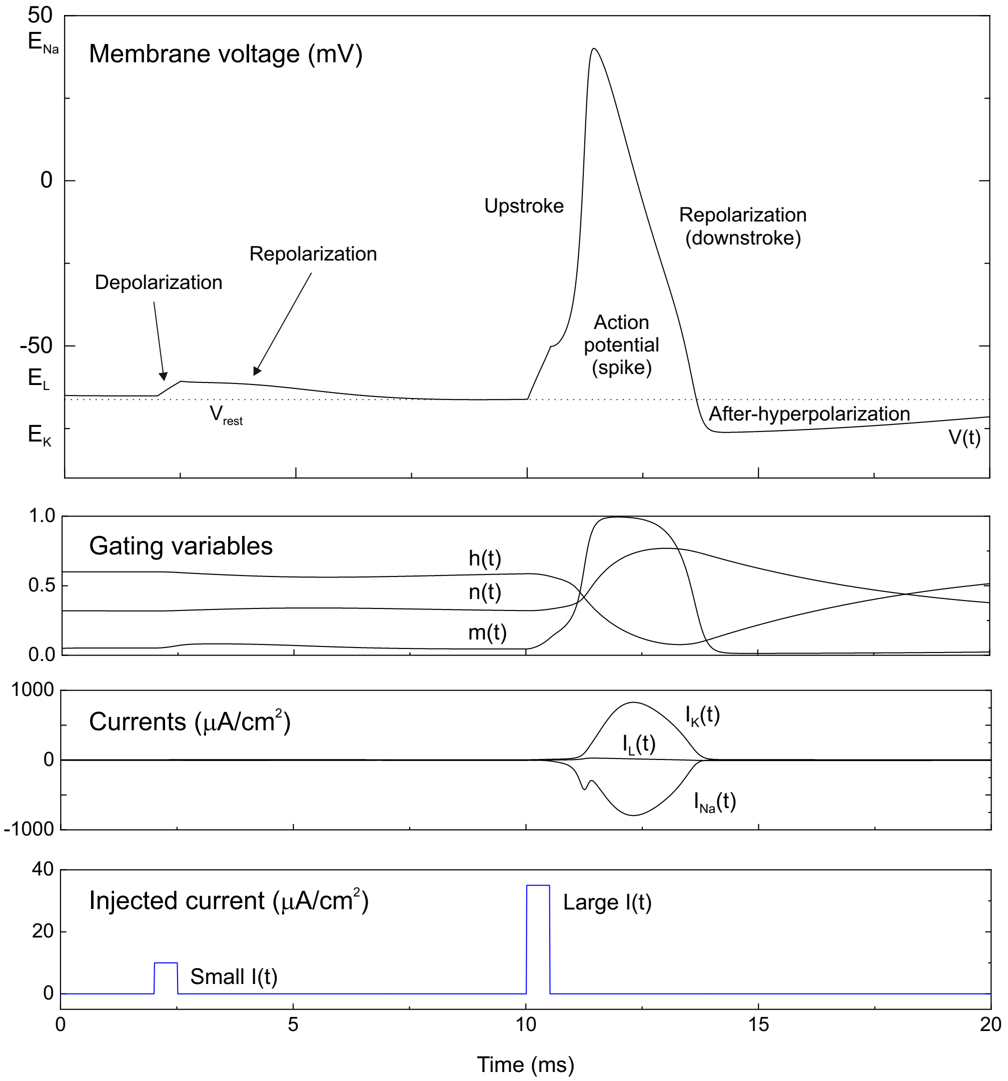

Figure 2.3: Mechanisms underlying the action potential in the Hodgkin-Huxley model. This study of the spike-generation mechanism would later win Alan Hodgkin and Andrew Huxley the 1963 Nobel Prize for physiology or medicine.

tion, spontaneous pacemaking activity, and intrinsic bursting, which the Hodgkin-Huxley model alone cannot reproduce. When constructing models of these cells, it is therefore wise to include additional ionic currents that are thought to underlie these observed behaviours. For example, a common extension found in many conductance-based models is a set of equations describing internal calcium dynamics, the inclusion of which is thought to be necessary for bursting (Fig. 2.4, bottom) and spike frequency adaptation (Fig. 2.4, top) [106]. As mentioned previously, in addition to voltage-dependency, many common ion channels demonstrate a dependence on the internal concentration of calcium which, in many cells, is observed to increase rapidly upon the firing of an action potential [107]. Calcium currents are known to be prominent in the soma and dendrites of neurons such as thalamic relay neurons and cerebellar Purkinje cells [108], and have been demonstrated with voltage-clamp recordings in a variety of central nervous system neurons [109]. Calcium-dependent currents can be modelled to various degrees of complexity depending on the requirements of the model. In Chapter 3, we model Ca^{2+} dynamics using the Goldman-Hodgkin-Katz (GHK) equation [110], while in Chapter 6 we use the simpler framework described in Ref. [111]. It has also been recently shown that the pacemaking behaviour observed in some respiratory neurons (Fig. 2.4, middle) is due to a persistent, non-inactivating sodium current [105]. In Chapter 4, we therefore include this long-lived current in our model to account for the observed spontaneous firing.

Another way in which the Hodgkin-Huxley model has been extended since its original development is through the inclusion of several neuronal compartments that account for the spatial structure of biological neurons [112]. In these multi-compartmental models, the neuron is divided into several compartments representing different parts of the dendrites, soma, and axon. If sufficiently strong stimulation arrives at one of the compartments, an action potential may propagate into the vicinity of neighbouring compartments [113]. One advantage of this approach, among many, is that it allows latency effects of action potential propagation to be modelled, which depend on the excitability of all compartments along the path of propagation [114]. While the parameter estimation methods presented in this thesis can be extended to multi-compartmental neuron models, both the size of the parameter search space and the computational overhead expand significantly [90].

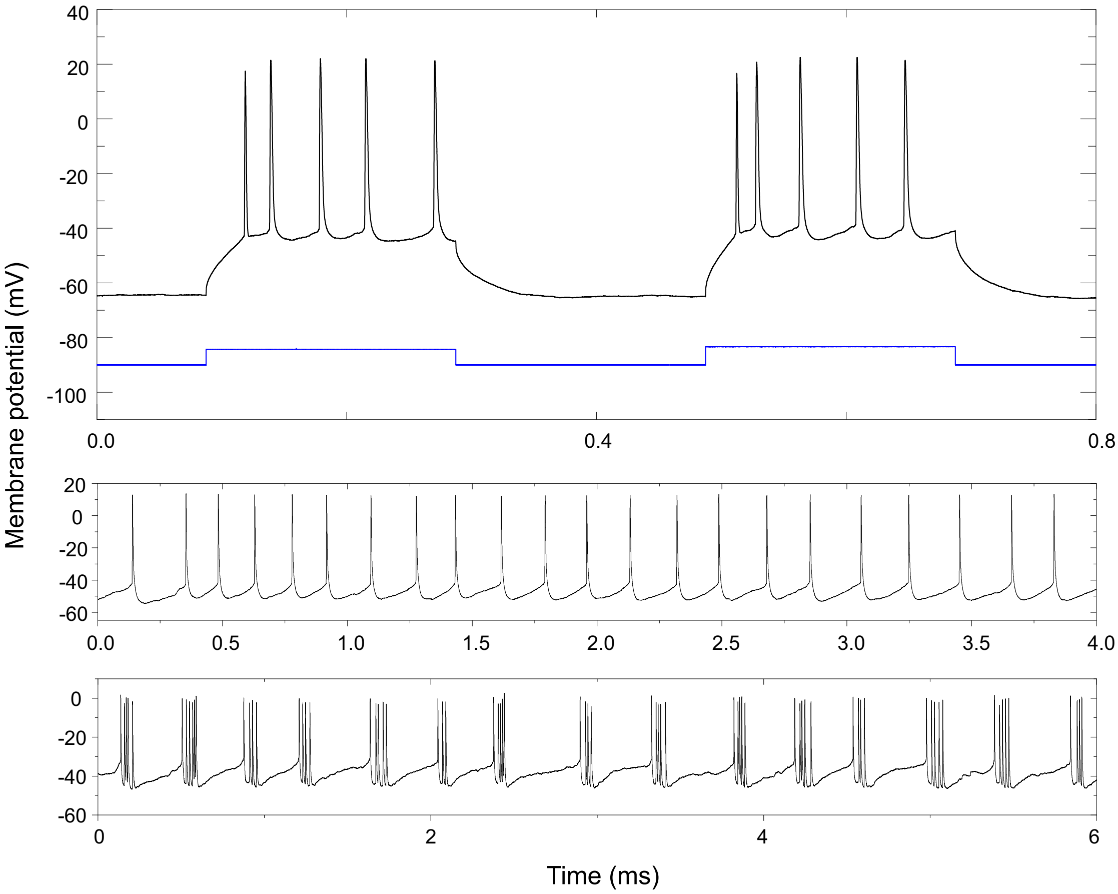

Figure 2.4: Complex behaviours of hippocampal cells and respiratory neurons. (Top) We recorded the response of a CA1 pyramidal neuron to step currents of 200 ms duration and 120 pA amplitude. The neuron fires tonic spikes which broaden in width and display spike frequency adaptation. (Middle) Spontaneous spiking activity (pacemaking) observed in an expiratory neuron in the medulla region of the rat brainstem. Rhythmic firing occurs in the absence of stimulatory input. (Bottom) Intrinsic bursting observed in an inspiratory neuron in the pre-Bötzinger complex of the rat brainstem. Bursting in these cells occurs as a result of the interplay of fast and slow ionic currents, resulting in rapid firing followed by a period of quiescence.

In Chapter 4, we demonstrate that a single-compartment somatic model is sufficient to predict the spiking dynamics of two classes of biological cell. We therefore conclude that the majority of the ionic currents responsible for the electrical activity of these neurons are present in their highest density in the soma. In Chapter 5, however, we model networks of inhibitory neurons and seek to understand the effect of synaptic inhibition received at distal dendrites, far from the neuron soma. We show that the conduction delay associated with this spatial structure can instead be modelled as a delay in the onset of synaptic transmission. In doing so, we manage to incorporate the specific properties of multi-compartmental models that are relevant to us without assuming the significant costs associated with such a full description of the neuron morphology.

2.3 Data assimilation

2.3.1 Introduction

Building a model of a particular complex system requires extracting information derived from measurements or observations of some of its physical properties. These observations are very often incomplete or sparse: not all of the properties of the system are readily accessible to experiment. This challenge of using partial information from the available observed data and transferring it to a model of the system generating those data is termed data assimilation [115–117]. The concept can be more formally stated as follows: over a time interval $[0,\, T]$ observations of *some* properties of a physical system are made at discrete times $t_i = iT/N$, $i = 0, 1, ..., N$. Using prior knowledge of the physical system in question, we can construct a model of its dynamics. This model may be expressed as a set of differential equations (Eqs. 2.5-2.7, for example) which describe how the system evolves through time. The model, as described so far, is said to be *incomplete*. There are many quantities that enter into the model which are as yet unknown. These are the *unobserved* properties of the system, which need to be estimated. In this section, we describe a systematic method for estimating the values of these properties using the observed data on the interval $[0,\, T]$, and thus *completing* the model. The model will typically consist of multiple *state variables*, dynamic quantities that evolve through time, and fixed physical parameters. So, in summary, the goal of data assimilation is to estimate the unobserved parameters and state variables in the observation window $[0, T]$. If we do this well, the full model state (observed and unobserved state variables) will have been estimated. The completed model may then be validated by comparing model predictions with further observed data outside the assimilation window for $t > T$. It is worth briefly considering the reasons why a prediction might go wrong.

- **Observed data is always imperfect**: the overall task of data assimilation is essentially a statistical problem. The data will always be corrupted by some experimental error, such as noise. There is therefore a probability distribution for the model state and parameters, conditioned on the observed data, and one seeks to find the maximum likelihood expectation of these quantities.

- **The model is wrong**: the model may lack a description of important dynamical features present in the system. Additionally, the physical system itself may operate in a noisy environment which is impossible to model.

- **The assimilation procedure is flawed**: it is incapable of extracting information from the data and transferring it to the model. Estimates of parameters and state variables are not equal to those of the true system.

This final point emphasizes the importance of using the dynamical model in a series of so-called "twin experiments". In twin experiments, data are generated with a given model and an attempt is made to recover the known parameters using that data with parameter estimation methods. These experiments are very useful for discovering the number of measurements required for a successful estimation, since they allow the experimenter to compare estimated parameters to ground truth values. In Chapter 3, we use twin experiments to quantify the effects of experimental and model error on parameter solutions in data assimilation problems.

2.3.2 Data assimilation in neuroscience

In recent years, data assimilation has been applied to various areas of neuroscience. For example, it has recently been used to infer spike timings from two-photon calcium imaging [118], and to estimate the connectivity of neuron populations from electro-cortical activity [119]. Data assimilation is particularly relevant to the construction of single-neuron models from biological recordings. These models are often conductance-based, and their equations describe the relationship between unobserved microscopic ionic currents and the macroscopic evolution of the membrane voltage. The dynamics of voltage-gated ion channels drive the observable electrical behaviour of the neuron, but are not themselves readily accessible to experiment. Data assimilation is therefore a good candidate for determining the parameters controlling ion channel kinetics from observations of membrane voltage. The application of data assimilation to the building of single-neuron models can be visualised in the following way. The problem is one of optimization: given a numerical model of the neuron, find the set of parameters and unobserved state variables that most closely reproduce the observed membrane voltage data [116].

A number of attempts have been made to develop methods for estimating parameter values from membrane voltage measurements [11, 100, 120]. These approaches have included stochastic, and evolutionary search algorithms [121], random parameter search [34], simulated annealing [122] and gradient descent methods [20]. The majority of these, however, have sought to estimate maximal conductance parameters; a linear problem. Estimating parameters governing ion channel kinetics is a nonlinear problem, and is thus more challenging. More recently, the parameters and unobserved states of conductance-based neuron models have been successfully obtained using an approach known as variational assimilation. By synchronizing the output of a neuron model to observed membrane voltage data, these methods were able to estimate all free parameters in a conductance model to build quantitative and predictive single-neuron models [22, 23, 81].

2.3.3 Variational assimilation

Variational assimilation is a parameter estimation method based on principles from control theory, observer theory, and synchronization of chaotic systems [116, 123]. It is typically implemented by coupling the output of an experimental system with a model $\mathbf{x}(t)$ of the system, such that the model and the physical system are 'synchronized'. This synchronization is posed as a constrained optimization problem in which a cost function describing the distance between the system output and model output is minimized, subject to the model equations of motion. This minimization problem is typically large and requires high-performance optimization software, such as IPOPT [124] or SNOPT [125] to be solved numerically. The full state $\mathbf{x}(t) = [x_1(t), x_2(t), ..., x_L(t)]$ of a physical system can be described by a set of L state variables, a set of K parameters $\mathbf{p}$, and any external inputs. Typically only a subset M of these quantities can be measured in the physical system ($M < L$). For the inverse problem of estimating neuron parameters from membrane voltage observations, only a single state variable $x_1(t) \equiv V(t)$ is available ($M = 1$). The evolution of the system is described by a set of first-order differential equations:

$$\frac{dx_l(t)}{dt} = F_l(\mathbf{x}(t), \mathbf{p}, t), \quad l = 1, ...L. \tag{2.8}$$

The goal is to find the unmeasured state variables and fixed parameters through the minimization of the least-squares distance between the observed experimental data $V_{\mathrm{exp}}(t)$ and the equivalent model output $x_1(t) \equiv V(t)$. The distance between the membrane voltage state variable of the model and the experimentally observed membrane voltage over the observation window $0 < t_i < T$ is given by the least-squares distance, or 'cost' function

$$\sum_{i=0}^{N} \left(V_{\mathrm{exp}}(t_i) - V(t_i)\right)^2 . \tag{2.9}$$

The true, or "optimal", parameters correspond to the parameter set $\mathbf{p}^*$ for which this distance is minimized. This is equivalently described as finding the *global minimum* of the cost function. Variational assimilation seeks to find this optimal parameter set by gradient descent over a search surface in parameter space. For highly nonlinear systems, the search surface may host many spurious *local* minima corresponding to sub-optimal parameter sets encountered by iterative gradient descent approaches [126, 127]. To partially address this issue, we included a coupling term $u(t)(V_{\mathrm{exp}} - V(t))$ in the neuron model equations of motion, which helps to smooth the search surface by driving synchronization between the model and the data. It works by eliminating positive conditional Lyapunov exponents in the joint model-data system [14, 128]. Since this coupling variable $u(t)$ does not form part of the true model dynamics, we penalize large values of $u(t)$ though its inclusion in the cost function. Thus, as the parameter search reaches the global minimum, $u(t)$ is driven to zero [22, 128]. The full cost function is therefore given by:

$$C(\mathbf{x}(0), \mathbf{p}) = \frac{1}{2N} \sum_{i=0}^{N} \{(V_{\mathrm{exp}}(t_i) - V(t_i, \mathbf{x}(0), \mathbf{p}))^2 + u^2(t_i)\}. \tag{2.10}$$

This cost function is minimized subject to a number of equality constraints, which enforce the model equations of motion between neighbouring time points, and inequality constraints, which consist of upper and lower bounds on the parameter and state variable values. Note that the cost function is normalized according to the length of the observation window, and the dependence of the model voltage $V(t, \mathbf{x}(0), \mathbf{p})$ on the initial model state at $t = 0$ has been made explicit.

2.3.4 Implementation details

The minimization process was performed using the open-source Interior Point OPTimizer (IPOPT) software which is designed for solving large-scale constrained nonlinear optimization problems [124] of the form

$$\min_{x \in \mathbb{R}^n} \quad f(x) \tag{2.11}$$

$$\text{s.t.} \quad g(x) = 0 \tag{2.12}$$

$$x^L \leq x \leq x^U, \tag{2.13}$$

where $f(x)$ is the objective function, $g(x)$ are equality constraints on the optimization, and $x \in \mathbb{R}^n$ are the optimization variables: in our case the state variables at all time points and the global system parameters. The optimization variables are constrained by lower and upper bounds x^L and x^U, respectively, with the model gating variables being bounded between zero and one, and the K free parameters being subject to user-defined upper and lower bounds $p_{k,L} \leq p_k \leq p_{k,U}$, $k = 1, ..., K$. In addition to these inequality constraints, the minimization includes equality constraints $g(x)$ that specify the rate of change of state variables across consecutive time points, as specified by the model equations. IPOPT uses an interior-point line-search method which replaces inequality constraints with a logarithmic barrier term that is added to the objective function, and seeks to minimize the following auxiliary barrier problem

$$\min_{x \in \mathbb{R}^n} \quad \varphi_\mu(x) = f(x) - \mu \sum_i^n \ln(x_i) \tag{2.14}$$

$$\text{s.t.} \quad g(x) = 0. \tag{2.15}$$

For a given value of the barrier parameter $\mu > 0$, the barrier objective function $\varphi_\mu(x)$ goes to infinity if any of the problem variables x_i approach their zero bound. An optimal solution will therefore be in the interior of the region defined by the logarithmic barrier. IPOPT solves a sequence of barrier problems in which $\mu \rightarrow 0$, where the optimal solution of the final problem corresponds to that of the original problem (Eq. 2.11-2.13). The optimizer solves the auxiliary problem by gradient descent using a Newton-Raphson algorithm, seeking extrema, $\nabla f(x) = 0$, of the objective function within the search space bounded by the logarithmic barrier. It is important to note that not only local minimizers, but also some maximizers and saddle points satisfy this criterion. To mitigate this fact, IPOPT requires that the sparsity structure of the constraint Jacobian and the Lagrangian function Hessian be specified prior to computation. The Lagrangian function for the optimization problem is defined as $f(x) + g(x)^T\lambda$ and the Hessian of the Lagrangian function is $\nabla^2 f(x) + \sum_{i=1}^m \lambda_i \nabla^2 g_i(x)$, where λ_i are Lagrangian multipliers [129]. These matrices had to be computed in advance, and were calculated using symbolic differentiation with the custom-built Python library *pyDSI* [23] which takes a simple text file formulation of the model equations and outputs correctly formatted and linked C++ files to be interfaced with IPOPT. Successful optimizations resulted in the output of data files containing estimates for the model parameters and state variables at the final iteration of the optimization. Matrix computations were performed using the MA97 solver library (http://www.hsl.rl.ac.uk/catalogue) and all assimilations were performed on a 16-core (3.20GHz) Linux workstation with 64GB of RAM.

Since the experimental membrane voltage data is sampled discretely, the equations of motion imposed as equality constraints needed to be transformed from continuous time to discrete time. This linearization can be formulated as the following transformation $\frac{d\mathbf{x}(t)}{dt} = \mathbf{F}(\mathbf{x}(t)) \rightarrow \mathbf{x}(t_{n+1}) = \mathbf{x}(t_n) + \mathbf{g}(\mathbf{x}(t_n))$, where the choice of discretization method informs the mathematical formula denoted by $\mathbf{g}(x)$. One possibility is to use Simpson's integration rule, which has been used extensively throughout the literature [20–22]:

$$x_l(t_{i+2}) = x_l(t_i) + \Delta t\left[\frac{1}{3}F_l(\mathbf{x}(t_i)) + \frac{4}{3}F_l(\mathbf{x}(t_{i+1})) + \frac{1}{3}F_l(\mathbf{x}(t_{i+2}))\right], \tag{2.16}$$

and another is to use the higher-order Boole's integration rule [130]:

$$\begin{aligned} x_l(t_{i+4}) = x_l(t_i) + 2\Delta t\Bigg[&\frac{7}{45}F_l(\mathbf{x}(t_i)) + \frac{32}{45}F_l(\mathbf{x}(t_{i+1})) + \frac{12}{45}F_l(\mathbf{x}(t_{i+2})) \\ &+ \frac{32}{45}F_l(\mathbf{x}(t_{i+3})) + \frac{7}{45}F_l(\mathbf{x}(t_{i+4}))\Bigg], \end{aligned} \tag{2.17}$$

which should be expected to result in a higher accuracy of parameter estimates. In order to test the errors associated with each of these two methods, we generated model data using the 3-dimensional Lorenz system parametrized in a non-chaotic regime [131] and configured with two parameters $\sigma = 5.00$, $\rho = 40.0$. We then used our IPOPT-based assimilation procedure to estimate the model parameters from time series observations of the x-variable of the system. The estimated parameter values are shown in Table 2.2 for increasing values of model step size (Δt). We compare the parameter estimates for estimations using Simpson's rule with those using Boole's rule, and find that the higher order method has a much greater accuracy, particularly at larger step sizes. In Chapter 3, we describe a novel assimilation technique which implements a variable sampling rate, filtering points during slow-changing sub-threshold dynamics of the neuron. Boole's rule

	Simpson's Rule $\mathcal{O}(h^4)$		Boole's Rule $\mathcal{O}(h^6)$	
Δt	σ	ρ	σ	ρ
0.005	5.000014	39.99992	5.000007	39.99996
0.01	5.000227	39.99865	5.000087	39.99952
0.02	5.003508	39.97946	5.001243	39.99378
0.04	5.050703	39.71837	5.015792	39.94637
0.05	5.116377	39.37814	5.032581	39.93155
0.06	5.225957	38.84805	5.053511	39.99929
0.07	5.39159	38.10238	5.068867	40.29379
0.08	5.629235	37.06659	5.053436	41.11519
0.09	5.985983	37.06659	4.943448	43.16304
0.1	6.615143	32.55311	4.574006	48.39547
-	-	-	-	-
0.16	10	22.30755	1.739742	100

Table 2.2: Comparison of accuracy of parameters extracted using the Simpson rule and Boole rule. True parameter values: $\sigma = 5.0$, $\rho = 40.0$.

allows us to increase the step size in these regions considerably (Table 2.2) while, in contrast, Simpson's rule quickly breaks down. The accuracy of Boole's rule was found to be ideal for the 50 kHz sampling rate ($\Delta t = T/N = 0.02$ ms) primarily used throughout the work in this thesis. Furthermore, while we also tried alternative integration methods such as high-order Runge-Kutta schemes [130], we found that they significantly increased the computation time required to solve the optimization problem. Boole's rule is therefore well-suited for the optimization of neuron models.

When performing parameter estimation, we found that imposing the model equations of motion alone as equality constraints on the optimization was insufficient for obtaining a good estimate for unobserved state variables. As a demonstration, in Fig. 2.5, we once again present the results of a twin experiment on the Lorenz system in which we attempt to infer the full model state $\mathbf{x}(t) = [x(t), y(t), z(t)]$ from observations of the x-variable [131]. For these experiments the system was parametrized in the chaotic regime using the canonical parameter set $(\sigma, \beta, \rho) = (10, 8/3, 28)$. While the observed state variable, $x(t)$, is well-estimated across the assimilation window, the estimates for the unobserved variables display high-frequency oscillations close to the true solution. This ef-

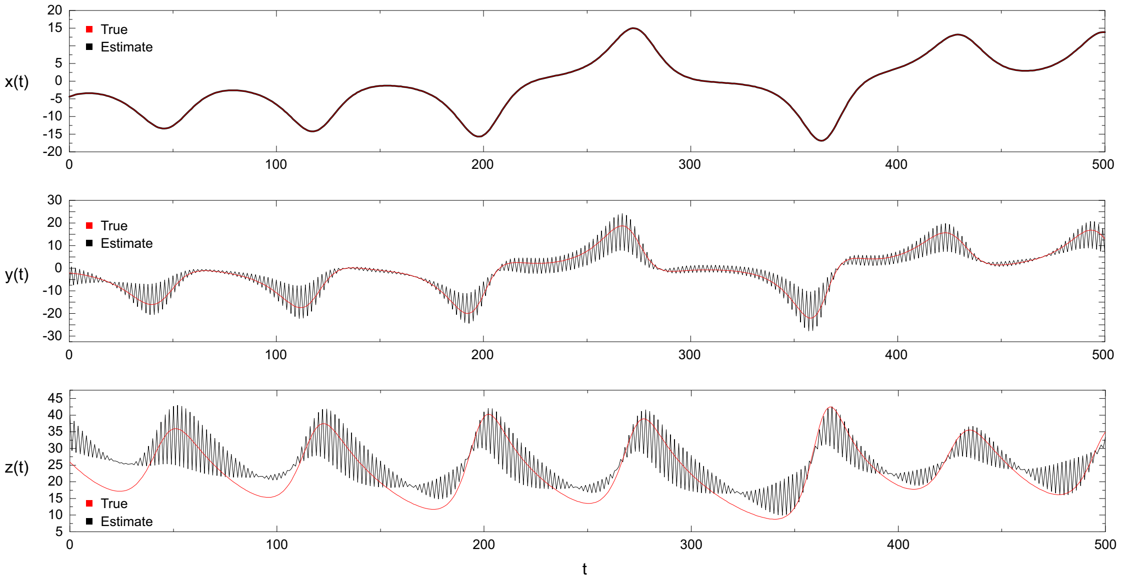

Figure 2.5: Twin experiment for the three-dimensional Lorenz system [131]. Using the data assimilation approach described in this section, we attempt to infer the evolution of the two unobserved state variables $y(t)$ and $z(t)$ from time series observations of the x-variable. In the absence of additional constraints enforcing smoothness on the state variables, we observe sub-optimal solutions (black) which oscillate close to the true solution (red).

fect has been observed previously in an optimization-based estimation framework [132]. In order to ensure smoothness of the estimated solutions, we used Hermite polynomial interpolation for all state variables as well as for the coupling variable $u(t)$ to constrain data mid-points:

$$x_l(t_{i+1}) = \frac{1}{2}[x_l(t_i) + x_l(t_{i+2})] + \frac{\Delta t}{8}[F_l(t_i) - F_l(t_{i+2})], \tag{2.18}$$

By imposing these additional interpolation constraints, we ensured that non-smooth solutions were considered invalid estimates of the model state. This is important, since the hidden states of conductance-based neuron models are known to exhibit smooth dynamics.

Part I

Predicting the Dynamics of Single Neurons

Chapter 3

Parameter estimation from imperfect observations

3.1 Introduction

Data assimilation has been used to successfully obtain predictive neuron models from membrane voltage data [81, 133, 134], but parameter estimation methods for these models have been reported to accept multi-valued parameter solutions [135, 136]. Identifying a single optimal parameter set is vital for constructing models that will perform well in response to novel stimuli. Furthermore, under ordinary conditions, neurons and biocircuits may exhibit functional overlap [137, 138] and redundancies [139, 140], complicating efforts to estimate actual neuron parameters. Systematic methods for estimating the true parameters of such systems is necessary for a number of tasks, including classifying neuronal phenotypes of unidentified cells [134, 141–143], and understanding the effects of disease on neuron dynamics at the molecular level [144–147]. In later chapters, we extend the methods presented here to the construction of predictive solid-state neuron models (Chapter 4) and inhibitory networks (Chapter 6) whose uses include the robust emulation of biological circuits [80] and providing a novel mechanism for improving cardiac function in a biomedical context [33, 53]. Neuron-based conductance models consist of coupled nonlinear differential equations which describe the evolution of state variables including membrane voltage and ion channel gates. The

Takens-Mañé embedding theorem states that information about the full state of a dynamic system may be preserved within the time series recording of a single state variable [148, 149]. This theory underpins the parameter estimation approaches which seek to constrain neuron models using membrane voltage data alone. However, the existence of a unique parameter solution is dependent on a number of conditions. Firstly, the modelled system must be *observable*, meaning its *initial conditions* can be estimated from observations of its state dynamics over a finite time window [150–152]. Secondly, the system must possess *identifiability*: any two distinct parameter sets $\mathbf{p}_1 \neq \mathbf{p}_2$ must produce different state trajectories under the same driving force and initial conditions. The criteria required for identifiability have not been extensively studied so far, partly because most investigations have focused on autonomous dynamical systems, rather than driven systems like stimulated neurons [137, 153]. Finally, variational cost functions are often riddled with local minima [154]. The arrival of gradient descent approaches at these local minima gives false parameter solutions. Obtaining false solutions becomes even more likely when the data are noisy, as the gap between the misfit to data of an optimal model and that of a sub-optimal model becomes narrower. In this situation, simply minimizing the cost-function will often fail to resolve true solutions from spurious ones. Regularization methods that allow the optimal solution to be recovered are therefore needed.

In this chapter, random Monte-Carlo simulations are performed to sample the posterior distribution functions (PDF) of parameters of a conductance-based neuron model estimated from noisy data. It is shown analytically how the interplay of model nonlinearity, experimental error, and model error acts to shift the maximum likelihood expectation and standard deviation of parameter estimates. The presence of noise is found to shift the location of the local and global minima relative to one another on the data misfit surface. This observation is subsequently harnessed to develop a novel approach to cost function regularization, increasing the probability of convergence towards the true global minimum from 67% to 94% for the conductance model, essentially making the parameter solutions independent of initial parameter guesses.

The chapter is structured as follows. The first section describes mathematically the effects of experimental error and model error on the data misfit surface.

The parameter offset $\delta\mathbf{p}_{\sigma\zeta}$ is calculated as a function of both model error and of the magnitude (σ) and realization (ζ) of additive noise. The second section demonstrates these results experimentally by computing the PDFs of estimated parameters and confirming the presence of noise-induced shifts in parameter solutions. The third section describes the novel regularization method that makes constructive use of the parameter offset to enhance the probability of convergence to optimal parameter solutions. The fourth section describes how parameter identifiability can be enhanced through the choice of external stimulation of the model and an increased assimilation window duration. Finally, the last section discusses predictions made by models configured with optimal and sub-optimal parameters. These results confirm that under appropriate conditions of stimulation, the predictions produced by distinct sets of parameters can always be distinguished.

3.2 Methods

3.2.1 RVLM neuron conductance model

In this chapter, we investigate a conductance-based model of a mammalian neuron from the rostral ventrolateral medulla (RVLM). RVLM neurons play a key role in cardiovascular function, which includes the control of blood pressure and respiration. These neurons possess a much greater complement of ionic currents than the Hodgkin-Huxley neuron [155, 156], and include transient sodium (NaT), delayed-rectifier potassium (K), low-threshold calcium (CaT) and a hyperpolarization-activated cation current (HCN) [105, 156]. These currents operate across a wide range of time courses and activate at significantly different thresholds, making these neurons ideal when testing the accuracy of the data assimilation method. The neuron model obeys the following equation of motion:

$$C\frac{dV(t)}{dt} = -J_{NaT} - J_K - J_{CaT} - J_{HCN} - J_L + I_{\text{inj}}(t)/A, \tag{3.1}$$

where C is the membrane capacitance (1.0 μF/cm^2), $V(t)$ is the membrane potential, $I_{inj}(t)$ is the external applied current, A is a parameter relating to the surface area of the neuron, and J_{ion} are the ion current densities (μA/cm^2) across the cell membrane. The equations of motion governing individual ion currents are summarized in Table 3.1. The amplitudes of these currents are determined by their respective maximal conductances (g_{NaT}, g_K, g_{HCN}, g_L), reversal potentials (E_{Na}, E_{K}, E_{HCN}, E_{L}), and gating variables (m, h, n, p, q, z). Ionic gating variables evolve according to the Hodgkin-Huxley framework:

$$\frac{dx}{dt} = \frac{x_\infty(V(t)) - x(t)}{\tau_x(V(t))}, \tag{3.2}$$

where $x \in \{m, h, n, z\}$ represents the state of (in)activation of the NaT, K and HCN ionic gates (Table 3.1). The (in)activation steady-state functions of the voltage-dependent gates are modelled by:

$$x_\infty(V) = \frac{1}{2}\left(1 + \tanh\frac{V - V_{tx}}{\delta V_x}\right), \tag{3.3}$$

where V_{tx} is the threshold voltage of the gate, and δV_x defines the slope of the sigmoid curve. The (in)activation time constant functions are modelled as:

$$\tau_x(V) = t_x + \epsilon_x\left(1 - \tanh^2\frac{V - V_{tx}}{\delta V_{\tau x}}\right), \tag{3.4}$$

where $\delta V_{\tau x}$ is the half-width-at-half-maximum of the bell-curve, and t_x, ϵ_x determine the height of curve peak. The transient low-threshold Ca^{2+} current is described by the Goldman-Hodgkin-Katz (GHK) equation:

$$J_{CaT} = \overline{p} \cdot p^2 \cdot q \cdot z^2 \cdot \frac{VF^2}{RT} \cdot \frac{[Ca^{2+}]_i - [Ca^{2+}]_o \cdot \exp\frac{-zFV}{RT}}{1 - \exp(\frac{-zFV}{RT})}, \tag{3.5}$$

where the gating variables p and q describe the activation and inactivation of the CaT channel, respectively. $\overline{p}_{\mathrm{T}}$ is the maximal permeability of the channel, $[\mathrm{Ca}^{2+}]_i$ and $[\mathrm{Ca}^{2+}]_o$ are the intracellular and extracellular calcium concentrations, $z = 2$ is the valence of Ca^{2+}, F is the Faraday constant, R is the gas constant, and $T = 298.15\mathrm{K}$. The GHK equation displays singular behaviour at $V = 0$ mV. To avoid this singularity, the Wolfram Mathematica software package was used to expand the GHK equation, giving a Horner form polynomial of order $n = 25$

which approximates Eq. 3.5 over the typical dynamic range of membrane voltages [157]. As described in Chapter 2, a nudging control term $u(t_n)[V_{\exp}(t_n) - V(t_n)]$ was added to Eq 3.1 to drive synchronization of the model to the observed data by smoothing irregularities in the search landscape [158].

3.2.2 Generating synthetic data

An array of complex current protocols $I_{inj}(t)$ were generated to provide stimulation to the model. These consisted of rapidly changing positive and negative current steps of varying duration and amplitude (Fig. 3.1, blue trace). The protocols were calibrated to elicit depolarization, spiking, and hyperpolarization across a range of time scales that encompassed the recovery times of the ion channels. This is a necessary requirement of the assimilation procedure; in order that the membrane voltage observations contain sufficient information for a successful parameter estimation, the neuron must be driven to operate across a wide dynamic range [159]. Data were synthesized by forward-integrating the neuron model (Eqs. 3.1-3.5) in response to the current protocols. The model was paramatrized according to the set of parameters denoted $\mathbf{p}_{\text{true}}$ in Table 3.2. The model equations were integrated using the LSODA solver in the from the Python SciPy library [160] which is ideal for stiff nonlinear systems [161]. Measurement errors were added to the model membrane voltage time series by the addition of Gaussian noise with zero-mean. This process obtained pairs of current and membrane voltage time series, $I_{inj}(t_i)$ and $V_{\exp}(t_i)$, to be used in the parameter estimation. The sampling rate of the time series was 100 kHz ($\Delta t = 10$ μs).

3.3 Results

3.3.1 Cost function expansion

The distance between the model membrane voltage state variable $V_{\text{mod}}(t_i, \mathbf{x}(0), \mathbf{p})$ and the experimentally-observed membrane voltage $V_{\exp}(t_i)$ is given by a least-squares cost function. The cost function is evaluated as the sum of distances at each time point $i = 0 \ldots n$ of the assimilation window of duration T and is given

ID	Channel	Current density	Maximal conductance
NaT	Fast and transient Na^+ current	$J_{\mathrm{NaT}} = g_{\mathrm{NaT}} m^3 h (E_{\mathrm{Na}} - V)$	$g_{\mathrm{NaT}} = 69$ mS.cm^{-2}
K	Transient depolarization-activated K^+ current	$J_{\mathrm{K}} = g_{\mathrm{K}} n^4 (E_{\mathrm{K}} - V)$	$g_{\mathrm{K}} = 6.9$ mS.cm^{-2}
HCN	Hyperpolarization-activated cation current	$J_{\mathrm{HCN}} = g_{\mathrm{HCN}} z (E_{\mathrm{HCN}} - V)$	$g_{\mathrm{HCN}} = 0.15$ mS.cm^{-2}
CaT	Low-threshold Ca^{2+} current	$J_{\mathrm{CaT}} = GHK$	-
L	Passive leakage current	$J_{\mathrm{L}} = g_{\mathrm{L}} (E_{\mathrm{L}} - V)$	$g_{\mathrm{L}} = 0.465$ mS.cm^{-2}

Table 3.1: Ion channels present in the RVLM neuron model. Equations describing the current densities are given along with their respective maximal conductances g_α, $\alpha \in \{\mathrm{NaT}, \mathrm{K}, \mathrm{HCN}, \mathrm{L}\}$; reversal potentials for sodium and potassium are given by $E_{\mathrm{Na}} = +41$ mV and $E_{\mathrm{K}} = -100$ mV, respectively; hyperpolarized-activated cation reversal potential $E_{\mathrm{HCN}} = -43$ mV; leakage potential $E_{\mathrm{L}} = -65$ mV. The gating variables m and h govern activation and inactivation of the NaT channel, respectively. Activation of the potassium channel is governed by the gating variable n, and z is the HCN activation gate. The calcium current is given by the Goldman-Hodgkin-Katz equation (Eq. 3.5) and has no maximal conductance.

by

$$c(\mathbf{x}(0), \mathbf{p}) = \frac{1}{2} \sum_{i=0}^{n} \{ (V_{\text{exp}}(t_i) - V_{\text{mod}}(t_i, \mathbf{x}(0), \mathbf{p}))^2 + u^2(t_i) \}, \tag{3.6}$$

where the variables $x_l(t)$, $l = 1 \ldots L$ define the state of the condutance-based model and the K model parameters are denoted p_k, $k = 1 \ldots K$. The state variables of the model are evaluated at discrete times $t_i = iT/n$, $i = 0 \ldots n$ across the assimilation window. They comprise the membrane voltage and gating variables of the neuron. The function $u(t)$ is the coupling term (Sec. 2.3.3) which regularizes the search space, smoothing convergence by eliminating positive values of the conditional Lyapunov exponents [162, 163]. As with the model variables, $u(t)$ is also evaluated at each discrete time point.

The different contributions of the experimental error and model error to the shift in parameter solutions can be considered by introducing the concept of the useful membrane voltage, denoted $V_{\text{use}}(t_i)$. This is the voltage that would be measured by the ideal current clamp (Fig. 3.1(a)) in the presence of zero noise, allowing us to separate experimental error, defined as $\epsilon_{\text{exp}}(t_i) = V_{\text{exp}}(t_i) - V_{use}(t_i)$, from model error, $\epsilon_{mod}(t, \mathbf{x}(0), \mathbf{p}) = V_{mod}(t, \mathbf{x}(0), \mathbf{p}) - V_{use}(t)$. Experimental error, $\epsilon_{\text{exp}}(t_i)$, corresponds to the contributions of measurement noise, thermal fluctuations etc. Assuming that these contributions can be considered random errors, they can be modelled as $n+1$ random variables $\epsilon_{\sigma\zeta}(t_i)$, $i = 0 \ldots n$, each sampled from a normal distribution, $\mathcal{N}(0, \sigma)$, with zero mean and standard deviation σ. Generating a set of $n+1$ variables this way gives an error for each point in the assimilation window, and each distinct set is called a noise 'realization'. Individual realizations are labelled ζ. The second form of error contributing to the shift in parameter solutions is model error. Model error, unlike experimental error, is a function of the model equations, model parameters and the initial state of the system. Having defined the two sources of error, $\epsilon_{\text{exp}}(t_i)$ and $\epsilon_{mod}(t, \mathbf{x}(0), \mathbf{p})$, the cost function may be expanded as:

$$\begin{aligned} c(\mathbf{x}(0),\mathbf{p}) &= \frac{1}{2}\sum_{i=0}^{n}\{\epsilon_{mod}^2(t_i,\mathbf{x}(0),\mathbf{p}) + u^2(t_i)\} \\ &+\frac{1}{2}\sum_{i=0}^{n}\epsilon_{\sigma\zeta}^2(t_i) + \sum_{i=0}^{n}\epsilon_{\sigma\zeta}(t_i)\epsilon_{mod}(t_i,\mathbf{x}(0),\mathbf{p}), \end{aligned} \tag{3.7}$$

making explicit the separate contributions from model errors and experimental errors.

Using this expanded cost function, one can now consider precisely how the cost function is modified in the presence of errors. Since parameter estimates correspond to the arrival of gradient descent algorithms at local / global minima, it is sufficient to consider the effect of errors in their vicinity. The global minimum at zero noise, corresponding to the true parameter set, is labelled $\mathbf{p}_0^*$. The perturbation of the cost function by noise of standard deviation σ is given by $\delta c = c(\mathbf{x}(0),\mathbf{p}_{\sigma\zeta}) - c(\mathbf{x}(0),\mathbf{p}_0^*)$. This quantity is the data misfit. Expanding about the true global minimum $\mathbf{p}_0^*$ gives:

$$\delta c = F + (\mathbf{p}-\mathbf{p}_0^*)^T\mathbf{G} + \frac{1}{2}(\mathbf{p}-\mathbf{p}_0^*)^T\hat{\mathbf{H}}(\mathbf{p}-\mathbf{p}_0^*)\ldots \tag{3.8}$$

The first three terms in the expansion correspond to: the offset F representing signal noise entropy (Eq. 3.11); a finite gradient $\mathbf{G}$ that arises from a combination of model nonlinearity and the noise realization (Eq. 3.9); and the Hessian $\hat{\mathbf{H}}$ perturbed by experimental and model errors (Eq. 3.10).

$$G_k = \sum_{i=0}^{n}\epsilon_{\sigma\zeta}(t_i)\left.\frac{\partial V_{mod}}{\partial p_k}\right|_{\mathbf{p}_0^*}, \tag{3.9}$$

$$H_{kk'} = \sum_{i=0}^{n}\left\{\left.\frac{\partial V_{mod}}{\partial p_k}\right|.\left.\frac{\partial V_{mod}}{\partial p_{k'}}\right|_{\mathbf{p}_0^*} + \left.\frac{\partial^2 V_{mod}}{\partial p_k \partial p_{k'}}\right|_{\mathbf{p}_0^*}[\epsilon_{\sigma\zeta}(t_i)+\epsilon_{mod}(t_i,\mathbf{x}(0),\mathbf{p})]\right\}, \tag{3.10}$$

$$F = \frac{1}{2}\sum_{i=0}^{n}\epsilon_{\sigma\zeta}^2(t_i) + \sum_{i=0}^{n}\epsilon_{\sigma\zeta}(t_i)\epsilon_{mod}(t_i,\mathbf{x}(0),\mathbf{p}). \tag{3.11}$$

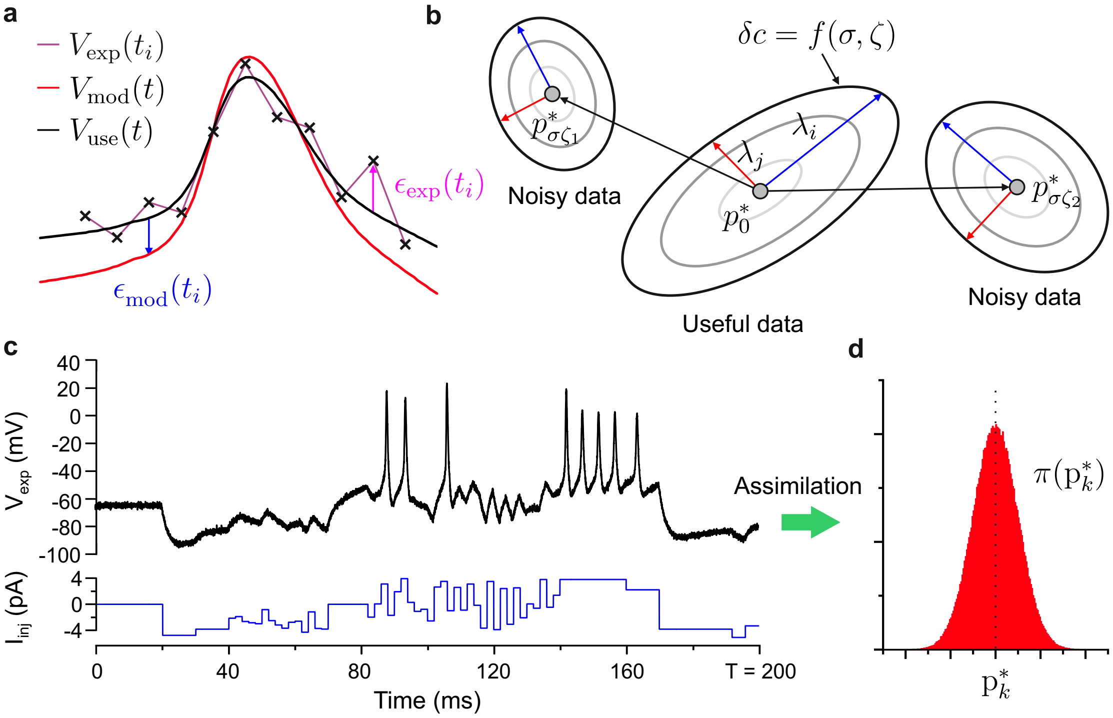

Figure 3.1: The data misfit surface is perturbed by experimental and model error. (a) Membrane voltage, $V_{\mathrm{exp}}(t_i)$, is recorded in discrete time t_i, $i = 0, ..., n$ (cross symbols); we denote the useful membrane voltage obtained from an ideal measurement apparatus by $V_{\mathrm{use}}(t)$ (black line); membrane voltage state variable of the conductance model, $V_{\mathrm{mod}}(t)$ (red line). Experimental error is given by $\epsilon_{\mathrm{exp}}(t_i) = V_{\mathrm{exp}} - V_{\mathrm{use}}(t_i)$. Model error is given by: $\epsilon_{\mathrm{mod}} = V_{\mathrm{mod}} - V_{\mathrm{use}}(t)$. (b) Lines of constant data misfit, $\delta c = f(\sigma, \zeta)$, in the vicinity of the global minimum p^*_0. Different noise realizations, $\zeta_1(\zeta_2)$, shift the global minimum in different ways $\mathbf{p}^*_0 \rightarrow \mathbf{p}^*_{\sigma\zeta_1}$ ($\mathbf{p}^*_0 \rightarrow \mathbf{p}^*_{\sigma\zeta_2}$). Noise also tilts the principal axes of the data misfit ellipsoid (red / blue arrows) and modifies the principal semi-axes (λ_i, λ_j). (c) RVLM neuron model membrane voltage V_{exp} (black line) driven by current injection I_{inj} (blue line). Additive noise $\epsilon_{\sigma\zeta}$ is incorporated in the model data prior to assimilation. (d) Posterior distribution function $\pi(p_k)$ of parameter p_k, $k = 1, ..., K$.

Let us now consider what each of these three terms means for parameter solutions at the global minimum. The surface of constant data misfit, $\delta c = f(\sigma, \zeta)$ (Fig. 3.1(b)), is a K-dimensional ellipsoid. The finite gradient term $\mathbf{G}$ (Eq. 3.10) acts to shift the centre of this ellipsoid from the true value, $\mathbf{p}_0^*$, to a new location denoted $\mathbf{p}_{\sigma\zeta}^*$. This shift moves the global minimum to a new location in parameter space. Practically speaking, this means that any variational assimilation approach landing at the global minimum will no longer correspond to the true parameter set. Note that this shift depends on the noise realization, ζ (Fig. 3.1(b)). Generally speaking, the vector components of $\mathbf{G}$ will remain finite (Eq. 3.10). This can be understood by considering the quantity $\partial V_{mod}/\partial p_k$. The precise timings of the rapid swings in membrane voltage that occur at the site of action potentials (-100 mV to +45 mV) are highly sensitive to tiny changes in parameter values. Thus, very small changes in the timing of an action potential result in a very large change in the value of V_{mod} for data points in the vicinity of that spike. Hence, the noise-weighted derivatives $\partial V_{mod}/\partial p_k$ averaged across the assimilation window typically give non-zero gradient values $G_k(\zeta)$ which are noise realization-dependent. Therefore, distinct noise realizations, ζ, will give different parameter offsets, $\delta \mathbf{p}_{\sigma\zeta} = \mathbf{p}_{\sigma\zeta}^* - \mathbf{p}_0^*$ (Fig. 3.1(b)).

Consider next the Hessian expansion term, $\hat{\mathbf{H}}$, arising as a result of the superposition of noise and model error. The first term in $H_{k,k'}$ determines the curvature of the data misfit surface (Eq. 3.9). This term defines the 'sloppiness' of model parameters [136]. Parameter sloppiness is a term describing the fact that models may be more sensitive to changes in certain combinations of parameters than others. Small curvature in data misfit space corresponds to 'sloppy' parameters that are less tightly constrained [164]. The second term in (Eq. 3.9) defines the perturbation of this curvature by noise and model error. Just as for $\mathbf{G}$, the second derivative of V_{mod} with respect to p_k and $p_{k'}$ typically does not exactly cancel in the summation across the assimilation window. As a result, the finite term that remains is expected to tilt the principal axes of the data misfit ellipsoid and change their semi-axes. Practically speaking, this corresponds to an alteration in parameter correlations.

The final term in the expansion is F which represents the signal noise entropy plus the sum of the products of noise and model error values. The first term in F

dominates, and corresponds to the random energy $T_{\sigma\zeta} dS$ relating to noise entropy dS through the Johnson-Nyquist theorem [165, 166]:

$$\frac{1}{2}\sum_{i=0}^{n} \epsilon^2_{\sigma\zeta}(t_i) = 2(n+1)k_B T_\sigma R \Delta f, \tag{3.12}$$

where k_B is the Boltzmann constant, T_σ is the noise-equivalent temperature, R is the membrane resistance of the neuron, and Δf is the bandwidth of noise.

Having considered the effects of model and experimental error on the cost function, one can now proceed with the calculation of the noise-induced parameter offset. The shift $\delta\mathbf{p}_{\sigma\zeta}$ is obtained through principal analysis of the Hessian matrix term $\hat{\mathbf{H}}'$. In the basis of its eigenvectors, the Hessian $\hat{\mathbf{H}}' = \hat{\mathbf{V}}^T \hat{\mathbf{H}} \hat{\mathbf{V}}$ is a $K \times K$ diagonal matrix:

$$\hat{H}' = \begin{bmatrix} \lambda_1^{-2} & 0 & \dots & 0 \\ 0 & \lambda_2^{-2} & \dots & 0 \\ \vdots & \vdots & \ddots & \vdots \\ 0 & 0 & \dots & \lambda_K^{-2} \end{bmatrix} \tag{3.13}$$

where the λ_k are the principal semi-axes of the data misfit ellipsoid. $\hat{\mathbf{V}}$ is the $K \times K$ orthonormal matrix of eigenvectors transforming $\delta\mathbf{p}$ into $\delta\mathbf{p}' = \hat{\mathbf{V}}^T \delta\mathbf{p}$ in the new basis and $\mathbf{G}$ into $\hat{\mathbf{G}}' = \hat{\mathbf{V}}^T \hat{\mathbf{G}}$. The data misfit $\delta c = f(\sigma, \zeta)$ may be written as:

$$\delta c = F' + \sum_{k=1}^{K} \left(\delta p'_k + \frac{G'_k}{\lambda_k}\right) \frac{1}{2\lambda_k} \left(\delta p'_k + \frac{G'_k}{\lambda_k}\right), \tag{3.14}$$

where

$$F' = F - \sum_{k=1}^{K} \frac{(G'_k)^2}{2\lambda_k}. \tag{3.15}$$

The noise-induced offset follows from Eq. 3.14 as $\delta\mathbf{p} = \mathbf{V}^T \hat{\mathbf{H}}^{-1} \mathbf{G}$. Through the gradient term $\mathbf{G}$, experimental error gives the first-order contribution to the shift in parameter solutions (Eq. 3.14). A second-order contribution is given by model error through its perturbation of $\hat{\mathbf{H}}$. The principal axes of the ellipsoid are tilted according to the eigenvectors of the matrix $\mathbf{V}$, and their semi-axes are the eigenvalues λ_k of $\mathbf{V}$.

3.3.2 Twin experiments: posterior distribution of parameters

In this section, we demonstrate the above results experimentally with the RVLM neuron model by computing the posterior distribution function (PDF) of the estimated parameters in the presence of noise. This is done by performing a statistical ensemble of assimilations, each member of which has a different noise realization, and tabulating the parameters estimated in each. The following section will then analyse the effect of *individual* noise realizations on parameter solutions by calculating individual parameter offsets relative to the zero-noise situation.

The RVLM model has 7 state variables ($L = 7$) and 41 parameters ($K = 41$). The biological parameters are the vector components of $\mathbf{p}_{true}$ presented in Table 3.2. Model membrane voltage data, $V_{mem}(t)$, were synthesized by configuring the RVLM model with $\mathbf{p}_{true}$ and forward integrating the model response to the current protocol shown in Fig. 3.1(c) (blue line). In order to validate that the nonlinear optimization method could infer the true parameter solution, a "twin-experiment" was conducted which attempted to recover the model parameters by performing data assimilation on the model data with no noise. The parameters were estimated using the interior point line parameter search algorithm [167] described in Sec. 2.3.3. The assimilation window had $n = 10,000$ mesh points with mesh size $\Delta t = 20\ \mu$s ($T = 200$ ms). The 41 parameters of the optimal solution $\mathbf{p}_0^*$ are listed in Table. 3.2. All parameter estimates were found to be within 4% of their true value.

Before computing the PDFs of the model parameters, noisy, 'experimental' data were synthesized by adding noise to the useful membrane voltage: $V_{\exp}(t) = V_{mem}(t) + \epsilon_{\sigma\zeta}(t)$. A set of $R = 1,000$ different time series were generated (each with a different noise realization, ζ) to generate a statistical distribution of estimated parameters $\pi(\mathbf{p}^*_{\sigma\zeta})$. Since the quantity of interest is the parameter solution at the global minimum, the parameter search was initialized at $\mathbf{p}_0^*$ in order to reduce the computational time associated with gradient descent over a large cost-function

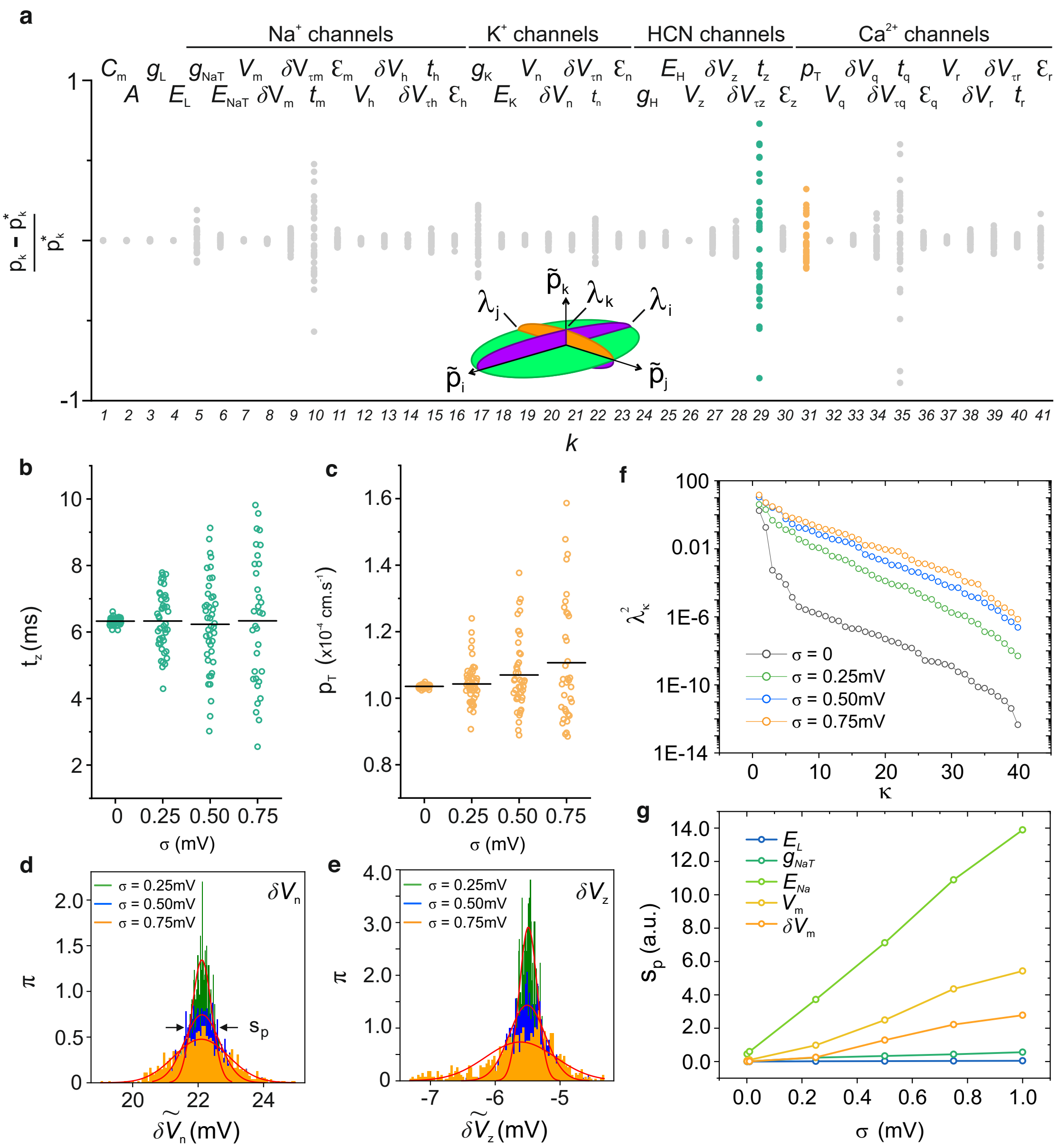

Figure 3.2: Probability distributions of estimated model parameters. (a) Scatter plot of parameters p_k, $k = 1, ..., 41$, estimated by assimilating RVLM membrane voltage traces incorporating different realizations of Gaussian noise. Noise amplitude: $\sigma = 0.75$ mV. The dependence of the distribution on noise amplitude is plotted for two parameters: (b) the recovery time t_z of HCN inactivation gate and, (c) the maximum permeability $\overline{p}_T$ of the CaT ion channel. (d,e) Probability density functions (PDF) of parameters t_z and $\overline{p}_T$ calculated at increasing noise amplitudes $\sigma = 0.25$, 0.50 and 0.75 mV. Statistical sample: 1000 parameter sets extracted for different noise realizations. The initial guess for the estimations was $\mathbf{p}_0^*$ (f) Eigenvalue spectrum of the 41×41 covariance matrix of parameter estimates. The λ_κ, $\kappa = 1, ..., 41$ are the semi-axes of the data misfit ellipsoid $\delta c = f(\sigma, \zeta)$ and the λ_K^2 are the eigenvalues of covariance matrix Σ. Eigenvalue spectra are calculated at increasing noise amplitudes: $\sigma = 0$, 0.25, 0.50 and 0.75 mV. (g) The relationship between the standard deviation of estimates for a parameter, s_p, and the noise amplitude at which the estimates were performed, σ.

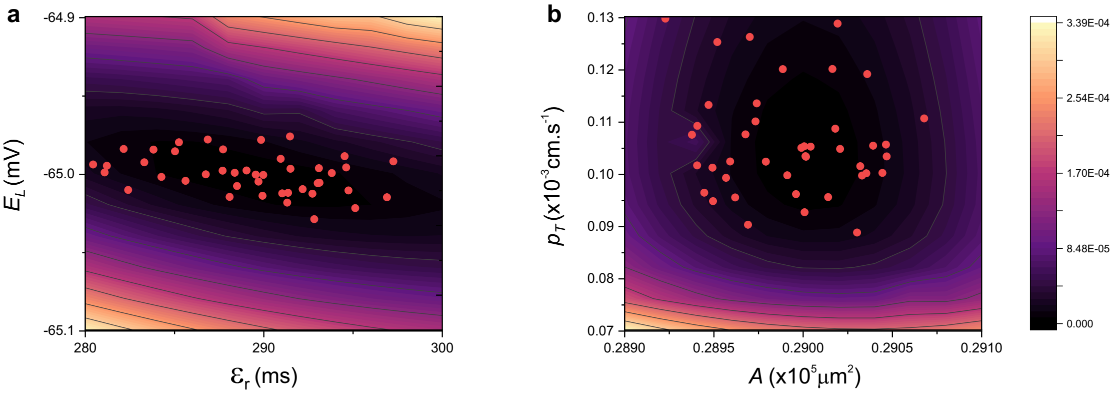

Figure 3.3: Dependence of the cost function on parameter pairs. (a) Dispersion of extracted parameters (E_L, ϵ_r) superimposed on a contour map of the noiseless cost function in the $E_L - \epsilon_r$ plane. The topography of the cost function was mapped by optimizing for different combinations of fixed E_L and ϵ_r. The colour bar gives the terminal value of the cost function upon completion of the minimization. (b) Same as (a) for the parameter pair (p_T, A).

space. Fig. 3.2(a) plots the distribution of estimated parameters centred on their mean value for a noise intensity of $\sigma = 0.75$ mV. The sloppiest parameters are the recovery time constants, specifically those of the Na^+ channel (t_m), HCN channel (t_z), and low threshold Ca^{2+} channel (t_q). This is consistent with previously described results in the literature [22, 81]. Increasing the noise amplitude from $\sigma = 0$ to 0.75 mV was found to broaden the distribution of estimated parameters. This is presented in Figs. 3.2(b,c) for the HCN recovery time parameter (t_z) and the maximum Ca^{2+} permeability (p_T). For the parameter t_z, as the noise amplitude increases from $\sigma = 0$ to 0.75 mV the maximum likelihood estimate (horizontal black line) remains approximately constant and the standard deviation of the distribution broadens symmetrically (Fig. 3.2(b)). In contrast, the MLE of the permeability parameter p_T increases as noise amplitude increases. This is due to the fact that for p_{T}, the parameter distribution is asymmetrical even at low noise levels.

The 1,000 parameter estimations were then used to compute the PDFs of the model parameters, revealing the effects of model nonlinearity on the cost function perturbations. The PDFs of the parameters controlling the slopes of the activation curves of K^+ (δV_n) and HCN (δV_z) are plotted in Figs. 3.2(d) and (e), respectively.

The Gaussian best fits (solid red line) are overlaid on top of the PDFs at three noise levels, $\sigma = 0.25, 0.5, 0.75$ mV. For parameter δV_n, just as was observed for t_z, the MLE of parameter is noise-independent. The PDF of this parameter remains approximately Gaussian even at large noise levels, and the standard deviation of the PDF increases with noise amplitude (Fig.3.2(d)). On the other hand, for parameter δV_z, as with p_T, the PDF is non-Gaussian and broadens asymmetrically as σ increases (Fig.3.2(e)).

Lastly, the correlations between estimated parameters and the effect of increasing noise amplitude on these correlations were investigated. This required computing the following covariance matrix:

$$\hat{\Sigma}_{l,m} = \frac{1}{R-1} \sum_{r=1}^{R} \left(p_{l,r} - \bar{p}_l\right) \left(p_{m,r} - \bar{p}_m\right), \tag{3.16}$$

which is related to the Hessian (Eq. 3.13) through $\hat{\mathbf{H}} = \hat{\mathbf{\Sigma}}^{-1}$. We computed the eigenvalues λ_k^2 of $\mathbf{\Sigma}$ which correspond to the squares of the principal half-lengths of the data misfit ellipsoid (Fig. 3.2(f)). It was observed that the parameters of the RVLM model exhibit correlations spanning several orders of magnitude. Although most parameters are well-constrained, not all correlations vanish as the noise intensity diminishes ($\sigma \to 0$). The two leftmost points (black circles) indicate pairs of parameters which remain highly correlated irrespective of noise level. By inspecting the eigenvectors of the covariance matrix, one finds that these parameters are the recovery time constants t_m, t_z and t_q previously noted in Fig. 3.2(a) to have a wider parameter spread. As expected, increasing noise intensity led to increased parameter correlation. The dependence of the standard deviation of the PDF, s_p, as a function of the noise intensity σ was also calculated. Fig. 3.2(g) presents some of these calculated values for arbitrarily-chosen parameters.

3.3.3 Twin experiments: cost function topography

To conclude this section, it is worth considering how the posterior distributions of the model parameters relate to the shape of the cost function in the vicinity of local and global minima. To illustrate this relationship, parameter estimations were performed on the noiseless model data in which pairs of parameters were fixed to certain values during the assimilation. In the first example, the parameters E_L and ϵ_r took values on a grid within ranges -65.1 mV $< E_L < -64.9$ mV and 280 ms $< \epsilon_r <$ 300 ms. For each value of (E_L, ϵ_r) on the grid, the cost function was minimized, and the value (height) of the cost function was recorded. This allows us to map the 'true' zero-noise cost function landscape. Fig. 3.3(a) shows the dependence of the cost function value on (E_L, ϵ_r) in terms of contour lines. One can see that in the middle there exists a long, thin expanded area near the true global minimum solution (290, -65.0) where the cost function is almost zero. The noise-perturbed parameter estimates for the pair (E_L, ϵ_r) that were presented in Fig. 3.2 are superimposed on the cost function contour map. The perturbations occur along directions of minimum curvature, as predicted in Sec. 3.3.1. Fig. 3.3(b) shows the dependence of the cost function magnitude on a second parameter pair (p_T, A). The cost function in this plane increases almost uniformly in all directions, and the noise-perturbed parameter estimates that are superimposed reflect this. These results give further evidence that noise-induced shifts in parameter solutions can be used to sample from the posterior distribution of the parameter set, or, equivalently, to map the topography of the cost function in the vicinity of local and global minima.

3.3.4 Additive noise regularizes the cost function

As discussed in Sec. 2.3.3, the cost function associated with nonlinear models is often highly irregular, hosting a plethora of local minima. This fact necessarily means that certain initial guesses of state variables and parameters may lead the gradient descent algorithm to arrive at sub-optimal solutions which are local minima of the data misfit function. We found empirically that the addition of Gaussian noise to the membrane voltage data often acted to regularize the data misfit surface, removing spurious local minima. We now demonstrate this, by first identifying the local minimum nearest to the global minimum by running an ensemble of parameter searches initialized at random points in parameter space using the zero-noise time series. The parameter solution associated with this local minimum in the absence of additive noise is given in Table 3.2 as p_0^ℓ. Having

Ion	Parameter		Data		Estimates		
			$\boldsymbol{p}_L, \boldsymbol{p}_U$	$\boldsymbol{p}_{\text{true}}$	$\boldsymbol{p}_0^*$	$\boldsymbol{p}_\sigma^*$	$\boldsymbol{p}_0^\ell$
	C	μF.cm^{-2}	1.0, 1.0	1.0	1.0	1.0	1.0
	E_{Na}	mV	42, 50	41	41.007	41.075	60.000
	E_{K}	mV	-90, -80	-100	-100.005	-100.763	-90.000
	E_{H}	mV	-30, -5	-43	-42.963	-42.793	-30.000
	E_{Leak}	mV	-110, -65	-65	-64.999	-64.964	-66.541
	A	$\times 10^4 \mu m^2$	20^2 - 50^2	2.90	2.90	2.91	2.90
NaT	g_{NaT}	mS.cm^{-2}	100, 120	69	68.912	69.924	100.000
m	V_m	mV	-49, -27	-39.92	-39.921	-39.965	-30.931
	dV_m	mV	5, 32	10	10.000	9.949	15.850
	dV_{tm}	mV	5, 23.39	23.39	23.380	23.254	0.100
	t_{0m}	ms	0.02, 0.7	0.143	0.143	0.157	0.815
	ϵ_m	ms	0.012, 7	1.099	1.099	1.094	19.543
h	V_h	mV	-79, -39	-65.37	-65.365	-65.558	-52.863
	dV_h	mV	-35, -5	-17.65	-17.652	-17.629	-13.752
	dV_{th}	mV	4, 43	27.22	27.218	27.670	14.107
	t_{0h}	ms	0.02, 90	0.701	0.701	0.684	0.502
	ϵ_h	ms	1, 470	12.9	12.898	12.942	10.629
$\mathbf{K_{DR}}$	$g_{K_{DR}}$	mS.cm^{-2}	0	6.9	6.905	6.736	2.232
m	V_m	mV	-69, -21	-34.58	-34.557	-34.763	-39.654
	dV_m	mV	5, 34	22.17	22.178	21.932	13.118
	dV_{tm}	mV	5, 34	23.58	23.588	23.851	21.556
	t_{0m}	ms	0.01, 5.4	1.291	1.291	1.273	0.434
	ϵ_m	ms	0.002, 23	4.314	4.311	4.248	6.416
CaT	p_{T}	$\times 10^{-4}$ cm.s^{-1}	0, 80	1.035	1.035	0.210	0.130
	V$_m$	mV	-80, -35	-65.5	-65.491	-64.483	-67.767
m	dV_m	mV	5, 39	12.4	12.391	14.003	9.958
	dV_{tm}	mV	10, 57	27	27.123	28.911	14.985
	t_{0m}	ms	0.02, 0.9	0.719	0.693	2.232	7.556
	ϵ_m	ms	0.5, 97	13.05	13.059	11.759	8.370
h	V_h	mV	-90, -55	-86	-86.011	-73.916	-74.356
	dV_h	mV	-34, -5	-8.06	-8.065	-4.547	-3.962
	dV_{th}	ms	3, 55	16.71	16.760	9.829	0.100
	t_{0h}	ms	5, 190	28.17	28.120	27.435	55.095
	ϵ_h	mV	0.5, 7000	288.68	287.067	319.355	1000.000
HCN	g_{H}	mS.cm^{-2}	0, 10	0.150	0.150	0.149	0.177
h	V_h	mV	-90, -40	-76	-76.001	-76.297	-79.121
	dV_h	mV	-30, -5	-5.5	-5.517	-5.430	-11.876
	dV_{th}	mV	5, 40	20.27	20.273	21.861	100.000
	t_{0h}	ms	0.1, 500	6.31	6.348	0.100	10.000
	ϵ_h	mV	0.1, 5000	55.05	55.019	60.471	50.323
Leak	g_L	mS.cm^{-2}	0.01, 0.6	0.465	0.465	0.463	0.482

Table 3.2: True and estimated parameters of the RVLM neuron model. From left column to right column: lower and upper bounds on the parameter search interval, $[\mathbf{p}_L, \mathbf{p}_U]$; true parameters used to generate the model data, $\mathbf{p}_{\text{true}}$; optimal parameters estimated at the true global minimum of the cost function, $\mathbf{p}_0^*$ ($\sigma = 0$); sub-optimal parameters estimated at the global minimum shifted by noise, $\mathbf{p}_{\sigma\zeta}^*$ ($\sigma = 0.5$ mV); sub-optimal parameters estimated at the local minimum, $\mathbf{p}_0^l$ ($\sigma = 0$), nearest to the global minimum $\mathbf{p}_0^*$.

identified a local minimum, the effect of noise amplitude σ and noise realization ζ on the relative positions of $p^*_{\sigma\zeta}$ and $p^\ell_{\sigma\zeta}$ can be studied.

The regularization method is depicted schematically in Fig. 3.4(a). The method relies on the principles behind the noise-induced shift in parameter solutions described in the previous sections. To begin, a single realization of additive noise (ζ) was chosen and the amplitude of that realization was scaled in the range -0.5 mV$< \sigma < +0.5$ mV. The method proceeds as follows: (i) starting from the zero-noise situation, $\sigma = 0$, the local and global minima, $\mathbf{p}^\ell_0$ (pink star) and $\mathbf{p}^*_0$ (red star), are separated by a saddle point (white dot) in the cost function surface; (ii) as the noise amplitude σ increases, the two minima undergo a shift relative to one another, moving closer together or further apart depending on the sign of σ. As the local and global minima $\mathbf{p}^*_{\sigma\zeta}$ and $\mathbf{p}^\ell_{\sigma\zeta}$ approach one another, there exists a critical noise amplitude σ_{crit} (iii) where the saddle point and the local minimum merge through a saddle-node bifurcation [106]. Note that a gradient descent method (blue dot), which may previously have arrived at the local minimum, would now continue towards the global minimum: $\mathbf{p}^\ell_{\sigma\zeta} \to \mathbf{p}^*_{\sigma\zeta}$; (iv) $\mathbf{p}^*_{\sigma\zeta}(\zeta)$ is then set as the new initial guess of the parameter search. The noise amplitude σ is then ramped down from σ_{crit} to zero, thus obtaining the optimal parameter solution $\mathbf{p}_0$.

Steps (i) to (iii) of the method are demonstrated numerically in Figs. 3.4(b,c). Two distinct noise realizations ζ_1 and ζ_2 were applied to the voltage data in Figs. 3.4(b) and Figs. 3.4(c), respectively. The assimilation window had $N = 10,000$ points and $\Delta t = 20\mu$s. The parameter search was initialized at the local minimum $\mathbf{p}^\ell_0$ where the cost function was $c(\mathbf{x}(0), \mathbf{p}^\ell_0) = 9.105306 \times 10^{-5}$. For reference, the cost function at the global minimum $\mathbf{p}^*_0$ was almost two orders of magnitude smaller at $C(\mathbf{x}(0), \mathbf{p}^*_0) = 1.179402 \times 10^{-6}$. For each noise realization, the estimation procedure was allowed to proceed from its initialization at $\mathbf{p}^\ell_0$. In both cases, the parameter solution of the estimation was projected in the two-dimensional plane $(\epsilon_z, E_\mathrm{L})$. This process was repeated for scaled noise amplitude σ in the range 0 to +0.5 (red dots) and 0 to -0.5 (blue dots). Again, the solutions to the estimations at each of these noise levels were projected in the $(\epsilon_z, E_\mathrm{L})$ plane. Note that the choice of plane is arbitrary. The same qualitative results are observed in other projection planes. At $\sigma = 0$, the parameter solution remains the local minimum (Figs. 3.4(b,c), magenta star), as expected. In the case of the

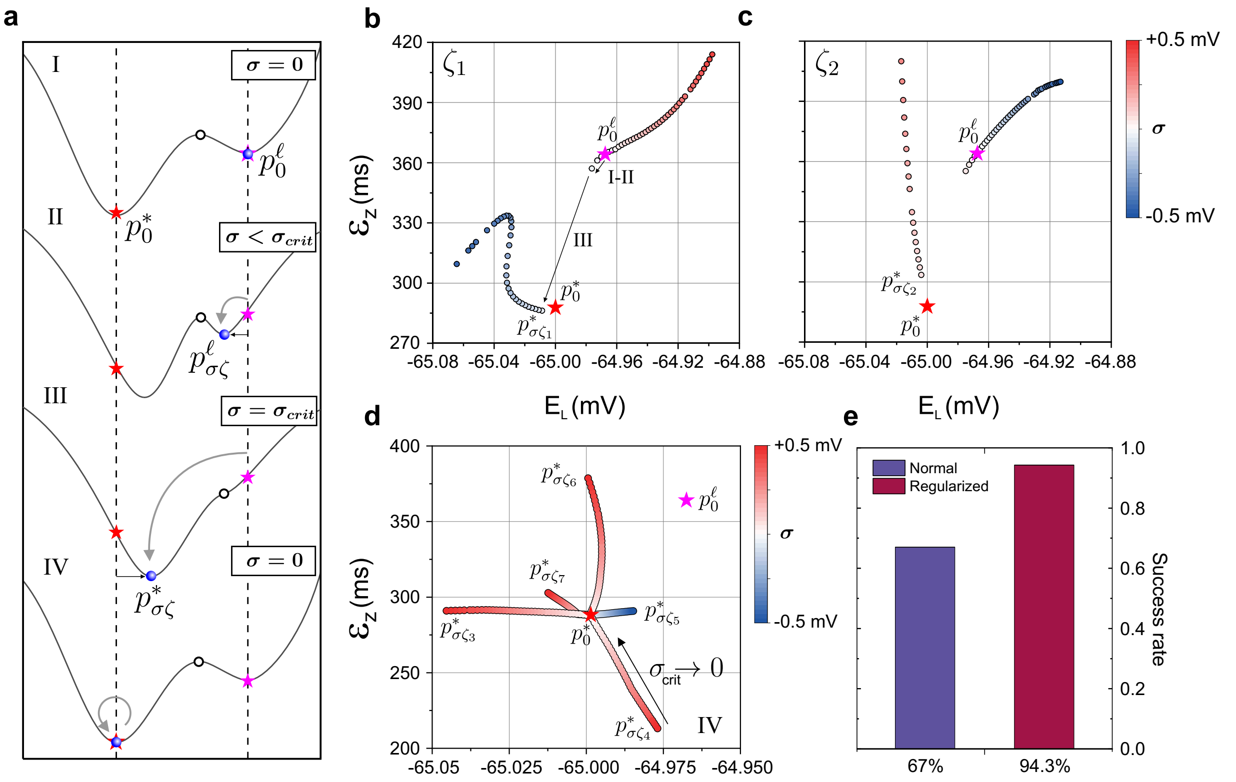

Figure 3.4: Noise-based regularization of parameter search. (a) Schematic profile of the data error misfit function δc plotted along a straight line passing through the global minimum p_0^* (red star) and the nearest local minimum p_0^l (magenta star). (I) In the absence of noise ($\sigma = 0$), the two minima p_0^l and p_0^* are separated by a saddle point (open dot). (II) By increasing the noise amplitude to a critical value $\sigma < \sigma_{\mathrm{crit}}$, one can shift the local solution, $\mathbf{p}_0^l \to \mathbf{p}_{\sigma\zeta}^l$, and the global solution, $\mathbf{p}_0^* \to \mathbf{p}_{\sigma\zeta}^*$ (blue dots). (III) At some critical amplitude σ_{crit}, the barrier vanishes as the local minimum $\mathbf{p}_{\sigma_{\mathrm{crit}}\zeta}^l$ merges with the saddle point. (IV) Parameter search initialized at $\mathbf{p}_{\sigma_{\mathrm{crit}}\zeta}^l$ now converges smoothly to the optimal solution p_0^* as the noise amplitude is reduced to zero. In this way, parameter search is regularized. (b) Trajectory traced by the local solution parametrized by noise as the noise amplitude is varied from $\sigma = -0.5$ mV to $+0.5$ mV. The amplitude of the noise is colour coded in each dot. The noise realization remains the same (ζ_1). The 41-dimensional trajectory is projected onto the arbitrarily-chosen 2D plane (E_L, ϵ_z). At $\sigma_{\mathrm{crit}} = -40\ \mu$V, $\mathbf{p}_{\sigma\zeta}^l$ merges with $\mathbf{p}_{\sigma\zeta}^*$ (step III). (c) Same as in (b) but for a trajectory calculated with a distinct noise realization, ζ_2. Here $\sigma_{\mathrm{crit}} = +50\ \mu$V. (d) Multiple different trajectories of the solution $\mathbf{p}_{\sigma\zeta}^*$ during step IV. The distinct starting points are the shifts induced by different realizations of noise, $\zeta_3, ..., \zeta_8$. (e) Probability of convergence to the optimal solution with (red) and without (blue) noise regularization. The success rate was calculated using a statistical sample of 150 parameter estimates performed from random parameter initializations.

first noise realization, ζ_1, for $\sigma > 0$, the local and global minima move away from one another causing $\mathbf{p}^{\ell}_{\sigma\zeta}$ to shift monotonically away from $\mathbf{p}^{*}_{\sigma\zeta}$ as σ increases (red dots). In contrast, when $\sigma < 0$, the distance between the two minima decreases. At a critical value of noise amplitude $\sigma_{crit} = -40$ μV, the saddle point vanishes, and the solution of the estimation procedure abruptly transitions from the local minimum $\mathbf{p}^{\ell}_{\sigma\zeta}$ to the global minimum $\mathbf{p}^{*}_{\sigma\zeta}$. The effect of using a different noise realization ζ_2 in Fig. 3.4(c) is to change the path traced by the solutions in parameter space. In this instance, the local and global minima move away from one another for $\sigma < 0$. For ζ_2, the saddle-node bifurcation occurs at a positive noise amplitude of $\sigma_{crit} = +50$ μV.

Steps (iii) to (iv) of the regularization method are demonstrated in Fig. 3.4(d). The optimal solution $\mathbf{p}^{*}_{0}$ was then recovered by ramping down the amplitude from σ_{crit} to zero. Fig. 3.4(d) shows the trajectories traced for five different noise realizations $\zeta_1 \ldots \zeta_5$ as σ is progressively decreased from σ_{crit}. In each case, the shifted parameter solution $\mathbf{p}^{*}_{\sigma\zeta}$ converges to $\mathbf{p}^{*}_{0}$. Fig. 3.4(d) thus demonstrates the dependence of the noise-induced parameter offset on noise realization, as predicted by Eq. 3.14.

This experiment verifies experimentally that harnessing the effect of noise on parameter solutions can be used to regularize convergence towards the global minimum. The algorithm of the regularization method can be summarized as follows: (i) first, solve the inverse problem using smooth data. The estimation procedure will arrive at either a global or local minimum, corresponding to an optimal or sub-optimal solution, respectively; (ii) the second step is to apply a realization of additive noise to the data and scale its amplitude until an abrupt step in both $\delta\mathbf{p}$ and δc is encountered; (iii) finally, progressively reduce noise amplitude to zero to obtain the optimal parameter solution. Using this algorithm for the RVLM neuron model starting from $R = 150$ random parameter initializations was found to boost the probability of reaching the optimum solution from 67% to 94.3% (Fig. 3.4(e)). In the remaining 33% and 5.7% of cases, respectively, the estimation terminated at local minima in the search space. In the case of more complex neuron models, for which the initial probability of finding the optimal solution is necessarily lower, this algorithm may prove an even more powerful regularization method than this experiment demonstrates.

3.3.5 Reducing parameter correlations

When performing parameter estimation of neuron models from observed membrane voltage data, it is important that the time series data contain sufficient information to constrain the model parameters. Large parameter uncertainties and correlations can arise if this criterion is not fulfilled. For conductance-based neuron models, this means that the assimilation window must contain examples of depolarization, hyperpolarization, and action potentials. To satisfy this, the current protocols used to stimulate the neuron must: (i) include current steps of different durations to probe the recovery of ionic gates with different kinetics, and current steps of different amplitude to extract information from the depolarized, sub-threshold and hyperpolarized states of a neuron; (ii) be sufficiently long to encompass multiple spikes, since most model parameters control the dynamics of depolarization and neuron spiking. Increasing the window length can therefore contribute to better constrained global parameter solutions and less correlated parameters. However, as the window length increases, the cost function is known to become highly irregular with an increasing number of local minima. This effect has been discussed extensively, specifically in the geophysical literature [168, 169].

In order to increase the length T of the assimilation window while keeping the cost function sufficiently regular, a smart sampling method was implemented which sampled sub-threshold dynamics with a larger step size than for action potentials. For values of membrane voltage above some threshold, say, -65 mV, a step size of $\Delta t_1 = 10$ μs was applied, while membrane voltage values below this threshold were sampled with a larger step size $\Delta t_2 = n\Delta t_1$. For the results presented below, a threshold value $V_{\text{thresh}} = -65$ mV was chosen. Since, for neuron models, sub-threshold dynamics are controlled by fewer parameters than depolarized states, this approach allows for considerable increases in the duration of the assimilation window without increasing the number of data points in the problem. This has the additional benefit of keeping the computation time roughly constant, even as the window duration is increased. In this section, the effects of both (i) stimulation complexity and (ii) assimilation window length on the correlations and uncertainties of estimated parameter sets were explored.

First, the effect of the assimilation window length on parameter correlations

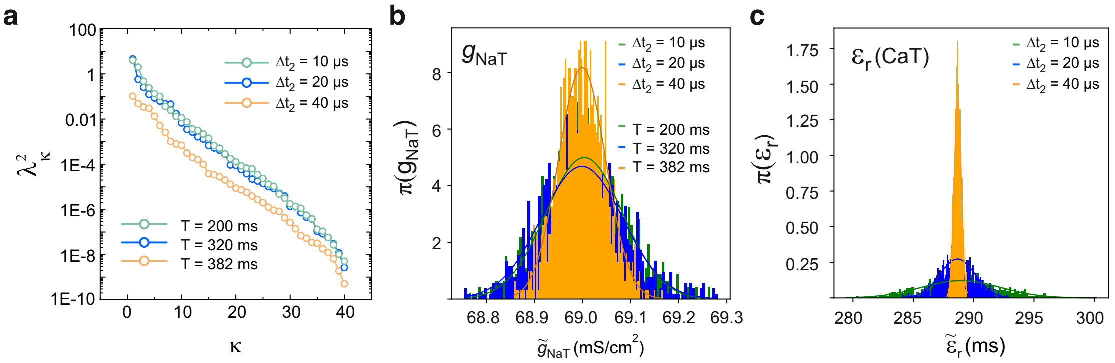

Figure 3.5: Increasing the total duration of the assimilation window reduces the uncertainty on estimated parameters. An adaptive step size was implemented to increase the duration of the assimilation window without increasing the total size of the problem ($n = 10,000$ samples). The base step size was $\Delta t_1 = 0.01$ ms during the depolarization time intervals ($V_{\rm exp} > -65$ mV) and $\Delta t_2 = m\Delta t_1$, $m = 1, 2, 4$, elsewhere ($V_{\rm exp} \geq -65$ mV). (a) Dependence of the parameter correlations on the duration of the assimilation window as it was increased from $T = 200$ ms ($m = 1$), 320 ms ($m = 2$) to 382 ms ($m = 4$). Additive noise had amplitude $\sigma = 0.25$ mV. (b,c) Posterior distribution functions of two parameters chosen for their contribution to distinct dynamics at increasing window durations. (b) PDFs for g_{NaT}, a parameter governing action potentials via the sodium current. (c) PDFs for ϵ_r, which governs *sub-threshold oscillations* via calcium kinetics. These PDF historgrams were generated using 1000 assimilations initialized at the global minimum, each with a unique noise realization.

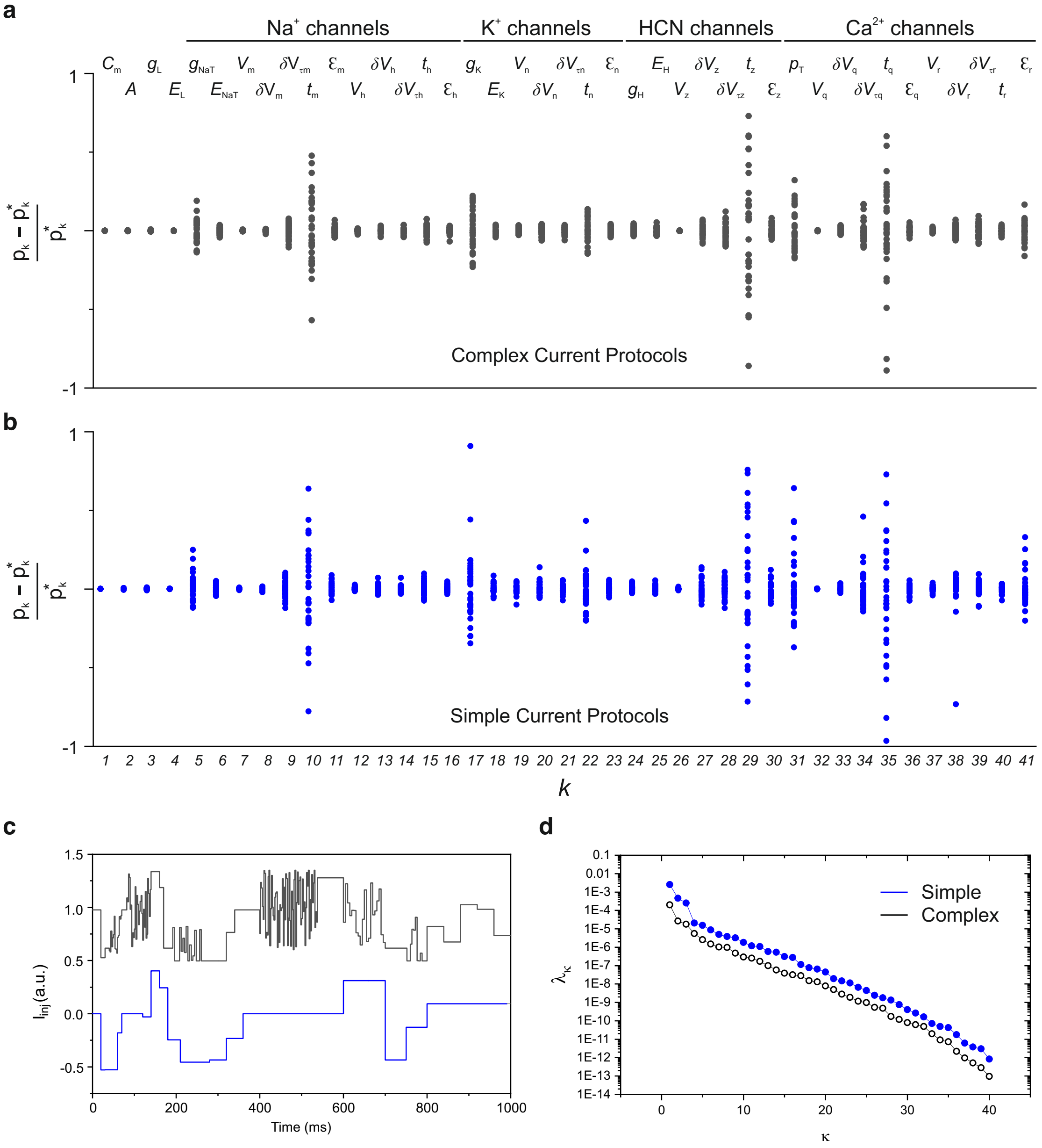

Figure 3.6: Dependence of parameter identifiability on the complexity of the stimulating current. (a) The dispersion of estimated parameters for the RVLM neuron model driven by a complex current stimulation protocol (grey line). (b) Same as (a) for a simpler current (blue line) composed of slower changing and longer-duration current steps. (c) Complex (grey) and simple (blue) current protocols used to stimulate the neuron and to constraint the parameters obtained in (a) and (b). (d) Size-ranked eigenvalue spectra for the covariance matrices $\hat{\mathbf{\Sigma}}$ of parameters estimated using the two current protocols in (c).

was investigated by computing the eigenvalue spectra of the covariance matrix $\hat{\mathbf{\Sigma}}$ (Fig. 3.5(a)). The covariance matrix was generated by performing an ensemble of $R = 1000$ assimilations, each with a distinct additive noise realization of amplitude $\sigma = 0.75$ mV. The assimilation window had $N = 10,001$ data points with non-uniform time steps as determined by the adaptive step method previously described. Fig. 3.5(a) plots the eigenvalue spectra for assimilation windows of increasingly long duration, corresponding to $\Delta t_1 = 10$ μs ($T = 200$ ms), 20 μs ($T = 320$ ms), 40 μs ($T = 382$ ms). It is clear from the results that increasing the duration of the assimilation window significantly reduces parameter correlations, λ_k^2, for all 41 parameters. This can be compared with Fig. 3.2(f) where some parameter correlations remain even as the noise intensity tends to zero. Fig. 3.5(b) plots the PDFs of the parameter g_{NaT} for increasing T. Since maximal conductance parameters are relatively well-constrained, the PDF does not narrow considerably with increasing window duration. In contrast, the PDF of the parameter ϵ_{CaT} becomes significantly narrower as T increases (Fig. 3.5(c)). For loosely-constrained parameters governing recovery time constants, the standard deviation of the PDFs were found to decrease by orders of magnitude as the duration of the assimilation window increased from $T = 200$ ms to 382 ms. A second advantage of using the adaptive step size method is that it facilitates longer assimilation windows, allowing longer current steps to be applied (500 ms). This is essential to quantify the effect of slow decaying currents on their long term modifications of neuron properties [170].

Secondly, the effect of current stimulation complexity on parameter correlations and uncertainty was investigated. The eigenvalue spectrum of the covariance matrix $\hat{\mathbf{\Sigma}}$ was first computed for an ensemble of $R = 1000$ assimilations performed using membrane voltage data generated using a complex current injection protocol. The parameter spreads for this ensemble are shown in Fig. 3.6(a), again for a noise level of $\sigma = 0.75$ mV. A sample of the protocol used is shown in Fig. 3.6(c). This experiment was then performed using a less complex current protocol, with slower changing current steps of longer duration (Fig. 3.6(c)). The parameter spreads for this experiment are shown in Fig. 3.6(b) for a noise level of $\sigma = 0.75$ mV. It is clear that the current protocol consisting of long rectangular steps fails to constrain the model parameters as successfully as the more complex protocol. The eigenvalue spectra of the covariance matrices of the two experiments are shown in Fig. 3.6(d). In the case of the more complex current protocols, parameter correlations are uniformly depressed. These results demonstrate the importance of selecting appropriate stimuli that probe the full dynamic range of the neuron for parameters to be identifiable.

3.3.6 Dependence of predictions on parameter accuracy

We now compare the predictions of models configured with optimal versus sub-optimal parameter sets. In this section, we demonstrate that predictions made with sub-optimal parameters ($\mathbf{p}_0^v$ or $\mathbf{p}_0^\ell$) are always discernible from those made with the optimal set $\mathbf{p}_0^*$. The RVLM model was configured with 3 sets of parameters: the zero-noise global minimum, $\mathbf{p}_0^*$, a local minimum $\mathbf{p}_0^\ell$, and $\mathbf{p}_0^v$, a vicinal location to the global minimum defined as the global minimum shifted by noise. These parameters are listed in Table 3.2. Fig. 3.7(a) shows the locations of the local minimum $\mathbf{p}_0^\ell$ (purple dot) and the vicinal minimum $\mathbf{p}_0^v$ (orange dot) on the cost function surface relative to $\mathbf{p}_0^*$ (red dot). The distance in parameter space to the optimum solution was evaluated using the Euclidean norm $\|\mathbf{p}-\mathbf{p}_0^*\|$. The predictions $V_{\text{pred}}(t_n)$ of the neuron model configured with the three parameter sets $\mathbf{p}_0^*$, $\mathbf{p}_0^v$ and $\mathbf{p}_0^\ell$ are shown in Fig. 3.7(b), (c) and (d) respectively (red lines). These are plotted on top of the model data $V_{\text{mod}}(t_n)$ (black line) generated using the true parameter set $\mathbf{p}_{true}$. The prediction error $\Delta V(t_n) = |V_{\text{pred}}(t_n) - V_{\text{mod}}(t_n)|$ is the cyan line (Fig. 3.7(b-d)). Predictions obtained using the global minimum parameter set $\mathbf{p}_0^*$ are nearly identical to the model data. In contrast, the predictions obtained using the vicinal minimum parameter set $\mathbf{p}_0^v$ show multiple discrepancies in depolarized regions, especially at the site of action potentials (Fig. 3.7(c)). The height of the action potential peaks is often incorrect, and spike bursts are incorrectly predicted as individual action potentials. Sub-threshold, the predictions are still very accurate, however. Finally, predictions made using the local minimum parameter set $\mathbf{p}_0^\ell$ result in some spurious extra spikes, in addition to sites where spikes are missing compared to the true model data. (Fig. 3.7(d)). Fig. 3.7(a) shows that both of the sub-optimal minima used to generate predictions are not particularly far away from the global minimum in cost function space. Despite

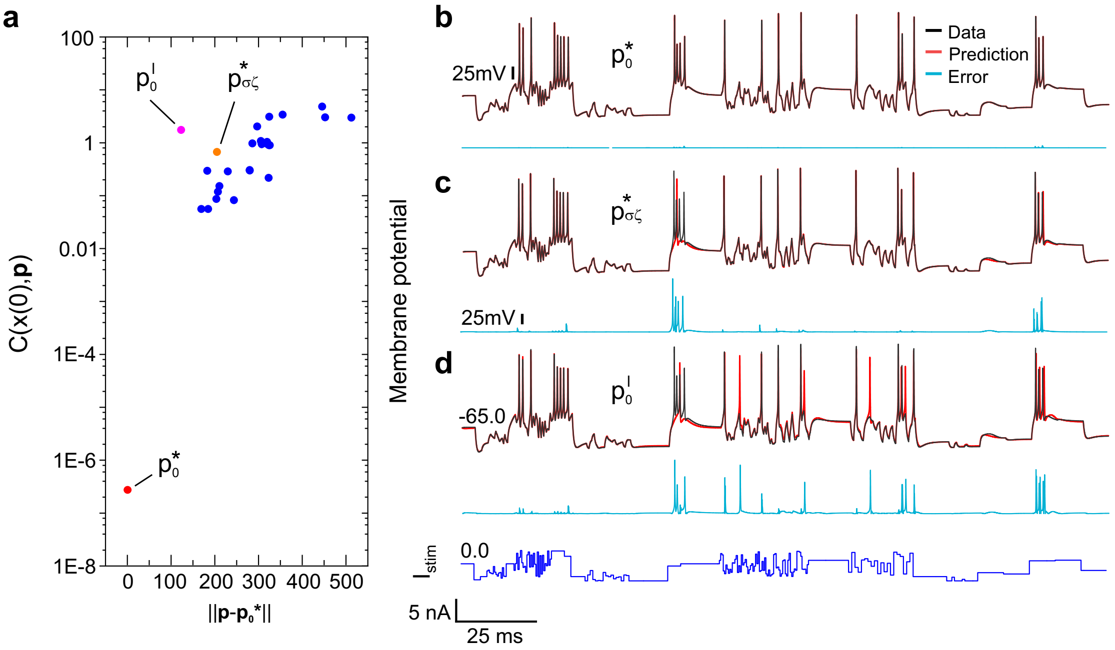

Figure 3.7: Effect of optimal and sub-optimal parameters on model predictions. (a) The value of the cost function at the site of sub-optimal local minima (purple/orange/blue dots) in the vicinity of the global minimum (red dot) plotted as a function of the Euclidean distance to the global minimum. The blue dots correspond to local minima situated further away from the global minimum. (b-d) Reference membrane voltage (black trace) generated using the current protocol (blue line, bottom). The membrane voltage (red lines) predicted by configuring the RVLM model with parameters: (a) $\mathbf{p}_0^*$, (b) $\mathbf{p}_{\sigma\zeta}^*$, (c) $\mathbf{p}_0^l$. The difference between the predicted voltage and the reference voltage is the prediction error (cyan lines).

this, the predictions still generate sizeable discrepancies relative to the true model data. This suggests that only the original parameters are capable of predicting the experimental time series, provided the stimulating current is sufficiently discriminating. In other words, the current here allows the system to fulfill the identifiability condition. The membrane voltage time series data contains enough information to possess a single-valued parameter solution, as described by Takens' theorem.

3.4 Discussion

In this chapter, it is argued that the parameters and initial conditions that control neuronal oscillations can generally be inferred from the observation of its membrane voltage over a finite time interval [148, 149, 171], provided that certain conditions are satisfied. By recovering the original model parameters in twin experiments, it was shown that the condition of observability can be satisfied by conductance-based neuron models. The second condition, parameter identifiability, requires that the system be driven by a sufficiently complex external stimulus to constrain all parameters. It was demonstrated in Fig. 3.6 that parameter sets inferred from data generated using simpler stimuli are less identifiable and are therefore poorly constrained compared to those listed in Table 3.2 ($\mathbf{p}_0^*$). This proves that driving the neuron across a wide dynamic range is therefore a necessary condition for guaranteeing identifiability.

In addition, this chapter presented novel approaches to help to mitigate the pervasive ‘sloppiness’ of biological models [136]. By using an adaptive time step method to increase the duration of the assimilation window, it was shown that parameter uncertainties as well as the correlations between parameters could be uniformly reduced, while avoiding a more irregular cost function landscape. The result of this is increased parameter identifiability (Fig. 3.5). In summary, if an experimenter is able to meet the conditions of observability and identifiability, sub-optimal parameters can be forced to give sub-optimal predictions, even when these parameter solutions are very close to the optimal solutions in parameter space (Fig.3.7). Therefore, it has been shown that single-valued solutions are accessible to parameter estimation algorithms, even when the model is complex.

Another challenge addressed in this chapter is the presence of local minima in the cost function. When data are distorted by experimental error, local minima become difficult to distinguish from the true global minimum. In Fig. 3.4, a regularization method was presented that makes constructive use of additive noise to destabilize local minima through saddle-node bifurcations, allowing gradient descent methods to arrive at the global optimum solution with a increased probability of 94%. This work examined separately the effect of experimental and model error on perturbations to parameter solutions. By expanding the cost function in the vicinity of minima in the search space, it was found that both forms of error shift the parameter solution on the data misfit surface in particular ways. The primary cause of this offset is experimental error, with model error providing a second order contribution.

These results show that even when biological systems exhibit a high degree of parameter sloppiness, the underlying parameter configuration may still be determined provided a sufficiently discriminating external driving is applied. Therefore, the degree of parameter identifiability attainable is always relative to the degree of sophistication of external stimulation of the physical system. While recent work has found similar network activity arising from disparate circuit parameters in self-sustaining oscillator networks, such as central pattern generators operating in the steady-state without external input [138, 139, 172, 173], this chapter argues that subjecting central pattern generators to a wider range of entrainments would further reduce the set of parameters compatible with the observed outputs, up to the point where a unique parameter solution would remain that characterises all electrical properties. There is therefore no theoretical limitation to inferring the underlying structure of ion channels or connectivity of small networks above and beyond designing stimulation protocols that fulfill identifiability conditions.

In this chapter, we applied data assimilation to a model problem in which the system generating the data is identical to the model we sought to optimize. In the next chapter, we extend the methods presented here to the optimization of artificial silicon neurons using electrophysiological recordings. By configuring individual ion channels of a solid-state neuron model with parameters estimated from the assimilation of biological data, we are able to successfully transfer the complete dynamics of hippocampal and respiratory neurons *in-silico*. In doing so, we demonstrate that the parameter estimation procedure developed in this chapter remain highly effective in the presence of real-world data and in situations where the inverse problem is ill-posed.

Chapter 4

Optimizing solid state neurons

4.1 Introduction

Computational models have been used to explore the properties of neural systems at every level of neuroscience, from the molecular and cellular level to the systems and cognitive level [102, 174, 175]. With the advent of neuromorphic engineering, the ability of researchers to construct detailed *hardware* models of neural system is now growing [176, 177]. The central goal of neuromorphic engineering is the design of integrated electronic systems that emulate the function and structure of biological neural systems. By exploiting analogies that exist between the gating kinetics of biological neuron channels and the physics of semiconductor devices, neuromorphic electronics can mimic neural circuitry in ever-greater detail [178]. These devices are typically fabricated from analog very-large-scale integrated (VLSI) circuitry with very low power consumption, and can be configured to behave in a qualitatively similar way to biological neurons. Although many silicon neurons and synapses have been designed in recent years [41, 179–181], the purpose of these devices was not to replicate the behaviour of biological cells in full and complete detail. Rather, these devices are typically designed for objectives including course-grained emulation of general neurobiological architectures [182, 183], bio-inspired computing technologies [184, 185], and high level machine-learning applications [186, 187]. In contrast, bioelectronic medicine is now driving the need for hyper-realistic neuromorphic circuits that interface with nervous systems, integrating raw nervous stimuli and responding identically to biological neurons. An increasing focus on implantable bioelectronics for treating chronic disease is instilling new urgency in the need for low-power analogue solid state devices that accurately mimic biocircuits [188].

Building high-fidelity solid state neurons requires a systematic method for estimating the optimal parameters of reconfigurable circuitry that reproduce recorded electrical responses. In recent years, many parameter estimation approaches have been applied to the problem of constructing *numerical* neuron models. These approaches range from hand-tuning [189] and trial-and-error fitting [190, 191] to genetic algorithms, Bayesian inference and statistical interpolation [121, 192, 193]. Most of these methods have been successful in estimating linear parameters such as maximal ionic conductances. In Chapter 3, constrained nonlinear optimization was employed to estimate nonlinear parameters, such as voltage thresholds and recovery times, which are essential for accurately predicting dynamical features such as spike timings. The problem of applying these data assimilation methods to transferring information from a biological cell to biomimetic *hardware* is met with additional difficulties that arise from fabrication constraints [194, 195]. For example, conventional neuromorphic circuitry assigns a constant slope to the steady-state activation function of ion channels [196]. In biology, this slope factor varies across neuron types and between ion channels. A more biologically plausible neuromorphic design is therefore needed, with the additional requirement that its mathematical description be compatible with nonlinear optimization methods. This neuromorphic design could then be configured with a set of optimal parameters such that its response to external stimuli is identical to to that of a biological neuron.

In this chapter, we describe a novel analogue circuit design that is capable of modelling any generic ion channel. By performing *ab-initio* analysis of the silicon components of a solid state neuron (SSN) implementing these ion channels, the equations describing the evolution of the membrane voltage and gating variables of the SSN are derived. This mathematical model of the SSN shares similarities with the Hodgkin-Huxley model, however it derives from the equations governing current flow through transistors operating in the weak inversion (or sub-threshold) domain. The model embodies the variable slopes of activation curves and time constants associated with gating kinetics, allowing parameters extracted from model optimization to be automatically tuned in the electronic device. A three ion channel SSN model that included a transient sodium current, a non-inactivating potassium current, and a leakage current was constructed and was found to predict the spike timings of the Hodgkin-Huxley model with 96.4% accuracy. Finally, a six-channel silicon neuron was constructed that faithfully modelled the dynamics of a CA1 hippocampal pyramidal neuron, and a five-channel silicon neuron was optimized to accurately predict the dynamics of a respiratory neuron. The completed models predicted the membrane voltage of biological neurons with high fidelity, demonstrating the possibility of fabricating bionic neurons that can accurately reproduce the response of biological cells through the use of data assimilation.

The chapter is structured as follows. The first section describes the biomimetic solid state ion channel that will be configured using data assimilation methods, and discusses how the channel differs from traditional conductance-based neuron models. A mathematical description of the hardware is derived from a first-principles analysis of the semiconductor physics. The second section presents the successful transfer of information from the Hodgkin-Huxley model membrane voltage data to a solid state neuron comprised of a VLSI sodium and potassium channel. Predictions generated using the configured solid state neuron are compared to the Hodgkin-Huxley output, and a high degree of agreement between the two is found. Finally, after validating the parameter estimation process in this way, the third section presents the results of assimilating biological neuron recordings into a more complex silicon neuron model, comprised of up to six active biomimetic ion channels. The final section gives a discussion of the results, and details promising applications of the presented methods.

4.2 Methods

4.2.1 Building solid-state neurons

Biomimetic solid-state ion channel.

The solid-state ion channel described in this chapter is composed of complementary metal-oxide-semiconductor (CMOS) transistors, and exploits the similarities in the underlying physics of these devices and of biological ion channels. The circuit diagram for this channel is shown in Fig. 4.1. The channel is composed of an activation sub-circuit denoted m, and an inactivation sub-circuit denoted h. Unlike in the Hodgkin-Huxley framework where the gating variables are multiplied together, in our biomimetic ion channel the net ionic current is given by the difference between the activation current I_m and the inactivation current I_h output from the two sub-circuits, respectively. The maximum ionic conductances are set by the source currents $I_{g\gamma}$, while the recovery time constants are set by the source currents $I_{\tau\gamma}$ and $I_{T\gamma}$. The threshold voltages of the ionic gates are $V_{t\gamma}$, where $\gamma \in \{m, h\}$. By tuning these parameters, the solid-state ion channel may be configured to mimic any individual channel type thought to be present in a particular biological neuron. As many channels as deemed necessary can then be added to the neuron membrane circuit. As discussed in previous chapters, we know that the gate recovery time of the majority of biological ion channels is membrane voltage-dependent. This dependence is described by the equation $\tau(V) = t_0 + \epsilon \left[1 - \tanh^2 \frac{V - V_t}{\delta V_\tau}\right]$, which is a bell-shaped curve with width δV_τ centred on the (in)activation voltage V_t, and where t_0 and $t_0 + \epsilon_0$ are the base and peak latency times, respectively. These biological kinetics $\tau_\gamma(V)$, $\gamma \in \{m, h\}$ are represented in our solid-state channel by the current $I_{\Sigma\gamma}$ in Fig. 4.1(a). By connecting in series n-type and p-type differential pair circuits (Fig. 4.1(c)), a bell-shaped dependence is obtained. The first, n-type, differential pair outputs a sigmoidal current $I' = I_{\max} \left[1 + \tanh \beta(V - V_{t\gamma})\right]/2$, which acts as the source current for the p-type differential pair circuit, which in turn outputs the current $I = I' \left[1 + \tanh \beta(V - V_{t\gamma})\right]/2$. This product of activating and inactivating characteristics produces the bell-shaped dependence of $I_{0T\gamma}$.

We can add a constant current $I_{\tau\gamma}$ to $I_{0T\gamma}$ to obtain:

$$I_{\Sigma\gamma} = I_{\tau\gamma} + \frac{I_{T\gamma}}{4}\left[1 - \tanh^2\beta(V - V_{t\gamma})\right], \tag{4.1}$$

which can be compared with $\tau_\gamma(V)$, $\gamma \in \{m, h\}$. This result assumes that the component transitors are operating in their sub-threshold regime for which $\beta = \kappa/(2U_T) \approx 14\text{V}^{-1}$, $U_T \approx 25$ mV is the thermal voltage, $\kappa = C_{Ox}/(C_{Ox+C_D}) \approx 0.7$ and C_{Ox} (C_D) is the capacitance of the oxide (depletion) layer.

The analogue current multiplier circuit works as follows. $I_{\Sigma\gamma}$ is injected into one of its inputs, while the other input receives the displacement current $I_{C\gamma} = C_\gamma dV_\gamma/dt$ through the capacitor C_γ. The output of the current multiplier is therefore $I_{C\gamma} = I_{\times\gamma} \times I_{\tau\gamma}/I_{\Sigma\gamma}$. The current $I_{X\gamma}$ is drained to ground by a current mirror, and is equated to the current output by the transconductance amplifier: $I_{\tau\gamma}\tanh\beta(V - V_\gamma)$. This sub-circuit determines the rate of change of the gating variable V_γ. If we substitute Eq. 4.1 into the equality $I_{C\gamma} = I_{\tau\gamma} \times I_{\tau\gamma}\tanh\beta(V - V_\gamma)/I_{\Sigma\gamma}$, we can write the equation of motion for the gate variable as:

$$C_\gamma\frac{dV_\gamma}{dt} = \frac{I_{\tau\gamma}\tanh\beta(V - V_\gamma)}{1 + \frac{I_{T\gamma}}{4I_{\tau\gamma}}\left[1 - \tanh^2\beta(V - V_{t\gamma})\right]}. \tag{4.2}$$

V_γ is equivalent to the membrane voltage delayed by some recovery time equivalent to $\tau(V)$. This delayed voltage is then fed into a differential pair sigmoidal circuit (Fig. 4.1(g)), generating the total gate current I_γ:

$$I_\gamma = \frac{I_{g\gamma}}{2}\left[1 + \tanh\beta(V_\gamma - V_{t\gamma})\right]. \tag{4.3}$$

Analogue interpolation of activation curves and gate kinetics

In biological neurons, the width of the kinetics bell-curves and slope of the activation sigmoids vary, while the corresponding parameter $\beta^{-1} \approx 71.4$ mV in the solid-state ion channel equations is fixed by the processing technology. Modelling biological neurons therefore demands a circuit design that can allow for a variable slope β_γ. To this end, we designed a new circuit composed of multiple differential pair circuits biased at different voltage thresholds $V_{t\gamma,i}$, and saturation currents

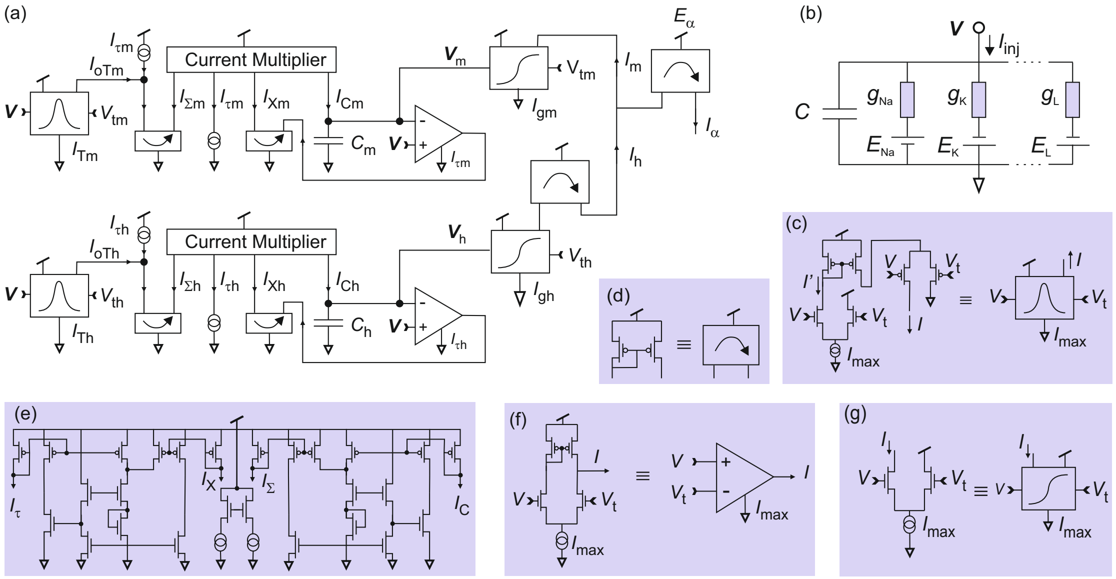

Figure 4.1: Biomimetic solid-state ion channel. (a) The conductance of a given ion species α is determined by the state of an activation gate and that of an inactivation gate. The net ionic current for the species $I_\alpha = (I_m - I_h)\theta(I_m - I_h)$ is given by the difference between the activation current (I_m) and the inactivation current (I_h). The Heaviside function, $\theta()$, specifies that the current mirror outputs a positive current I_α when $I_m > I_h$ and 0 otherwise. (b) Electrical equivalent circuit representation of the neuron membrane. (c-g) Block diagrams detailing the sub-circuits responsible for (c) the gate recovery time, (d) current mirror, (e) current multiplication $I_{C\gamma} = I_{\times\gamma} \times I_{\tau\gamma}/I_{\sum\gamma}$, where $\gamma \in \{m, h\}$, (f) transconductance amplification and (g) sigmoidal activation/inactivation.

$I_{\max,i}$, $i = 1, ..., n$. The sum of these currents interpolates the (in)activation according to:

$$I_\gamma = \sum_{i=1}^{n} \frac{I_{g\gamma,i}}{2} \left[1 + \tanh \beta(V_\gamma - V_{t\gamma,i})\right]. \tag{4.4}$$

In our SSN circuit, we therefore replace the static activation circuit (Fig. 4.1(a)) with this interpolation circuit to allow for the modelling of activation curves of arbitrary shape. Correspondingly, we will replace the static slope parameter β with the variable slope parameter β_γ in our SSN model equations. In a similar fashion, the width of the voltage-dependent kinetics is made to vary by summing the currents of n bell-shaped generating circuits biased to peak at threshold voltages $V_{t\gamma,i}$ with source currents $I_{T\gamma,i}$. A bell-shaped curve of arbitrary width can be interpolated according to:

$$I_{oT\gamma} = \sum_{i=1}^{n} I_{T\gamma,i} \left[1 - \tanh^2 \beta(V - V_{t\gamma,i})\right]. \tag{4.5}$$

We also replace the static bell-shaped generating circuit (Fig. 4.1) with the circuit in Fig. 4.2(c). Another hurdle that these substitutions allow us to overcome is the fact that in biological neuron models, the ionic current equations take the gate variables to an exponent: $I_\alpha = \overline{g}_\alpha m^p h^q (E_\alpha - V)$, where $\overline{g}_\alpha$ is the maximum conductance and E_α the ion reversal potential. To a first-order approximation, the exponents p and q increase the slope of activation curves from $1/\delta V_m \to p/\delta V_m$ and $1/\delta V_h \to q/\delta V_h$, while shifting the effective voltage thresholds V_{tm} and V_{th} higher. The above circuit modifications suffice in capturing these features of traditional conductance models in our SSN circuit.

SSN model equations of motion

We may now write the full set of equations of motion of the SSN model with the slope factor replacements $\beta \to \beta_\gamma$ and $\beta \to \beta_{\tau\gamma}$. The rate of change of membrane voltage is given by the Kirchhoff's current conservation equation applied to the electrical equivalent circuit of the neuron membrane (Fig. 4.1(b)). A solid state neuron incorporating Na$^+$, K$^+$, and leak channels (NaKL) obeys the following

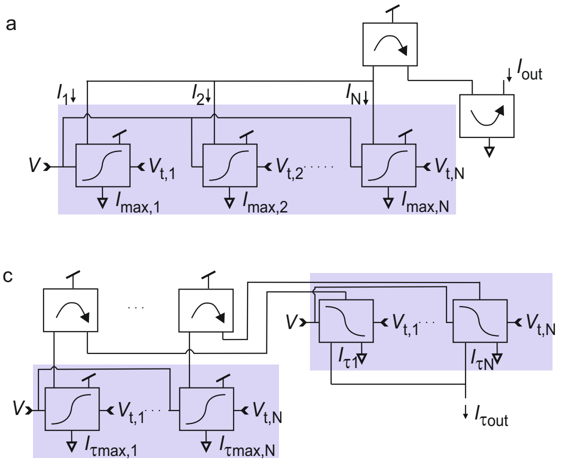

Figure 4.2: Analogue interpolation circuits for (in)activation curves and gating kinetics. (a) Sigmoidal currents are summed to interpolate the activation or inactivation curves of an ionic gating variable. Voltage thresholds $V_{t1}, ..., V_{tN}$ and source currents $I_{\text{max},1}, ..., I_{\text{max},N}$ can be adjusted for fitting. (b) Bell-shaped currents are similarly superposed to generate gating kinetics curves. N bell-shaped curves centred at $V_{t1}, ..., V_{tN}$ with amplitudes $I_{\text{max},1}, ..., I_{\text{max},N}$ are summed to fit kinetics.

equations:

$$C\frac{dV}{dt} = (I_m - I_h)\theta(I_m - I_h) - I_n + I_L \tanh\beta_L(E_L - V) + \alpha I_{\text{inj}} + I_{\text{dark}},$$

$$\frac{V_m}{dt} = \frac{\tilde{I}_{\tau m}\tanh\beta(V - V_m)}{1 + \frac{\tilde{I}_{Tm}}{4\tilde{I}_{\tau m}}\left[1 - \tanh^2\beta_{\tau m}(V - V_{tm})\right]}, \qquad I_m = \frac{I_{gm}}{2}\left[1 + \tanh\beta_m(V_m - V_{tm})\right],$$

$$\frac{V_h}{dt} = \frac{\tilde{I}_{\tau h}\tanh\beta(V - V_h)}{1 + \frac{\tilde{I}_{Th}}{4\tilde{I}_{\tau h}}\left[1 - \tanh^2\beta_{\tau h}(V - V_{th})\right]}, \qquad I_h = \frac{I_{gh}}{2}\left[1 + \tanh\beta_h(V_h - V_{th})\right],$$

$$\frac{V_n}{dt} = \frac{\tilde{I}_{\tau n}\tanh\beta(V - V_n)}{1 + \frac{\tilde{I}_{Tn}}{4\tilde{I}_{\tau n}}\left[1 - \tanh^2\beta_{\tau n}(V - V_{tn})\right]}, \qquad I_n = \frac{I_{gn}}{2}\left[1 + \tanh\beta_n(V_n - V_{tn})\right],$$

(4.6)

where $\theta()$ is the Heaviside step function. Because the rate of change of the gating variables in Eq. 4.2 depends on both a capacitance C_γ and a source current $I_{\tau\gamma}$, one can define the ratio $\tilde{I}_{\tau\gamma} = I_{\tau\gamma}/C_\gamma$, for $\gamma \in \{m, h, n\}$. This removes a parameter degeneracy during the assimilation procedure, since these two parameters are directly correlated in the equations, and has the advantage for VLSI design that capacitances may be made as small as desired provided that the source currents are adjusted accordingly. We have included a parameter I_{dark} which accounts for the leakage current of sub-threshold circuit components when in the OFF state. This current is far smaller than ionic currents, but will need to be accounted for in the model. We have also introduced a scaling parameter α which amplifies the injected current protocol. This is the silicon model equivalent of the neuron surface area parameter in the biological conductance model.

In summary, we have developed a biomimetic solid-state neuron with 22 independent parameters: I_{gL}, $I_{g\gamma}$, $\tilde{I}_{\tau\gamma}$, $\tilde{I}_{T\gamma}$, β_L, β_γ, $\beta_{\tau\gamma}$, E_L, and $V_{t\gamma}$ for $\gamma \in \{m, h, n\}$, which may be easily extended through the addition of additional ionic channels to the neuron membrane circuit. This versatility allows the modelling of the most complex neurons with solid-state devices. We have performed an *ab initio* analysis of the currents of the SSN hardware components, meaning that parameter estimation can be performed using the SSN model equations before configuring the hardware directly with the estimated parameters.

4.2.2 Electrophysiological protocols

Brain slice preparation.

The electrical response of hippocampal and respiratory neurons to complex current protocols were recorded in acutely isolated brain slices from male Han Wistar rats. Respiratory neuron recordings were obtained from postnatal day (P)1 to P3 rats, while hippocampal neuron recordings were taken from P16-17 rats. Rats were anaesthetized and decapitated, and the brains were subsequently sectioned in ice-cold slicing solution (NaCl, 52.5 mM; sucrose, 100 mM; glucose, 25 mM; $NaHCO_3$, 25 mM; KCl, 2.5 mM; $CaCl_2$, 1 mM; $MgSO_4$, 5 mM; NaH_2PO_4, 1.25 mM; kynurenic acid, 0.1 mM, and carbogenated using 95% O_2/5% CO_2). A Campden 7000 smz tissue slicer (Campden Instruments UK) was used to prepare transverse slices of 350 μm thickness, and rhythmically active transverse slices through the medulla at 400 μm thickness. Medullary slices contained the pre-Bötzinger complex as well as the hypoglossal motor nucleus (XII) and rootlets for cell identification. Slices were then submerged in artificial cerebrospinal fluid (aCSF) containing: NaCl, 124 mM; glucose, 30 mM; $NaHCO_3$, 25 mM; KCl, 3 mM; $CaCl_2$, 1.5 mM, $MgSO_4$, 1 mM; NaH_2PO_4, 0.4 mM. The slices were incubated at 30° C for 1-5 hours prior to use.

Current-clamp recordings.

Individual cells were visually indentified using an upright Axioskop 2 (Carl Zeiss) microscope using differential interference contrast optics. Respiratory neurons were identified by anatomical location as well as the phase of burst firing with reference to activity in the XII motor nucleus or rootlet. The submersion chamber was perfused with the aCSF at 2 ml min^{-1}, and all recordings were performed at 30±2°C. Patch pipettes were pulled from standard walled borosilicate glass (GC150F, Warner Instruments) and filled with an artificial intracellular solution composed of: potassium gluconate, 130 mM; sodium gluconate, 5 mM; HEPES, 10 mM; $CaCL_2$, 1.5 mM; sodium phosphocreatine, 4 mM; Mg-ATP, 4 mM, Na-GTP, 0.3 mM; pH 7.3. Recordings were performed in the presence of (μM) kynurenate, 3; picrotoxin 0.05; and strychnine, 0.01 to isolate the neuron from synaptic activity of neighbouring cells in the slice. Signals were obtained using a custom-build LabView interface through a USB-6363 DAQ card and a MultiClamp 700B amplifier. The membrane voltage time series and the injected current protocols were simultaneously recorded in current-clamp mode at a sampling rate of 100 kHz.

Generating current protocols.

In order to constrain neuron parameters pertaining to spiking activity and subthreshold activity, it was important that the current injection protocols contained both depolarizing and hyperpolarizing segments. Additionally, estimating parameters of dynamics which operate over a wide range of time scales demands that the protocols contain fast- and slow-changing currents. With this in mind, we designed a set of protocols composed of: (i) positive and negative current steps of different duration and amplitude, and (ii) chaotic oscillations generated by the x-variable of the hyperchaotic Bouali dynamical system [197]. The Bouali system is described by the following set of equations:

$$\frac{dx}{dt} = x(1-y) + \zeta z, \qquad \frac{dy}{dt} = \rho(x^2-1)y,$$
$$\frac{dz}{dt} = \gamma(1-y)v, \qquad \frac{dv}{dt} = \eta z, \tag{4.7}$$

and was used with the parameterization $(\zeta, \rho, \gamma, \eta)$ = (-2, 1, 0.2, 1). Prior to injecting these protocols into patch-clamped cells, a calibrating current consisting of positive depolarizing steps was injected to determine the minimum amplitude required to elicit neuron firing. The injected current protocols were then rescaled to the appropriate amplitude for an optimal recording.

4.3 Results

4.3.1 Transferring dynamics from HH to SSN

In order to demonstrate that our biomimetic solid-state neuron is capable of reiterating the dynamics of biological neurons, we now demonstrate the equivalence of the NaKL SSN model (Eq. 4.6) and the Hodgkin-Huxley (HH) model (Eq. 2.5) by predicting the response of the HH neuron with the NaKL SSN model. We begin with this approach for two principal reasons: firstly, we wish to validate that the gating variables V_γ of the SSN neuron, which are not accessible to observation in biological neurons, behave similarly to the gating variables of the neuron that we're modelling; secondly, we wish to assess the fidelity of information transfer between from one NaKL model to another. We began by building an NaKL conductance model configured with model parameters derived from a thalamic relay neuron [110]. The parameters for this model are listed in Table 4.1. We then forward-integrated the model in response to a range of current injection protocols (Fig. 4.3, blue traces) to generate an ensemble of membrane voltage time series (Fig. 4.3, black traces). The SSN model was then synchronized to the HH membrane voltage data over an assimilation window of length T = 1000 ms (green trace), giving the parameter estimates listed in Table 4.2. These parameters were used to complete the SSN model, which was forward-integrated from the end of the

Parameter ID	Value
C_m (uF/cm^2)	1
A	0.29
g_{NaT} (mS/cm^2)	69
E_{Na} (mV)	41
g_K (mS/cm^2)	6.9
E_K (mV)	-100
g_{Leak} (mS/cm^2)	0.465
E_L (mV)	-65
V_{tm} (mV)	-39.92
δV_m (mV)	10
$\delta V_{\tau m}$ (mV)	23.39
t_m (ms)	0.143
ϵ_m (ms)	1.099
V_{th} (mV)	-65.37
δV_h (mV)	-17.65
$\delta V_{\tau h}$ (mV)	27.22
t_h (ms)	0.701
ϵ_h (ms)	12.9
V_{tn} (mV)	-34.58
δV_h (mV)	22.17
$\delta V_{\tau h}$ (mV)	23.58
t_n (ms)	1.291
ϵ_n (ms)	4.314

Table 4.1: Parameters set in the Hodgkin-Huxley conductance model. These parameters were obtained from voltage-clamp data from a thalamic relay neuron [110].

assimilation window ($t = T$) onwards (Fig. 4.3, red trace) to generate a prediction of future membrane voltage for $t > T$. The estimated state of the neuron at the end of the assimilation window ($\boldsymbol{x}(t = T)$) provided the initial state for forward integration. Additionally, the completed model was used to generate predictions for two novel current protocols (Fig. 4.3(b), (c)), where the initial state of the neuron was assumed to be the equilibrium resting potential.

We now wish to quantify the quality of the match between our SSN model prediction and the 'true' data. Since we are interested in predicting both spike-timings and sub-threshold behaviour, we use two separate metrics: the so-called spike-coincidence factor, Γ, and the normalised root mean square deviation (NRMSD). Roughly speaking, the coincidence factor is a measure of spike-train synchrony

Ion	Parameter ID	Lower bound	Upper bound	Estimated value
NaT	$\tilde{I}_{gm}$ (nA pF^{-1})	0	200	162.75
	$\tilde{V}_{tm}$ (V)	0.01	1.8	0.908
	β_m (V^{-1})	1	100	8.405
	$\tilde{I}_{\tau m}$ (nA pF^{-1})	0.1	200	0.6854
	$\tilde{I}_{gh}$ (nA pF^{-1})	0	200	4.638
	$\tilde{V}_{th}$ (V)	0.01	1.8	1.143
	β_h (V^{-1})	1	100	3.581
	$\tilde{I}_{\tau h}$ (nA pF^{-1})	0.1	200	0.1482
K	$\tilde{I}_{gn}$ (nA pF^{-1})	0	200	164.18
	$\tilde{V}_{tn}$ (V)	0.01	1.8	0.911
	β_n (V^{-1})	1	100	8.372
	$\tilde{I}_{tn}$ (nA pF^{-1})	0.1	200	0.6747
L	$\tilde{I}_L$ (nA pF^{-1})	0	100	0.23105
	β_L (V^{-1})	1	100	1
	E_L (V)	0.001	1.8	0.6194
	α	1.00E-04	1000	39.54
	β (V^{-1})	14	14	14
	I_{dark} (nA pF^{-1})	-0.05	0.05	0

Table 4.2: Columns 3 and 4 specify the parameter search intervals used in data assimilation. Column 5 lists the SSN parameters estimated by assimilating the membrane voltage synthesized by the Hodgkin–Huxley (HH) model. I_{inj} had units of nA, and V, V_m, V_h and V_n units of V.

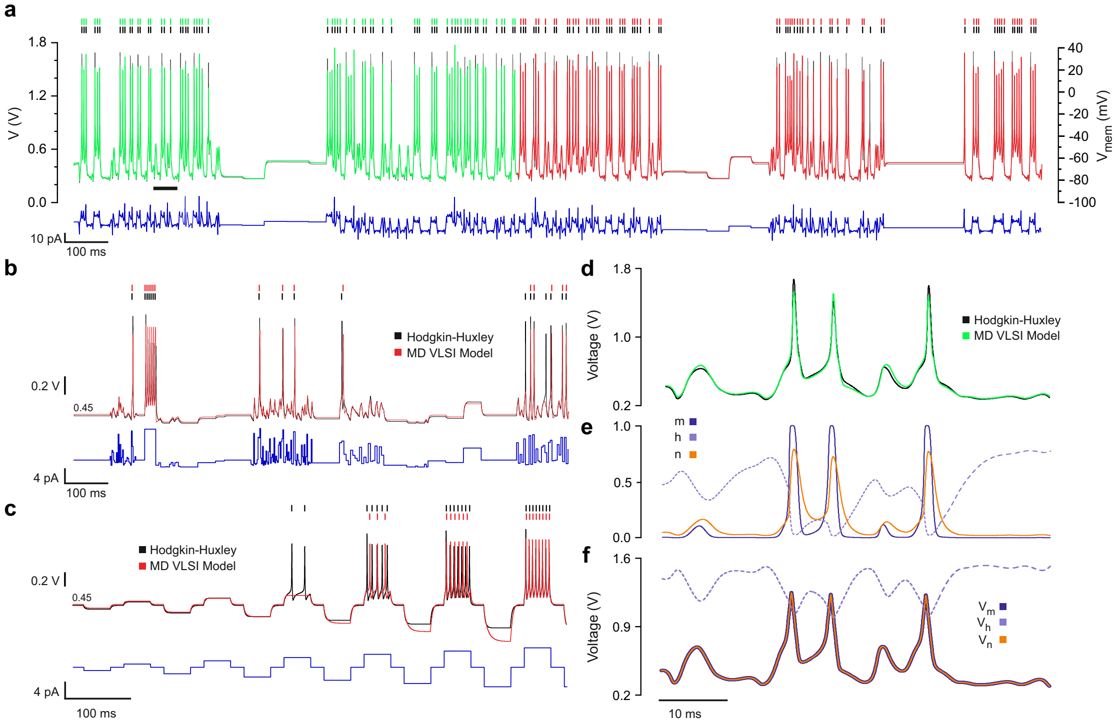

Figure 4.3: Demonstrating the equivalence of the NaKL SSN model and the Hodgkin–Huxley model. (a) The SSN model was synchronized to membrane voltage oscillations synthesized by the Hodgkin–Huxley model (black line). The Hodgkin–Huxley time series voltage was assimilated over a 1000-ms-long window (green line) under the constraints of the current injection protocol (blue line). The membrane voltage was then predicted from $t = 1000$ ms onwards by forward integrating the completed SSN model (red line) in response to the current protocol (blue line). (b), (c) Membrane voltages predicted by the same SSN model (red line) and HH model (black line) for two novel current protocols. (d) Expanded detail of the SSN and HH action potentials and a comparison of NaT and K gating variables in (e) the HH model and (f) the SSN model.

that estimates the similarity of two or more spike trains. It is computed as:

$$\Gamma = \frac{N_{\mathrm{coinc}} - \langle N_{\mathrm{coinc}} \rangle}{\frac{1}{2}(N_{\mathrm{data}} + N_{\mathrm{model}})} \frac{1}{N}, \tag{4.8}$$

where N_{data} denotes the number of spikes in the true (HH) time series, N_{model} denotes the number of spikes in the predicted (SSN) time series. N_{coinc} is the number of spikes between the two spike trains that coincide with precision $\Delta = 2$ ms. The quantity $\langle N_{\mathrm{coinc}} \rangle = 2fN_{\mathrm{data}}$ is the expected number of coincidences generated by a Poisson process with the same rate f as the predicted (SSN) spike train. The normalization factor $N = [1 - 2f\Delta]$ ensures that $0 \leq \Gamma \leq 1$, where $\Gamma = 1$ would correspond to a perfect match. For the data shown in Fig. 4.3, the spike coincidence factor between the HH and SSN models was calculated to be 97% in Fig. 4.3(a), and 91% in Fig. 4.3(b).

The second metric that we use to quantify the match between the two time series is $R^2 = 1$ - NRMSD, where NRMSD is the root mean square deviation between the data and the prediction, normalized by the amplitude of the membrane voltage oscillations (1.8V). For the predictions in Fig. 4.3, we find an average value of $R^2 = 96.4\%$. It is evident from Fig. 4.3(c) that the least well-constrained parameters are those corresponding to deeply hyperpolarized membrane voltage states. This demonstrates the importance of including strongly hyperpolarizing currents during the assimilation window. The weak hyperpolarization in Fig. 4.3(a) fails to fully constrain the sub-threshold parameters. The estimated threshold voltages $V_{t\gamma}$ are consistent with the relative values of the HH thresholds, and the estimated $\tilde{I}_{\tau\gamma}$ give biologically pausible recovery times: $t_{0,m} = U_T/\tilde{I}_{\tau_m} = 0.026/0.6854 = 0.03$ ms, $t_{0,h} = 0.026/0.1482 = 0.17$ ms, and $t_{0,n} = 0.026/0.6747 = 0.04$ ms. We note that the current injection scaling parameter is estimated to be $\alpha = 39.54$. This current re-scaling is necessary to account for the fact that the membrane voltage has been rescaled from the [-100 mV, +45 mV] range of the biological HH model to the [0, 1.8 V] range of the SSN neuron. Additionally, this parameter accounts for the surface area of the biological HH cell, which here is $ISA = 2.9 \times 10^{-4}\mathrm{cm}^2$. These considerations give $\alpha \approx (12.414/ISA + 1241.4)/1000 \approx 44$, which is consistent with the estimated value of $\alpha = 39.54$ (Table 4.2). Finally, let us consider the dynamics of the optimized SSN model. Fig. 4.3(d) shows that the spike waveforms of the SSN model (green trace) and the HH model (black trace) are nearly identical. The dynamics of the HH gating variables (m, h, and n) are shown in Fig. 4.3(e), while the SSN counterparts (V_m, V_h, and V_n) are plotted below in Fig. 4.3(f). These plots indicate that the internal dynamics of the two models share a number of common features, including the relatively slow kinetics of sodium inactivation, and the close correlation between the gating variables V_m and V_n (or between m and h in the HH model).

In summary, we now have a systematic methodology for transferring information from biological neurons to our SSN neuron model. We now proceed to demonstrate this same method for real biological neuron recordings. As mammalian neurons are more complex than the NaKL neuron considered above, we now expand the SSN model to include extra ionic currents.

4.3.2 Constructing a CA1 pyramidal cell model

By expanding the SSN model to include more ionic currents, it becomes possible to model and predict the dynamics of real biological cells. We constructed a silicon model of the CA1 neuron which included the ion channels present in high density in the soma and proximal dendrites (Table 4.3). These included the transient Na^+ current (NaT), the delayed-rectifier K^+ current (K), and the A-type K^+ current (A). Two non-inactivating currents were also included in the model: the persistent Na^+ current (NaP) and the muscarinic-sensitive K^+ current (M) [97, 198]. Although present in CA1 hippocampal cells, we excluded both the low threshold calcium current (CaT) [199, 200] and the hyperpolarisation-activated cation current (HCN) [201], since the density of these channels is low outside of distal apical dendrites far from the cell soma. Another current that was omitted from the model is the after-hyperpolarization K^+ (AHP) current that is sometimes observed in CA1 neurons during voltage-clamp experiments [202]. While this small-conductance current gives a minor contribution to spike-frequency adaptation under current-clamp conditions, its calcium dependency required its omission. The SSN model for a CA1 hippocampal neuron was thus expanded to include NaP, A and M currents in addition to the NaT, K and Leak currents of the smaller model. The mathematical description of this SSN model consisted of eight coupled differential

ID	Channel	Current density	CA1	R.N.
NaT	Transient Na^+	$J_{NaT} = g_{NaT} m^3 h (E_{Na} - V)$	Yes	Yes
NaP	Persistent Na^+	$J_{NaP} = g_{NaP} m (E_{Na} - V)$	Yes	Yes
K	Transient depol. activated K^+	$J_K = g_K m^4 (E_K - V)$	Yes	Yes
A	Rapidly inactivating K^+	$J_A = g_A m^4 h (E_K - V)$	Yes	Yes
AHP	Ca^{2+} activated K^+	$J_{AHP} = g_{AHP} m (E_K - V)$	D.D	Rare
CaL	High threshold Ca^{2+}	$J_{CaL} = \rho m^2 J_{Ca}$	D.D	Rare
CaT	Low threshold Ca^{2+}	$J_{CaT} = m^2 h J_{Ca}$	D.D	Rare
HCN	Hyperpol.-activated cation	$J_{HCN} = g_{HCN} h (E_{HCN} - V)$	D.D	D.D
M	Muscarinic-sensitive K^+	$J_M = g_M m (E_K - V)$	Yes	No
Leak	Leak channels	$J_L = g_L (E_L - V)$	Yes	Yes

Table 4.3: **Ion currents of CA1 hippocampal cells and respiratory neurons**. *RN* respiratory neuron, *D.D* distal dendrites. Ion current densities as a function of ionic conductances g_α, $\alpha \equiv \{$NaT, NaP, K, A, AHP, CaL, CaT, HCN, M, and Leak$\}$; the sodium and potassium reversal potentials, $E_{Na} \approx +45$ mV and $E_K \approx -90$ mV; the hyperpolarized-activated cation reversal potential E_{HCN}=-43 mV [203] and maximum calcium current J_{Ca}. The ionic currents of the solid-state model $I_\alpha = (I_m - I_h)\theta(I_m - I_h)$ are given by Eq. 4.6. Prevalence of ion channels in CA1 hippocampal pyramidal neurons and respiratory neurons distinguishing their presence in soma and in distal dendrites (D.D.).

equations.

Figure 4.4(a) shows the best fit of this model (green line) to the CA1 neuron data (black line) across a 1000-ms-long assimilation window. The estimated parameters are listed in Table 4.4 (CA1 → SSN). The SSN model was then completed with these parameters, and the membrane voltage was predicted from the end of the assimilation window. The 4000-ms-long prediction (red line) in response to the current protocol (blue line) is also shown in Fig. 4.4(a). The spike coincidence factor was 56% and the agreement between predicted and observed oscillations was $R^2 = 76\%$. A portion of the prediction window is expanded and presented in Fig. 4.4(b), for clarity. The predictive power of the CA1 SSN model was validated by predicting the membrane voltage in response to a number of similar current protocols, all of which gave similarly impressive results [81]. Fig. 4.4(c) presents the behaviour of all of the model state variables at the site of an action potential.

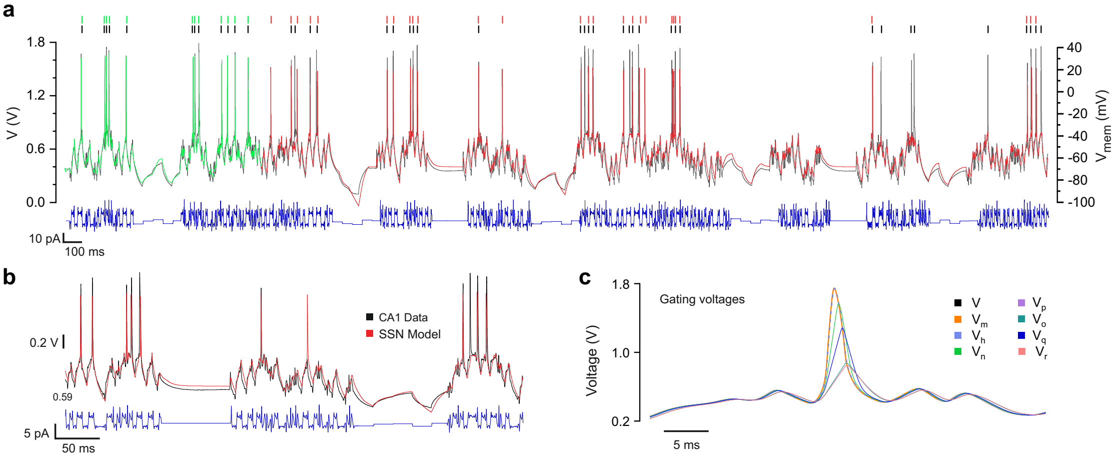

Figure 4.4: Assimilation and prediction of a CA1 pyramidal neuron. Membrane voltage oscillations of a pyramidal cell from the rat hippocampal cortex (black line) induced by the injection of a current protocol (blue line). The current trace shows the actual injected current, as measured. The CA1 SSN model was synchronized to the experimental membrane voltage over a $T = 1000$-ms-long assimilation window (green trace). The optimum fit produced an estimate of the model parameters shown in Table 4.4. Models completed by incorporating the optimal parameters were used to predict the membrane voltage from $t \geq T$ (red line). (b) Detail of the predicted membrane voltage over a short interval of the prediction window. (c) Detailed dynamics of the state variables of the SSN model during an action potential.

As in biological CA1 cells, the spike initiation is due to the fast activation of the NaT channel (V_m). Repolarization is subsequently initiated by the slower activation of the K^+ current (V_n). The channels with the slowest assigned activation kinetics were the M-type current (V_r), A-type current (V_o) and NaP current (V_p), as expected from the biology where these currents are known to be long-lived [204]. These results show that with a sufficiently realistic model, data assimilation can assign kinetic parameters consistent with the known biological properties of ion channels.

4.3.3 Constructing a respiratory neuron model

Next, we assimilated and predicted the membrane voltage of a respiratory neuron (RN) acquired from a slice of the Bötzinger region of the rat brain stem. First, we constructed a RN SSN model incorporating transient sodium (NaT), persistent

Ion	Parameter ID	Lower bound	Upper bound	RN→SSN	CA1→SSN
NaT	$\tilde{I}_{gm}$ (nA pF^{-1})	0	200	5.06291	15.3882
Activation	$\tilde{V}_{tm}$ (V)	0.01	1.8	0.60186	0.775011
	β_m (V^{-1})	1	100	4.3211	3.65247
	$\tilde{I}_{\tau m}$ (nA pF^{-1})	0.1	200	0.741963	200
Inactivation	$\tilde{I}_{gh}$ (nA pF^{-1})	0	200	3.87017	14.5214
	$\tilde{V}_{th}$ (V)	0.01	1.8	0.537676	0.761754
	β_h (V^{-1})	1	100	21.352	3.74198
	$\tilde{I}_{\tau h}$ (nA pF^{-1})	0.1	200	0.213195	1.90216
K	$\tilde{I}_{gn}$ (nA pF^{-1})	0	200	4.95587	1.05781
Activation	$\tilde{V}_{tn}$ (V)	0.01	1.8	1.1707	1.10211
	β_n (V^{-1})	1	100	4.95415	12.5939
	$\tilde{I}_{\tau n}$ (nA pF^{-1})	0.1	200	0.266346	0.48398
NaP	$\tilde{I}_{gp}$ (nA pF^{-1})	0.01	1.8	0.905	0.905
Activation	$\tilde{V}_{tp}$ (V)	1	100	50.5	50.5
	β_p (V^{-1})	0	200	100	100
	$\tilde{I}_{\tau p}$ (nA pF^{-1})	0.1	200	0.101315	0.101282
A	$\tilde{I}_{go}$ (nA pF^{-1})	0	200	3.25713	0.436843
Activation	$\tilde{V}_{to}$ (V)	0.01	1.8	0.527758	0.90838
	β_o (V^{-1})	1	100	4.79776	8.92825
	$\tilde{I}_{\tau o}$ (nA pF^{-1})	0.1	200	0.525516	0.110045
Inactivation	$\tilde{I}_{gq}$ (nA pF^{-1})	0	200	3.25878	199.914
	$\tilde{V}_{tq}$ (V)	0.01	1.8	0.533867	1.1711
	β_o (V^{-1})	1	100	22.552	100
	$\tilde{I}_{\tau q}$ (nA pF^{-1})	0.1	200	0.209388	0.267222
M	$\tilde{I}_{gr}$ (nA pF^{-1})	0	200	-	99.6646
Activation	$\tilde{V}_{tr}$ (V)	0.01	1.8	-	1.17193
	β_r (V^{-1})	1	100	-	54.7187
	$\tilde{I}_{\tau r}$ (nA pF^{-1})	0.1	200	-	0.10128
Leak	$\tilde{I}_L$ (nA pF^{-1})	0	100	0.010666	0.025847
	β_L (V^{-1})	1	100	100	10.8213
	E_L (V)	0.001	1.8	1.47205	0.233041
	α	1.00E-04	1000	3.42752	0.154576
	β (V^{-1})	14	14	14	14

Table 4.4: Parameters extracted from a respiratory neuron (RN → SSN) and from a CA1 pyramidal neuron (CA1 → SSN).

sodium (NaP), delayed-rectifier potassium (K), A-type potassium (A), in addition to a leakage channel [156, 205]. These ion channels were chosen in accordance with Table 4.3. The results of assimilating membrane voltage data with this RN SSN model are presented in Fig. 4.5, where the best fit of the model (green line) to the experimental membrane voltage data (black line) produced the parameter set listed in Table 4.4 in the "RN → SSN" column. The RN SSN model was completed with this parameter set and predictions of the membrane voltage for $t \geq T$ were generated in response to the current protocol (blue line). The predictions show a high degree of accuracy (Fig. 4.5(a)) comparable to that of the CA1 SSN predictions, with a spike coincidence factor of 76% and an $R^2 = 92\%$ match between the predicted and observed times series voltages. A more detailed comparison of data and prediction is given in Fig. 4.5(b) which presents an expanded segment of the prediction window. The sub-threshold membrane voltage dynamics for the RN predictions are much better than for the CA1 SSN model, even though deep hyperpolarizing step currents are still the greatest source of prediction error. This could be due to the fact that few hyperpolarizing currents are used in the assimilation window (Fig. 4.5(a)). The accuracy of predictions to an ensemble of 60 different current stimuli further demonstrated the successful transfer of information from the respiratory neuron to the RN SSN model [81]. The dynamics of the gating variables at the site of a single action potential are shown in Fig. 4.5(c). As in the HH and CA1 examples above, the spike initiates as a result of the activation of the NaT channel before the slower-activating potassium currents activate, contributing to repolarization. We therefore find that the RN SSN model accurately represents the membrane voltage dynamics of the respiratory neuron and the relative activation sequence of its component ion channels.

4.4 Discussion

The results in this chapter demonstrate an effective methodology for building artificial solid-state neurons that may be used to repair diseased biocircuits in the central nervous system. There is a clinical need for biomedical devices incorporating biofeedback that permits natural control in real-time. For example, the respiratory

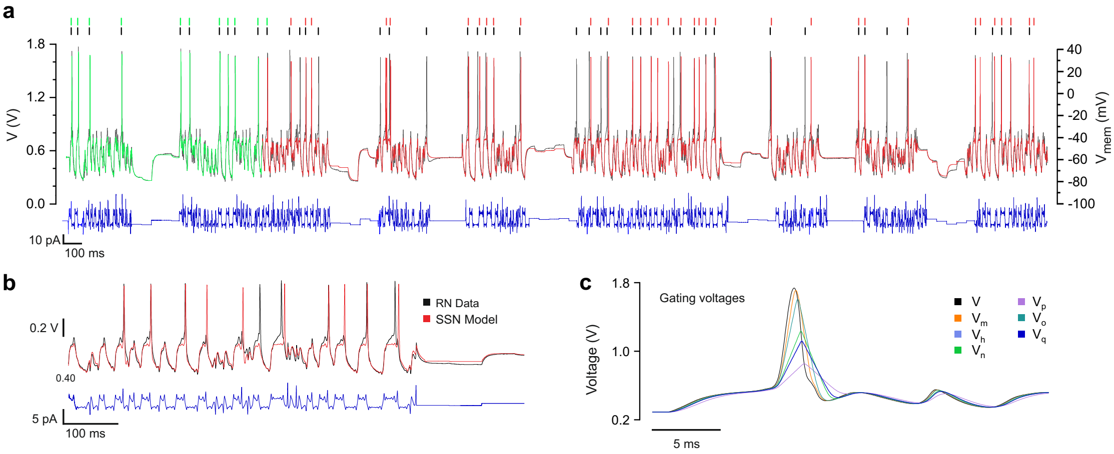

Figure 4.5: Assimilation and prediction of a respiratory neuron. (a) Intracellular recording of a respiratory neuron acquired from a slice of the Bötzinger region of the rat brain stem (black line). The neuron was stimulated with a current waveform alternating hyperchaotic oscillations and current steps (blue line). The RN SSN model was used to assimilate the experimental membrane voltage over a 1000-ms-long window (green trace) to estimate the optimum parameters. (a,b) The completed RN SSN model predicts the membrane voltage (red traces) in quantitative agreement with observations (black traces) for a very wide range of current waveforms. (c) Detail of the gating variables during an action potential.

neuron modelled in this chapter belongs to a network which couples the cardiac and respiratory rhythms, and is responsible for respiratory sinus arrythmia (RSA). The loss of RSA due to old age or disease is a strong indicator of cardiovascular pathology. Solid-state devices embodying synthetic medullary circuits may offer a much needed therapy for heart failure [53, 54, 206]. The presented method answers this need by providing an accurate neuromorphic implementation of ion channel dynamics that can be configured to respond in a quantitatively similar manner to any given neuron. This approach combines a number of advances. Firstly, the data assimilation approach used to estimate the parameters of the solid state neuron requires little-to-no prior knowledge of ion channel kinetics or maximal conductances; all parameters are estimated in an automated manner, eliminating the need for subjective fitting criteria. A second advance stems from the fact that data assimilation configures the entire model simultaneously from a single time series recording of the membrane voltage. In contrast, previous methods have fitted models using the sequential fitting of voltage-clamp measurements obtained from individual families of ion channels [207]. These measurements require pharmacological manipulation and data must necessarily be pooled from multiple neurons. As highly nonlinear systems, neurons configured with parameter averages often do not behave as the 'average' of the pooled neurons themselves [72]. Data assimilation of membrane voltage data avoids these challenges entirely. Furthermore, the assimilation of large datasets allows the fitting method to absorb stochastic fluctuations of spike timings if the assimilation window is sufficiently large. This minimizes uncertainty on extracted parameters. The third advance made by this work is the derivation of a mathematical description of the hardware SSN device, allowing the use of parameter estimation methods typically reserved for use with numerical models. Previous approaches used the numerical Hodgkin-Huxley model as a proxy of the hardware dynamics in the hope that parameters estimated with the Hodgkin-Huxley model would give correct predictions when programmed in the hardware [208]. For predictions to be successful, the same system of equations must be used when both assimilating data and forward integrating completed models. In this way, it is possible to also predict the time dependence of gate variables (Figs. 4.4, 4.5).

The SSN model presented here is highly versatile, allowing the inclusion of a variety of ion channels types, biologically-plausible slopes of activation functions and gate kinetics. These allow the model to describe both the electrical activity and internal dynamics of complex mammalian neurons. The hardware models typically used in the neuromorphic engineering literature are simplified or phenomenological models such as the integrate-and-fire neuron [176, 209], which are inadequate for generating quantitatively accurate predictions. Our development of a hyper-realistic neuron model allows for the faithfully transfer of neuronal dynamics from a biological cell to the SSN device. As a potential bioimplantable device, it is important that the SSN consumes very little power. The SSN respiratory neuron was found to have an average power consumption of 139 nW when firing at a rate of 240 Hz, dissipating 579 pJ per spike [81]. This power consumption is approximately 110 times smaller than the equivalent digital SSN implementation, making the analog VLSI SSN highly suitable for biomedical applications.

The current-clamp experiments performed in this chapter injected a complex current protocol in the neuron soma, while recording the response of the somatic membrane voltage. This experimental design allowed us to consider the neuron as a single isopotential compartment. From a computational standpoint, a single compartment model has the benefit of keeping the number of free parameters to the minimum number required to accurately predict neuron electrical activity. In biological neurons, however, other aspects of the neuron physiology play important roles. For example, dendrites are the predominant locus for afferent synaptic signals. Ligand-gated channels in the dendrites elicit dendritic spikes upon receipt of synaptic input which forward-propagate to the soma [210]. Furthermore, action potentials that initiate in the soma will often backpropagate towards distal dendrites [211, 212]. While the question of the function of backpropagation remains unresolved, it has been suggested that it may contribute to synaptic plasticity [213]. Further SSN compartments could be added to describe the active properties of dendrites, and these multi-compartment models could be similarly optimized to accurately predict these phenomena.

In the next chapter, we show that hardware implementations of optimized neurons can be extremely useful for the modelling of neural networks of interest. Solid-state neurons offer a route by which neuronal systems can be emulated directly and in real-time, and are therefore much more suited than simulations to the high-resolution parameter sweeps that are often necessary for analysing nonlinear and chaotic dynamics. Traditionally, solid-state neuron circuits have provided only a qualitative approximation to the exact equations governing simulated neurons, and as such are rarely used for quantitative neuroscientific research [42]. The novel biomimetic ion channel presented in this chapter allows for the building of highly predictive hardware neurons whose parameters can be obtained using the methodology that we have described.

Part II

Dynamics of Neural Circuits

Chapter 5

Synchronization in inhibitory neural networks

5.1 Introduction

Synchronized firing activity has been observed in many central nervous systems, but its underpinning mechanisms and neurobiological function remain a topic of debate [55, 56]. Synchrony has been observed in various neuronal populations, including thalamocortical relay neurons [63], hippocampal pyramidal neurons [64], and cortical inhibitory interneurons [65]. In these studies, the main mechanisms proposed for this coherence were excitatory synaptic coupling or electrical coupling mediated by gap junctions [66]. Indeed, inhibitory synaptic connectivity has classically been considered as a mechanism promoting antisynchronous firing [67, 68]. Recent findings are now challenging this view. In the cerebral cortex and hippocampus, there exist two prevalent sub-types of synchronizing interneurons [214]: soma-targeting fast-spiking (FS) cells [215, 216], and somatostatin-containing interneurons (SOM) that preferentially target dendrites [216, 217]. Neighboring SOM–SOM and FS–FS pairs are often coupled through both gap junctions [218] and GABAergic inhibitory synapses [219]. In the literature, the importance of the electrical coupling for synchronous network activity has been emphasized [66, 220, 221]. However, recent work has described synchrony in networks of FS and SOM interneurons with purely inhibitory coupling [69, 70]. These studies have found that tonically depolarized FS–FS and SOM–SOM pairs connected by bidirectional inhibitory synapses often fired coherently [70], thus experimentally confirming the existence of inhibition-driven synchrony that has been previously predicted theoretically [76, 222]. While these experiments confirm that coordination of firing can arise by mutual synaptic inhibition alone, the mechanisms still remain unclear. An understanding of the properties of these networks, and their robustness to near-experimental conditions, is now needed, though it remains extremely difficult to reveal the dynamical mechanisms of intercircuit coordination by direct experimentation in vivo or in vitro.

Motivated by these challenges, we used small networks of inhibitory silicon neurons to show that local networks mimicking the soma-targeting properties observed in fast-spiking interneurons and the dendrite-projecting properties observed in somatostatin interneurons synchronize through two distinct mechanisms. The first mechanism corresponds to conduction delays deriving from dendritic-targeting of SOM synapses. We find that these delays act to boost the number of stable coherent oscillations in the network. The second mechanism we observe is a dependency on the amplitude of stimulation current applied to the circuit. We find that synchronous network oscillations are most stable within a particular band of amplitudes, a result which we identify with the high-frequency entrainment of FS neurons [223]. We probed the synchronization phase diagrams of all-to-all inhibitory networks in-silico as a function of inhibition delay, neurotransmitter kinetics, timings and intensity of stimulation. Delayed inhibition was found to stabilize synchronization over a broader range of experimental conditions than high-frequency entrainment.

Computational models have previously been used to test other synchronization mechanisms such as the interneuron gamma (ING) mechanism [224], the pyramidal interneuron gamma (PING) mechanism [225, 226], the action of both excitatory and inhibitory synapses [227, 228] and the modulation of long range inhibition by local dendritic gap junctions [229, 230]. Mutually inhibitory networks, however, are highly nonlinear systems that exhibit abrupt transitions between modes of oscillation in response to the timing and amplitudes of stimuli [76, 231, 232]. Neuromorphic silicon networks allow us to measure these phase transitions in real time without compromise on model accuracy, size or complexity [41, 233]. A further merit of using neuromorphic systems is to demonstrate the robustness of the large number of stable modes of oscillation which we observe against noise and network imperfections.

The chapter is organised as follows. First, the methods section describes the implementation of the silicon neurons and the two types of coupling in the network: chemical synapses and gap junctions. Next, it describes a method for transforming multi-neuron spike trains into a set of evolving phase lags between neuron pairs. This framing allows us to reduce the problem of analysing rhythmic firing patterns to the analysis of fixed points in a phase-lag state space. Results are first presented for a pair of mutually inhibitory interneurons, before being extended to larger three- four- and five-cell networks. We then introduce a novel combinatorial counting method for calculating *a priori* the number of coherent oscillatory modes available to an N-neuron all-to-all inhibitory network. The chapter ends with a discussion of the presented results.

5.2 Methods

5.2.1 Silicon all-to-all inhibitory network

The silicon neurons used in this chapter implemented the Mahowald-Douglas (MD) SSN model [41]. In this model, the action potential is generated by a fast-activating transient sodium current (NaT), and repolarization is driven by a delayed-rectifier potassium current (K) in addition to a leakage current (Leak). Therefore, the MD model is essentially a translation of the Hodgkin-Huxley model (Sec. 2.2) to very-large-scale integrated (VLSI) circuit technology. Six of these neurons were interconnected (Fig. 5.1) with mutually inhibitory VLSI synapses [234] that injected either a positive or negative postsynaptic current into the receiving neuron, depending on the user-defined configuration. Individual neurons could be added and removed from the functioning network as desired. The silicon neurons emulated the dynamics of the membrane voltage V in response to an external current stimulus I_{stim} which evolved according to the equation: $C\dot{V} = g_{\mathrm{Na}}(E_{\mathrm{Na}} - V) + g_{\mathrm{K}}(E_{\mathrm{K}} - V) + g_{\mathrm{Leak}}(E_{\mathrm{Leak}} - V) + I_{\mathrm{stim}}$ where E_{Na} and E_K are the sodium and potassium reversal potentials and C is the membrane capaci-

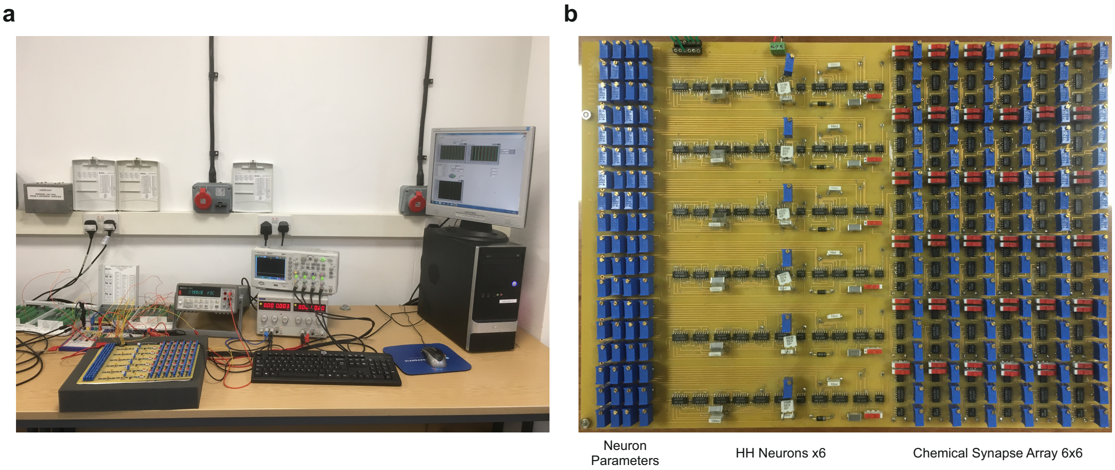

Figure 5.1: (a) Data acquisition bench used to acquire the dynamics of analogue inhibitory networks. DAQ cards (NI6259×2, top left) inject timed currents stimuli into individual neurons and record the time series data of their membrane voltage. The application of stimuli was controlled using a custom-built LabVIEW program. (b) All-to-all mutually inhibitory network of six silicon neurons connected via 36 synapses. Time dependent current stimuli are injected in the top left DIL port. The same port is used to measure the time series membrane voltages. The number of neurons in the network was increased or decreased by setting synaptic conductances to zero.

tance. In the MD model, the gating variables m, h and n of the Hodgkin-Huxley model are represented in the analogue circuit by currents ι which are either activated or inactivated according to: $\iota(V_{\tau,x}) = \iota_{\text{max}}\{1 + \tanh[(V_{\tau,x} - V_x)/dV_x]\}/2$, where $x = \{m, h, n\}$, V_x is the threshold voltage of each ion gate, and dV_x is the determines the slope of the (in)activation function of the gate. The $V_{\tau,x}$ variables follow a first order dynamics $\dot{V}_{\tau,x} = (V - V_{\tau,x})/\tau_x$ which describes the recovery of each gate variable and is characterized by recovery time τ_x [233].

Two different types of synapse were implemented in the silicon circuit: 'chemical' synapses [234] that model the injection of postsynaptic current in response to a presynaptic spike, and gap junctions, which directly couple the membrane voltages of the presynaptic and postsynaptic neurons. The chemical synapses were implemented using a differential pair integrator circuit (Fig. 5.2(a)). The postsynaptic current was approximately given by $I_{\text{post}}(t) = gS(t)(V_{\text{post}}(t) - V_{\text{rev}})$ where $V_{\text{rev}} = 7\text{V}$ was the reversal potential, $V_{\text{post}}(t)$ the membrane voltage of the postsynaptic neuron, g the maximum conductance and $S(t)$ was the fraction of docked neurotransmitters at time t. The neurotransmitter docking rate was given by: $\dot{S}(t) = [S_\infty(V_{pre}(t)) - S(t)]/\tau_u$ with $S_\infty(t) = 0.5\{1 + \tanh[(V - V_{th})/dV_{syn}]\}$. The empirical inhibition delay d, decay time τ_u and synaptic conductance g were controlled through the tuning of three gate voltage parameters: V_{th}, V_W and V_τ in the circuit. The synaptic conductance could take values in the range $1\ \mu\text{S} < g < 3\ \mu\text{S}$. The gap junctions were implemented electronically using a differential transconductance amplifier circuit. The current-voltage transfer characteristics of these VLSI gap junctions have previously been measured by Zhao and Nogaret [233]. The current varies linearly as $I_{\text{post}} = g'(V_{\text{post}}(t) - V_{\text{pre}}(t))$ near the balance point of the pre-synaptic and post synaptic membrane potentials. The transconductance g' can be tuned in the range $24\ \mu\text{S} < g' < 45\ \mu\text{S}$ using the gate bias V_M of a current source transistor. Away from the balance point, saturation effects reduce the rate of current injection [233]. The polarity of the injected current could be changed by swapping the voltage inputs. In this way one could form either an inhibitory or an excitatory connection between neurons in the circuit. The minimum stimulation current needed to elicit firing in an individual neuron is referred to as the 'depolarization threshold', I_{th}, and was adjusted to match the range of synaptic currents by adjusting the leakage current of the neuron membrane. For the chemical synapses, the current thresholds were $I_{\text{th}} = 8\ \mu\text{A}$ (synaptic coupling) and for gap junctions, $I_{th} = 86\ \mu\text{A}$. The duration of an action potential was tuned to $W = 1$ ms.

5.2.2 Generating phase-lag trajectories

Individual neurons were stimulated by current steps of constant amplitude I_{stim} generated by the analogue outputs of two DAQ cards (NI PCI6259) and a bank of six voltage-to-current converters. Custom LabVIEW [235] code was written to vary the timings of current stimuli in a systematic manner. Throughout this chapter, we reduce the problem of analysing rhythmic firing patterns to the analysis of phase lags between neuron pairs. By staggering the onset of stimulation for individual neurons, we were able to initialise the network in a range of desired phase-lag states (Fig. 5.3). During an initial transient phase (Fig. 5.3(b), blue), the phase relationships between the neurons adjust over consecutive cycle periods

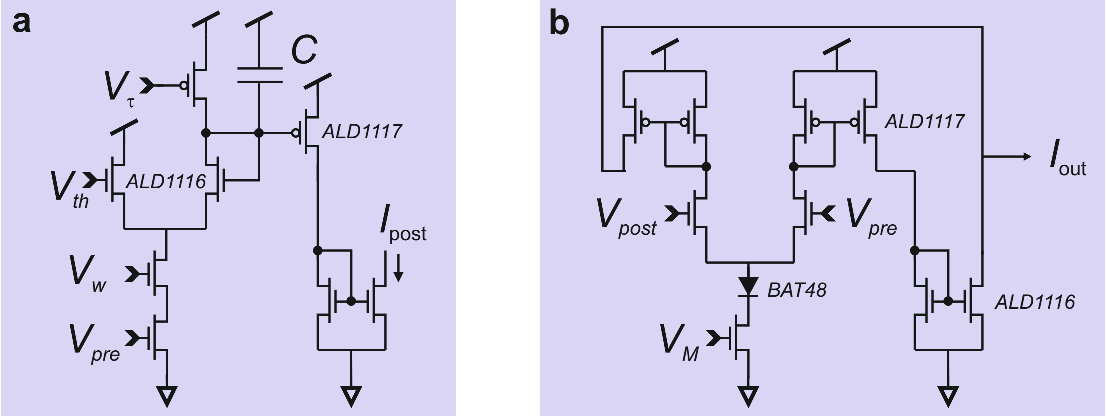

Figure 5.2: VLSI synapses. (a) Inhibitory chemical synapse [234]. Presynaptic action potentials, V_{pre}, increase the conductance of the presynaptic MOSFET. The drain current of this MOSFET is modulated by V_W which sets the synaptic weight. The V_{th} MOSFET sets the activation threshold of the synapse. The docking time (τ_d) and undocking time (τ) of neurotransmitters are modelled by the charge discharge times of capacitor C through the V_τ MOSFET. τ_u and τ_d were tuned with V_τ. The delayed synaptic response d was tuned with parameters V_{th} and V_W. (b) Inhibitory gap junction [233]. The output current of this synapse was is a linear function of the difference between the pre- and post-synaptic membrane voltages V_{pre} and V_{post}, respectively.

of length T. After a period of time, the network phase lags cease to change over consecutive periods, and the network reaches a steady state (Fig. 5.3(b), right). The state of the network in cycle period p is defined as the set of phase lags $\{\Delta\Phi_{i1}^{(p)}\}$, $i = 2, 3, \ldots N$, where $\Delta\Phi_{i1} = (t_i - t_1)/T$ denotes the phase-lag of neuron i relative to neuron 1. Prior to each run, the network was prepared in a particular initial state, and the temporal evolution of these phase lags $\{\Delta\Phi_{i1}^{(p)}\}$ was measured over consecutive network cycles $p = 1 - 50$, to obtain phase-lag trajectories. By varying the initial delays between the neurons with respect to the reference cell 1, we can detect all stable oscillatory modes of the network.

For a network of size N, the phase shifts $(\Delta\Phi_{21}^{(p)}, \Delta\Phi_{31}^{(p)}, \ldots \Delta\Phi_{N1}^{(p)})$ were calculated in each oscillation period $p = 1 - 50$ using a MATLAB [236] programme which extracted the timings of voltage peaks of neuron i and neuron 1 in each oscillation period. The state trajectories $\mathbf{\Delta\Phi}^{(p)}$ were plotted in an (N-1)-dimensional ($\Delta\Phi$) coordinate system. For the visualisation of higher-dimensional state spaces, the trajectories were plotted orthographically in the Coxeter plane of the $(N-1)$-

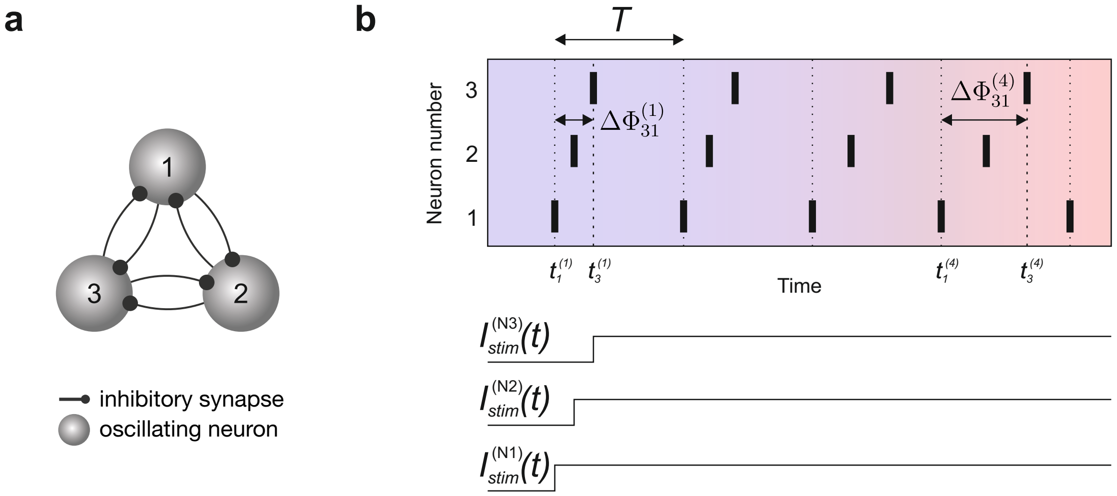

Figure 5.3: (a) Schematic of 3-neuron inhibitory network. (b) Stimulating current steps I_{stim} applied to individual neurons are staggered relative to the onset of stimulation for neuron 1. The neurons begin firing (vertical black bars) with period T upon injection of their respective I_{stim}. In each network period, the state of the network is defined by the phase lag pair $\boldsymbol{\Delta\Phi} = (\Delta\Phi_{21}, \Delta\Phi_{31})$, where $\Delta\Phi_{i1} = (t_i - t_1)/T$ is the phase lag of neuron i relative to neuron 1. By systematically varying the timing of current stimulation, the network can be initialized at a different $\boldsymbol{\Delta\Phi}$, and the evolution of the phase lags over consecutive periods can be observed.

dimensional hypercube ($N = 4, 5$) using projection matrices:

$$\hat{\mathbf{P}}_{4N} = \begin{pmatrix} -\sqrt{2}\cos\theta_4 & \sqrt{2}\sin\theta_4 & 1 \\ \sqrt{2}\sin\theta_4 & -\sqrt{2}\cos\theta_4 & 1 \end{pmatrix}, \tag{5.1}$$

where $\theta_4 = \pi/12$, and

$$\hat{\mathbf{P}}_{5N} = \begin{pmatrix} 1 & \cos\theta_5 & 0 & -\cos\theta_5 \\ 0 & \sin\theta_5 & 1 & \sin\theta_5 \end{pmatrix}, \tag{5.2}$$

where $\theta_5 = \pi/4$. The state trajectories pertaining to the same stable mode were regrouped using MATLAB code that calculated the $\Delta\Phi$-coordinate of the mode.

5.3 Results

5.3.1 Dynamics of the half-center oscillator

The half-center oscillator (HCO) is a fundamental building block of many central pattern generator (CPG) circuits, the rhythmic networks that drive patterned behaviours in biological systems [237, 238]. The HCO is a widely-used model for the reciprocal inhibition of clusters of neurons that produce anti-phase spiking or bursting patterns that are typically phase-locked with one-another [239]. The dynamics available to the HCO have been studied from both biological and nonlinear dynamics standpoints, however understanding the transitions between possible HCO dynamics as a function of network parameters often requires brute-force parameter sweeps of computational models [240, 241]. For these reasons, the HCO is an ideal system for initiating a study of the emergence of synchronization through inhibition using a real-time hardware CPG. Here, we examine the onset of synchronization in a mutually inhibitory neuron pair (Fig. 5.4) as a function of synaptic kinetics (d, τ_u) and current stimulation (I_{stim}) applied to all of the neurons in the network, generating an $d - I_{\text{stim}}$ phase diagram for the emergence of phasic synchronous modes of oscillation.

We began by setting the inhibition delay to the minimum configurable value of $d < 150$ μs). As I_{stim} is increased from the depolarization threshold cur-

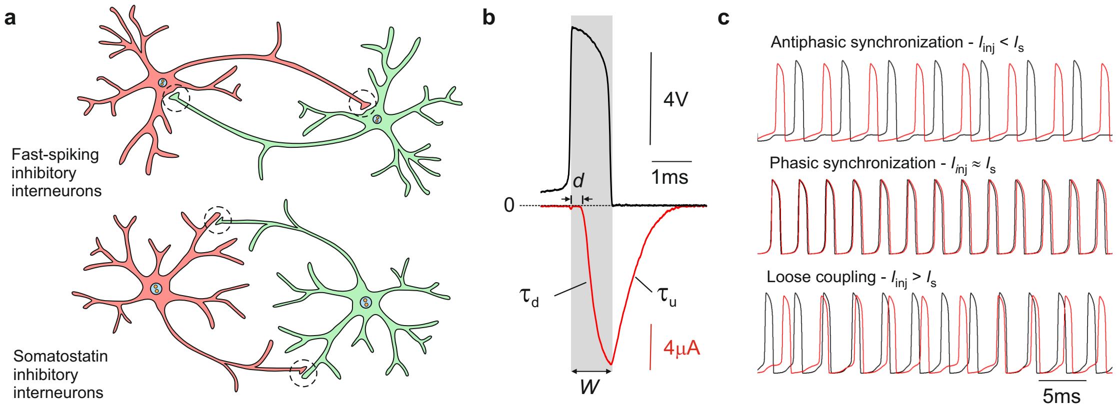

Figure 5.4: Synchronization of a pair of mutually inhibitory neurons. (a) Fast-spiking soma-projecting (FS) and somatostatin dendrite-projecting (SOM) interneurons. Synapses located on dendrites act to delay the inhibition of the postsynaptic neuron by $0 - 800$ μs. (b) Inhibitory postsynaptic current (red line) elicited by an action potential in the presynaptic neuron (black line) applied to a VLSI synapse. Synaptic kinetics: inhibition delay d, neurotransmitter docking time τ_d, undocking time τ_u, and spike width W. (c) Periodic action potentials of mutually inhibitory neurons below, at, and above the synchronization current, I_s. $\tau_u = 1.5$ ms.

rent ($I_{th} = 8$ μA), three distinct modes of synchronized oscillations are observed (Fig. 5.4(c)). The first mode is antiphasic synchronization. In this mode, the two neurons are phase-locked, but oscillate out-of-phase. At a higher value of $I_{stim} = 14$ μA, the network suddenly switches modes and displays phasic synchronization where the two neurons lock in phase, firing simultaneously. We term the value of I_{stim} at which this occurs the *synchronization current* I_s. For $I_{stim} > I_s$, the synaptic inhibition becomes small relative to the stimulation current that each neuron receives, and as such the neurons gradually begin to decouple. As the stimulation increases, this loose coupling regime is characterized by $N : 1$ harmonic phase locking [242]. In this regime, the two oscillators undergo an integer number (N) of oscillation cycles before firing in synchrony again. Harmonic locking is found in many biological systems, including during coupling between cardiovascular rhythms, breathing, and blood pressure [243, 244].

We found that below a critical value of d, changing the synaptic inhibition delay had no effect on the synchronization current $I_\mathrm{S} = 14$ μA. For longer values of $d > 150$ μs, I_s broadens to become a window of width [I_L, I_H] (Fig. 5.5(a)). The window

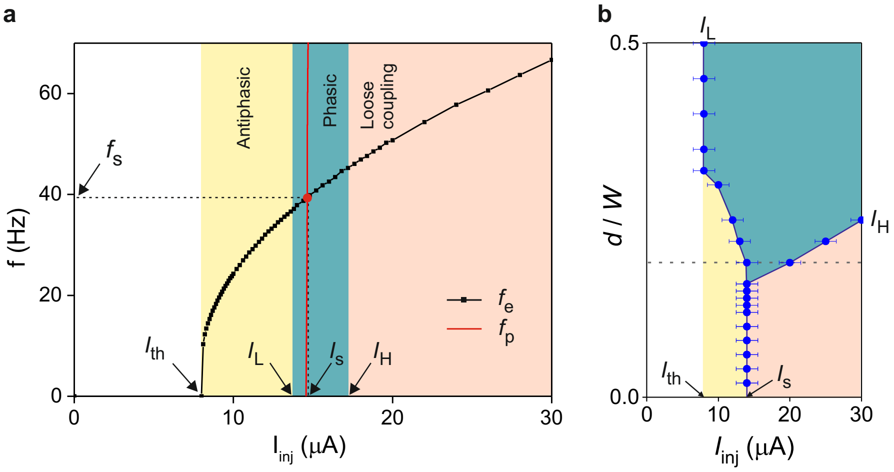

Figure 5.5: Dependence of the half-center oscillator pair on synaptic kinetics and stimulation. (a) Frequency-current dependence of a VLSI neuron (square symbols) and frequency-current dependence of phase-locked oscillations (red line). Their intercept gives the frequency (f_s) and current (I_s) of synchronized oscillations. Three domains of oscillatory modes at $d = 0.2W$ are observed (yellow, green, and red vertical bands). (b) Phase diagram of synchronization in the $d - I_{stim}$ plane where delay d is normalised by the spike width W. Two distinct mechanisms underlie synchronization in local inhibitory networks: changes in current stimulation amplitude and an increase in inhibition delay.

widens as a function of d, and the lower bound saturates at the depolarization threshold $I_{\mathrm{L}} = I_{th} = 8\ \mu\mathrm{A}$ for $d > 300\ \mu\mathrm{S}$. Above this value of d, the window continues to diverge with increasing in I_{H}, further stabilising the synchronous oscillatory mode. These results are in agreement with recent experimental work by Wang et al. who probed the synchronization of biological neuronal networks in the entorhinal cortex [245]. They found that while inhibitory coupling led to anti-phase oscillations in the case of no delays, it led to near-synchrony for delays of $> 10\%$ of the network period. In summary, the upper and lower bounds of the I_{s} interval $[I_{\mathrm{L}}, I_{\mathrm{H}}]$ carve out three domains in the $d - I_{stim}$ phase diagram of Fig. 5.5(b), corresponding to antiphasic (yellow), phasic (green), and loose coupling (red) regimes. This phase diagram demonstrates how phasic synchronization in the HCO may be induced either by delaying the onset of synaptic inhibition, or alternatively by applying an appropriate stimulation current sufficiently close to the synchronization value I_s. The effect of delayed synaptic inhibition is to allow each neuron in the pair sufficient time to depolarize prior to being inhibited by the other. We now extend these results by probing the network dynamics of a 3-cell inhibitory CPG network.

5.3.2 3-cell mutually inhibitory network

Studies of 3-cell CPGs in the context of biology have consistently discovered highly nonlinear and multistable dynamics [246–249]. These dynamics are known to make the oscillatory modes of the system highly sensitive to incoming stimuli generated by 'command neurons' designed to switch between specific motor pattern of the CPG [250–252]. By configuring a 3-cell CPG network of silicon neurons, we now extend the results of the previous section to analyse this dependence on the timing of external stimuli. The state of the network in a given cycle period was defined by the set of phase lags $\Delta\boldsymbol{\Phi}$, where $\Delta\Phi_{i1}$ denotes the lag of neuron i relative to neuron 1, $i = 2, 3, \ldots N$ as described in Sec. 5.2. By preparing the network in a particular initial state, and measuring the temporal evolution of these phase lags $\{\Delta\Phi_{i1}^{(p)}\}$ over consecutive network cycles $p = 1-50$, state trajectories of the system were obtained. Fig. 5.6(a) shows the phase-lag map of these trajectories for a mutually inhibitory 3-neuron network with $d = 300\ \mu$s inhibition delay. Each state trajectory emanates from a distinct initial phase-lag $\Delta\Phi_{i1}^{(1)}$, and converges to one of six attracting points in the phase space, labelled with circular, square and diamond symbols. The symbol type corresponds to the sub-division of the attractors into three categories according to the duration of their inter-spike intervals (ISI): $T/3$, $T/2$, and T, where T is the period of the network cycle (Fig. 5.6). Two of the six attractors (circle symbols) correspond to modes of oscillation in which the three neurons fire in clockwise and anti-clockwise sequences $1 \rightarrow 2 \rightarrow 3$ and $1 \rightarrow 3 \rightarrow 2$. The ISI for these attractors is $T/3$, since the cycle period is shared between the three neuron spikes (Fig. 5.6(b), top). Three of the six attractors (square symbols) correspond to partially-synchronized modes of oscillation in which two of the three neurons fire in-phase (Fig. 5.6(b), middle). These correspond to the sequences $1 \rightarrow \{2, 3\}$ and its permutations, where $\{i, j\}$ denotes the synchronized firing of neurons i and j. For these modes, ISI $= T/2$. The final attractor (diamond symbol) corresponds to the fully-synchronized mode of oscillation in which all three neurons fire in-phase with ISI$=T$. (Fig. 5.6(b), bottom). The phase lag map in Fig. 5.6(a) shows that the corresponding basins of attraction of the modes become smaller as the oscillations become more coherent. While the basins of attraction for the anti-phase modes (black and red) span most of the phase space, the basin for the fully-coherent mode (yellow) attracts only a few trajectories. The structure of the phase space is therefore consistent with observations of HCO which suggest that synchronized oscillatory modes are stable over a smaller range of network conditions, and are correspondingly more sensitive to external perturbation.

In the case of the HCO, we found the synchronous mode of oscillation to be highly-dependent on inhibition delay and I_{stim}. We wished to confirm whether these findings could be generalized to larger networks. First, we tested for delay-dependence in the the 3-cell network by reducing d from 300 μs to $d = 0$ μs for all connections in the CPG. The phase lag map for this configuration is shown in Fig. 5.6(c). The partially- and fully-synchronized attractors are no longer present in the phase space, leaving only the attractors corresponding to anti-phase modes of oscillation. For completeness, the synapses were then reconfigured to behave as non-delayed excitatory synapses. The phase portrait in Fig. 5.6 shows that this networks hosts a single fully-synchronized attractor. This is in agreement with theoretical work suggesting that all-to-all excitatory coupling is conducive to

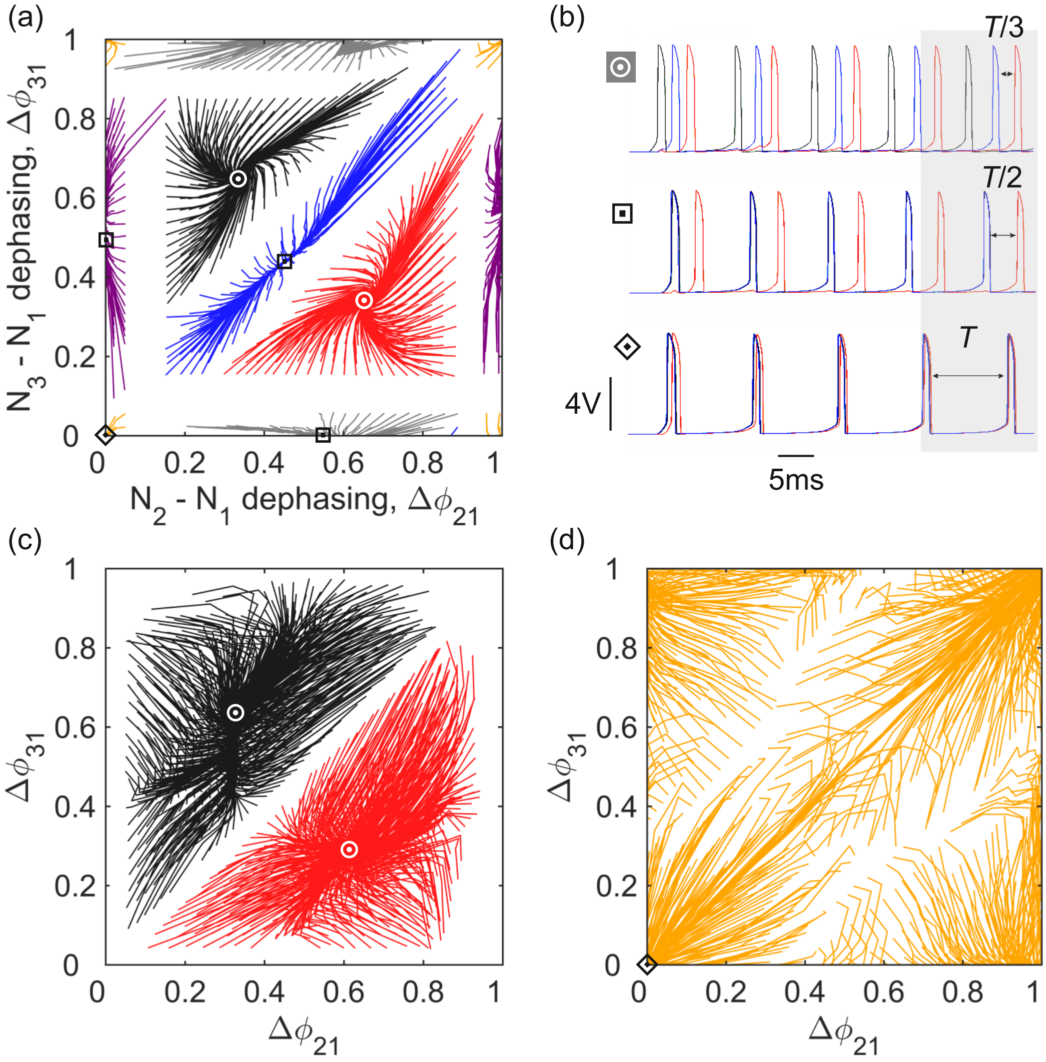

Figure 5.6: Phase lag portraits for 3-neuron inhibitory networks. (a) Experimental phase portrait of a three-cell network with neurons coupled via mutually inhibitory synapses. Anti-phasic travelling wave attractors (circle symbols), partially synchronized attractors (square symbols) and phasic, fully-synchronized attractor (diamond symbol) are the six observed stable oscillatory modes of the network. State trajectories (full lines) emanate from a grid of initial states $\mathbf{\Delta\Phi}$ evenly distributed over the phase space. Reciprocal inhibition across the network was homogeneous $g_{ij} = g_{ji} = 2$ μS for $i, j = 1, 2, 3$. (b) Transient neuron oscillations showing convergence towards (top) the antiphasic attractor (ISI=$T/3$), (middle) the partially synchronized attractor (ISI=$T/2$), and (bottom) the phasic attractor (ISI=T). (c) Phase portrait of a 3-cell network interconnected with mutually inhibitory gap junctions showing antiphasic attractors only (circle symbols) $g_{ij} = g_{ji} = 45$ μS. (d) Excitatory gap junction synapses result in a single attracting mode that corresponds to full synchronization (diamond symbol). Parameters: (a,b) $I_{stim} = 25$ μA, $T = 18$ ms, $g_{ij}^{(s)} = 2$ μS, $\tau_u = \tau_d = 1.5$ ms, $d = 300$ μs; (c,d) $I_{stim} = 50$ μA, $I_{th} = 86$ μA.

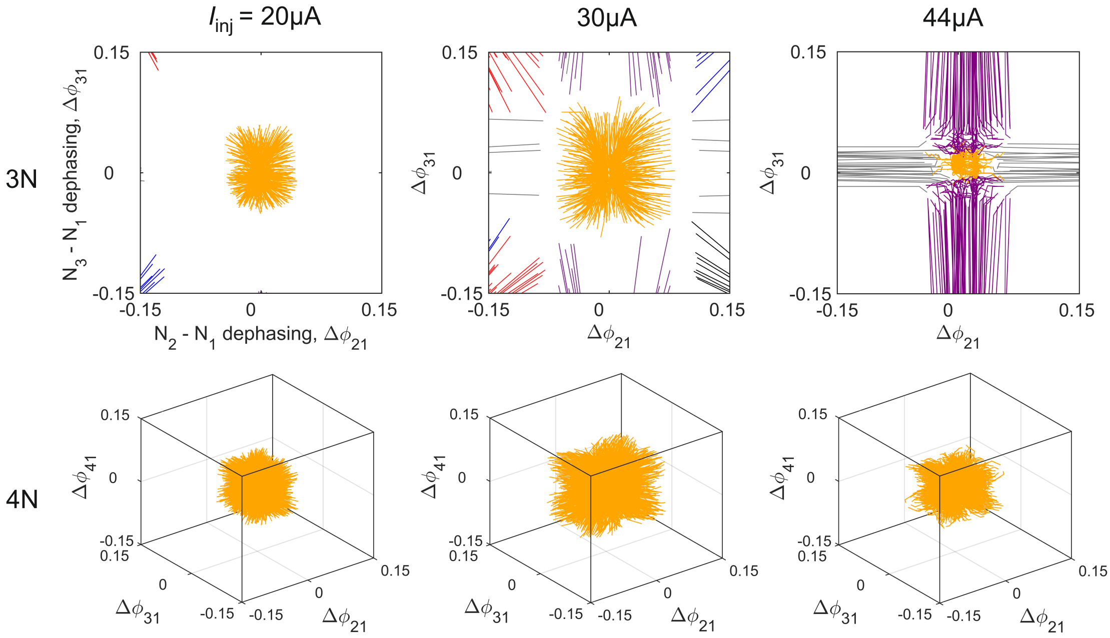

Figure 5.7: Current-dependence of the fully synchronized attractor. Phase-lag maps for the 3-neuron and 4-neuron inhibitory networks were measured in the vicinity of the coherent attractor (yellow basin) at increasing levels of current stimulation: $I_{stim} = 20$ μA, 30 μA and 44 μA. Grey, purple and blue trajectories correspond to nearby basins of partially synchronized oscillations, while red and black trajectories correspond to those of antiphasic oscillations. The volume of the coherent basin passes through a maximum at $I_s \approx 30$ μA. Parameters: $d = 350$ μA, $\tau_u = 1.5$ ms.

network synchrony [253]. Next, we examined the dependence of the synchronous mode on current stimulation. Fig. 5.7 (top) shows the phase portrait in the vicinity of the fully-synchronous attractor for the 3-cell network as I_{stim} was varied between 20 μA and 44 μA. The area of the coherent basin of attraction passes through a maximum at $I_s \approx 30$ μA. We also find that these findings hold for 4-cell inhibitory CPGs whose three-dimensional phase space in the vicinity of the coherent attractor is shown in Fig. 5.7 (bottom), demonstrating that synchrony is most stable close to values of $I_{stim} = I_s$. These observations generalize the $d - I_{stim}$ phase diagram for the HCO to larger networks, and show how synchronization in inhibitory networks can be achieved either through increases in inhibition delay or through carefully-tuned current stimulation.

In this section, we have considered oscillatory CPG modes that can be distinguished by the sequential firing of neurons in the network. In the following section, we demonstrate a combinatorial method for calculating the number of modes available to all-to-all inhibitory networks of arbitrary size. We then validate the method by generating phase-lag maps for three-cell, four-cell, and five-cell networks, and comparing our combinatorial calculations with the number of observed attractors in the phase space of each CPG.

5.3.3 Combinatorial counting of firing patterns

Information processing in the nervous system requires coordinated activity across populations of neurons, but the code by which populations of cells interact to perform computation is still largely unknown [254–256]. Recent advancements in neural engineering have enabled the simultaneous time series recording of large numbers of neurons, and there is now a corresponding need for new methods to analyze complex patterns across multiple simultaneous spike trains [257, 258]. Most current methods analyse firing patterns in terms of precise time delays between successive spikes [259–261]. Here, we describe a novel method for analyzing sequential firing patterns in networks of arbitrary size that is based on the relative firing order of the constituent neurons. Sequences are highly important for neural processing. Examples include sequential recruitment of different brain areas during a task, as well as spike sequences in models of pattern recognition [262]. Relative time order of firing events, in contrast to the precise time intervals between them, is important for a number of phenomena such as time-scaling and noise filtering [263–265]. Although we apply our method to individual spikes, the approach is general and could be applied to burst firing in a network cells, or even to EEG or ECG events.

We begin by recalling that in the networks analysed previously the N neurons discharge within a period that contains M inter-spike intervals (ISI) of duration T/M. These ISIs separate the N spikes into M discharge events. For example, in the fully synchronous mode there is a single discharge event ($M = 1$) in which all N neurons fire simultaneously. This event is said to have cardinality of $k_1 = N$. Here, the cardinality of each of the M discharge events refers to the number of simultaneous neuron firings in that event. In contrast, for a travelling-wave mode

$1 \to 2 \to ... \to N$ there are $M = N$ discharge events, each of which contains a single discharge, possessing cardinalities of $k_1 = k_2 = ... = k_M = 1$. In general, every oscillatory mode is characterised by $1 \leq M \leq N$ discharge events with cardinalities of $k_1 \geq k_2, ..., k_M \geq 0$, which satisfy the rule:

$$\sum_{i=1}^{M} k_i = N. \tag{5.3}$$

Let's take an example. In a four-neuron inhibitory network there exists a fully-synchronous attractor in which all four neurons fire in-phase, giving

$$\{k_i\} = (k_1, k_2, k_3, k_4) = (4, 0, 0, 0). \tag{5.4}$$

In this mode, there is a single ISI ($M = 1$). Other modes exists in which neurons fire over $M = 2$ ISIs, and they can be distributed as $(3, 1, 0, 0)$ or $(2, 2, 0, 0)$. Calculating the possible permutations of spike arrangements within these two attractor types gives us 4+3=7 distinct partially-coherent modes. For modes distributing over $M = 3$ ISIs, event cardinalities are $(2, 1, 1, 0)$, giving 12 partially coherent attractors of this kind. Finally, for the travelling-wave modes ($M = 4$) that distribute as $k_i = (1, 1, 1, 1)$, we have an additional 6 modes, giving a total of 26 attractors.

Now we generalise this calculation to find the capacity of inhibitory networks of arbitrary size. Recalling that the list $\{k_i\}$ denotes the occupancy of each discharge event, we now define a dual list $\{n_j\}$, $j = 1, ..., N$, that tabulates the *number of events* with each possible cardinality. An oscillatory period therefore can be said to contain n_1 single-spike events, n_2 two-spike events, ..., and n_N N-spike events. This dual list satisfies the sum rule:

$$\sum_{j=1}^{N} n_j = M. \tag{5.5}$$

Next, we note that spike groupings can be rearranged in a number of ways over the M inter-spike intervals which all realize the same dual list $\{n_j\} = (n_1, ...n_N)$. We call each of these rearranged spike groupings a different 'waveform' in which spike groupings appear in a particular sequence. The total number of attractors that a network may host is given by the number of possible waveforms multiplied by the number of possible rearrangements of spikes within a waveform. The number of possible waveforms that may be constructed from a given spectrum $\{n_j\}$ of spike groupings is given by:

$$\begin{aligned} W_N^M(n_1,...n_N) &= \binom{M}{n_1} \times \binom{M-n_1}{n_2} \times \binom{M-n_1-n_2}{n_3} \times ... \times \binom{M-n_1-...-n_{N-1}}{n_N} \\ &= \frac{M!}{M!(M-n_1)!} \times \frac{(M-n_1)!}{n_2!(M-n_1-n_2)!} \times ... \times \frac{(M-n_1-...-n_{N-1})!}{n_N!(M-n_1-n_2-...-n_N)!} \\ &= \frac{M!}{n_1!n_2!...n_N!(M-M)!} \\ &= \frac{M!}{n_1!n_2!...n_N!}. \end{aligned}$$

The number of waveforms is therefore given by the multinomial coefficient:

$$W_N^M(n_1,...n_N) = \binom{M}{n_1,...,n_N}. \tag{5.6}$$

We now consider the number of possible ways that individual firings can be arranged within any given waveform. For a given cardinality list $\{k_i\} = (k_1,...,k_M)$, there are $A_N^M(k_1,...k_M)$ ways of distributing N neuronal firings over the M ISIs. This is the number of ways of distributing k_1 spikes out of N in the first ISI, k_2 spikes out of $N-k_1$ in the second ISI, ..., and k_M spikes in the M^{th} ISI. It is calculated as follows:

$$\begin{aligned} A_N^M(k_1,...k_M) &= \binom{N}{k_1} \times \binom{N-k_1}{k_2} \times \binom{N-k_1-k_2}{k_3} \times ... \times \binom{N-k_1-...-k_{M-1}}{k_M} \\ &= \frac{N!}{k_1!(N-k_1)!} \times \frac{(N-k_1)!}{k_2!(N-k_1-k_2)!} \times ... \times \frac{(N-k_1-...-k_{M-1})!}{k_M!(N-k_1-k_2-...-k_M)!} \\ &= \frac{N!}{k_1!k_2!...k_M!(N-N)!} \\ &= \frac{N!}{k_1!k_2!...k_M!}. \end{aligned}$$

The number of possible arrangements of spikes within any given waveform is therefore given by the multinomial coefficient:

$$A_N^M(k_1,...k_N) = \binom{N}{k_1,...,k_M}. \tag{5.7}$$

The total number of attractors is obtained by multiplying the number of waveforms by the number of trajectories per waveform, and summing over the partition of integer N. This partition corresponds to the decreasing list $k_1 \geq k_2 \geq ... \geq k_m$ which satisfies the condition $k_1 + ... + k_m = N$. For example, the partition $(k \vdash N)$ of the integer $N = 5$ is shown in Table 5.1. The product $W_N^M \times A_N^M$ includes M cyclically invariant trajectories: firing as $1 \rightarrow 2 \rightarrow 3 \rightarrow 4$ or $4 \rightarrow 1 \rightarrow 2 \rightarrow 3$ correspond to the same attractor. The number of cyclically independent trajectories is thus obtained by dividing this product by M. We can now write the total capacity C of a given network as:

$$T_N = \sum_{k \vdash N} \frac{1}{M} \underbrace{\binom{M}{n_1, ..., n_N}}_{w_N^M = W_N^M / M} \underbrace{\binom{N}{k_1, ..., k_M}}_{A_N^M} . \tag{5.8}$$

Each element of the summation corresponds to a different partition $(k \vdash N)$ of the integer N, where M is the number of positive integers in each partition (see Table 5.2 for an example of this calculation). As we saw in the previous section, the capacity of a network is highly-dependent on synaptic inhibition delay. For small enough $d < 150$ μs, neurons in the network are only able to discharge sequentially, and the network is unable to host partially- or fully-synchronized oscillations. This implies that the number of discharge events is equal to the number of neurons $(M = N)$, and that $k_1 = k_2 = \cdots = k_N = 1$. This is a special case of Eq. 5.8, giving

$$L_N = \sum_{k \vdash N} \binom{N-1}{n_1, ..., n_N} \binom{N}{k_1, ..., k_M} = \frac{N!}{N} = (N-1)!. \tag{5.9}$$

This is well-known as the capacity of a class of dynamical systems called winnerless competition networks [231]. These networks dynamically encode stimuli in the form of deterministic trajectories corresponding to the sequential activity of neurons in the network. In this section, we have demonstrated that the inclusion of inhibition delay in all-to-all inhibitory networks can significantly boost network capacity.

k_1	k_2	k_3	k_4	k_5
1	1	1	1	1
2	1	1	1	0
2	2	1	0	0
3	1	1	0	0
3	2	0	0	0
4	1	0	0	0
5	0	0	0	0

Table 5.1: Integer partition for $N = 5$. The integer partition of n lists all ways of writing n as a sum of positive integers. Each row gives one of the seven partitions. Two sums that differ only in the order of their summands are considered the same partition.

5.3.4 Emergence of synchronization

Having derived the methodology for calculating the capacity of networks of arbitrary size, we now compare calculated values with experimental observations. Using Eq. 5.8, we calculate that the maximum capacity increases as $T_3 = 6$, $T_4 = 26$, $T_5 = 150$, $T_6 = 1082$. The minimum capacity, allowing sequential discharges only, is $L_N = (N-1)!$, and increases as $L_3 = 2$, $L_4 = 6$, $T_5 = 12$, $T_6 = 120$. These calculations are experimentally verified in Fig. 5.8, which shows that the capacity of an N-neuron all-to-all inhibitory network lies between L_N and T_N, depending on the synaptic inhibition delay d. For longer inhibition delays ($d = 400$ μs), partially- and fully-coherent oscillations are stable, and the networks host modes ranging from fully-synchronous (Fig. 5.8: (a) diamond, (b) triangle, (c) hexagon) to purely sequential (Fig. 5.8(a-c) circles). For example, the four-neuron phase-lag map in Fig. 5.8(b) hosts six sequential attractors (circle symbols) with one spike per inter-spike interval, giving discharge event occupancies (1,1,1,1), twelve partially-synchronous attractors (square symbols) with discharge event occupancies (2,1,1,0), 4 + 3 partially synchronized attractors (diamond symbols) with (3,1,0,0) and (2,2,0,0) occupancies, respectively, and the fully-coherent attractor (triangle symbol) with the occupancy (4,0,0,0). For clarity, the predicted capacity of the four-neuron network is calculated explicitly in Table 5.2. Fig. 5.8(d-f) shows that intermediate synaptic inhibition delay ($d = 250$ μs) destabilises the

M	ISI	k_1	k_2	k_3	k_4	n_1	n_2	n_3	n_4	$w_N^M\{n\}$	$A_N^M\{k\}$	$w_N^M \times A_N^M$
4	T/4	1	1	1	1	4	0	0	0	1/4	24	6
3	T/3	2	1	1	0	2	1	0	0	1	12	12
2	T/2	3	1	0	0	1	0	1	0	1	4	4
2	T/2	2	2	0	0	0	2	0	0	1/2	6	3
1	T/1	4	0	0	0	0	0	0	1	1	1	1
												Total = 26

Table 5.2: Calculation of the number of attractors for an all-to-all inhibitory network with 4 neurons using the combinatorial method. The third column displays all possible partitions of the integer $N = 4$. Each row in the table has a corresponding M, where M is the number of positive integers in the partition.

fully coherent mode in all sizes of network ($N = 3, 4, 5$). In the four-cell network, the partially-coherent attractors (ISI=$T/2$) have also vanished, while those with ISI=$T/3$ (square symbols) and ISI=$T/4$ (circle symbols) remain. Note that the basins of attraction of the remaining partially-coherent modes exhibit a reduced size (Fig. 5.8(d,f)). When synaptic inhibition delay is further reduced to $d = 100$ μs, only the sequential attractors remain (Fig. 5.8(g-i)).

Figure 5.9 shows how network capacity scales with the size of the network. For small inhibition delay, ($d = 100$ μs), the experimentally-observed capacities scale exactly as predicted from L_N (Eq. 5.9). At the longest inhibiton delays, ($d = 400$ μs), the maximum number of attractors is observed to increase according to the sequence T_N calculated by Eq. 5.8. At intermediate values of d, we observe that the networks host sequential oscillations in addition to a reduced number of partially-synchronised oscillations. The capacity of these networks therefore lies somewhere between L_N and T_N as expected. We can conclude from these observations that the capacity of all-to-all inhibitory networks can be boosted by a factor of T_N/L_N when synaptic inhibition is delayed.

5.4 Discussion

The results presented in this chapter suggest that inhibitory networks may synchronize via two distinct mechanisms that exploit the particular anatomical properties of fast-spiking interneurons and the inhibition delay introduced by dendrite pro-

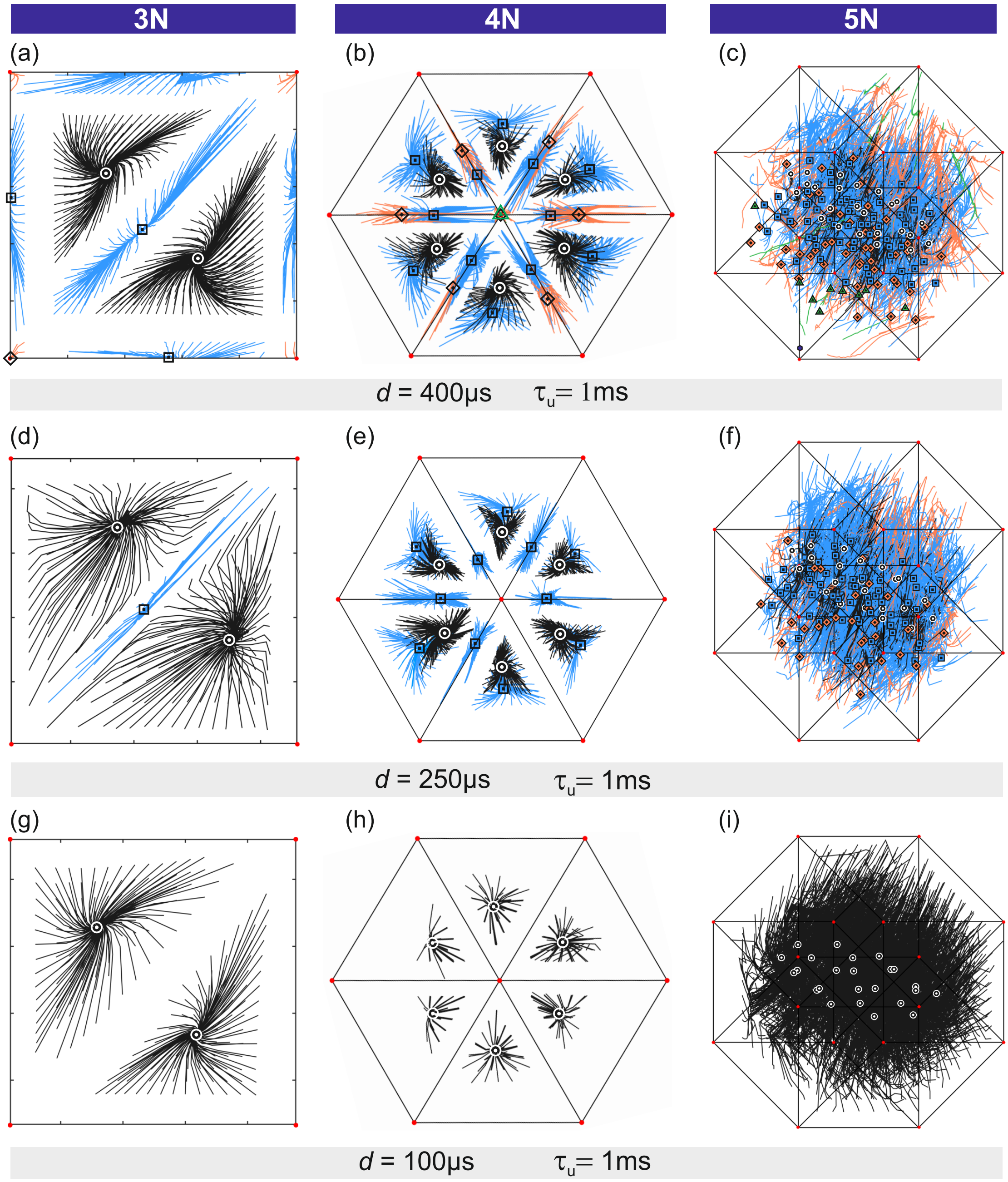

Figure 5.8: Emergence of synchronization in small inhibitory networks. Phase lag maps of the three, four and five-neuron networks measured at increasing values of inhibition delay (a–c) $d = 400$ μs, (d-f) $d = 250$ μs and (g-i) $d = 100$ μs. Both the decay time of the postsynaptic current: $\tau_u = 1.5$ ms and the inhibition peak current: -13.8 μA were kept constant. The (N-1)-dimensional phase space (straight lines) and the state trajectories within it (full lines) were projected orthographically into the Coxeter plane. State trajectories converge towards fixed-point attractors classified according to the duration of their ISIs: T/N (black lines, circle attractors), $T/(N-1)$ (blue lines, square attractors), $T/(N-2)$ (orange lines, diamond attractors), T/(N-3) (green lines, triangular attractors), $T/(N-4)$ (purple lines, hexagonal attractor). The total number of attractors observed at inhibitory delay $d = 400/250/100$ μs is 6/3/2 ($N = 3$), 26/17/6 ($N = 4$), 142/107/24 ($N = 5$), 1053/688/120 ($N = 6$).

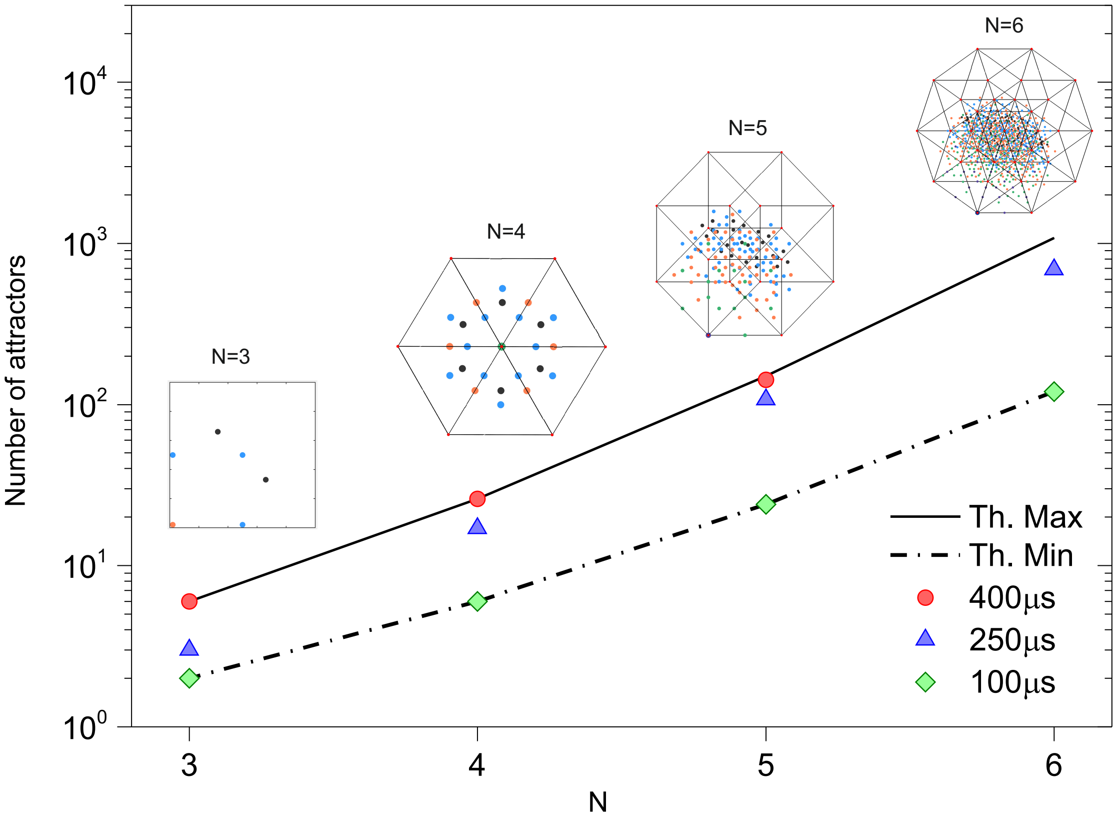

Figure 5.9: Scaling of network capacity with network size. The total number of attractors observed in the three-neuron to six-neuron networks at increasing values of the inhibition delay: $d = 100$ μs (green diamonds), 250 μs (blue triangles), 400 μs (red dots). At intermediate values of inhibition delay (250 μs), the network capacity lies between the upper theoretical boundary T_N (solid line) and the lower boundary L_N (dashed line). Inset are orthographic projections of predicted point attractors which are distinguished by the number of ISIs per cycle: ISI=T/N (black dots), $T/(N-1)$ (blue dots), $T/(N-2)$ (orange dots), $T/(N-3)$ (green dots), $T/(N-4)$ (purple dots).

jecting synapses in somatostatin cells. Dendrite-projecting somatostatin interneurons introduce conduction delays of the order of 0-800 μs by projecting synapses onto the 200-700 μm-long dendrites of the mammalian cortex [71]. Transmission line delays of this magnitude postpone the onset of inhibition sufficiently to stabilize the coherent oscillations of inhibitory neurons (Fig. 5.8(a-c)). The neurphysiological properties of somatostatin neurons could thus induce robust network synchronization which is only weakly dependent on shared excitatory stimulation and postsynaptic kinetics. In contrast to somatostatin neurons, the wiring of somatostatin neurons introduces delays which are too short to warrant automatic synchronization. Instead stomatostatin neurons may achieve synchronization through high-frequency entrainment. This corresponds to the current-induced synchronization which we observe at small inhibition delay.

The all-to-all networks used in this study are homogenous in all synaptic connections, and so the oscillatory modes display permutation symmetries. For example, within partially coherent states, the neurons which oscillate in phase may distribute differently across the network. A subset of L neurons ($L < N$) may oscillate in phase at different locations of the network. Two partially coherent states with identical L-number differ through the permutations of neuron firing order. The equivalence of these states is demonstrated by the six-fold symmetry of phase maps of the 4-neuron network (Fig. 5.8(b)). Changing synaptic conductances to introduce network heterogeneity has the effect of varying the sizes of basins of attraction of particular modes [76], breaking the phase space symmetry. This would correspond to the loss of partially coherent modes, and the reduction in total network capacity. Introducing a range of inhibition delays or mixing gap junctions with chemical synapses would similarly increase the volume of some basins to the detriment of others, potentially bringing total network capacity down below the theoretical minimum L_N.

Full synchronization in our network corresponds to the coherent attractor whose basin occupies a very small volume of phase space for all network sizes (triangle symbol, Fig. 5.8). As a result, this state of synchronization is the least robust of all possible modes with respect to noise and network heterogeneity. In contrast, the majority of the phase space volume is occupied by partially-coherent attractor basins of larger volume. Accordingly, these oscillatory modes are far more stable than the fully-coherent state (Fig. 5.8(a–c)), and therefore far more likely to support synchronized neural activity in real biological circuits. We showed that the introduction of delayed inhibition boosted the capacity of inhibitory networks by a factor of T_N/L_N. It was subsequently shown by Nogaret and King [266] that one can approximate this maximum capacity using the Stirling transform as $T_N \sim (N-1)!/(\ln 2)^N$. We can therefore say that the majority of the phase space is filled with partially coherent attractors whose proportion increases rapidly according to $(\ln 2)^{-N}$ as the network size increases, demonstrating network capacities far exceeding that of both winnerless competition networks ($\sim (N-1)!$) [231] and Hopfield networks ($\sim 0.14N$) [267].

In summary, this study leads us to conclude that local cortical and hippocampal microcircuits may have adapted to exploit the robustness of synchronization by delayed inhibition versus the tunability of synchronization by fast-spiking interneurons. We have demonstrated that mutual synaptic inhibition alone is sufficient for the emergence of synchronization, but only in the presence of adequate inhibition delay. These results are in agreement with experimental observations of synchronization in GABAergic interneuron networks [69, 70].

Although we report the results of experiments on spiking inhibitory networks, many of the same ideas may be extended to networks of bursting neurons. Indeed, many important functional circuits in the nervous system rely on the phasic and anti-phasic synchrony of bursting between network components [73]. Robust methods for the design of artificial networks with specific desired attractor modes in both numerical and hardware neuron models therefore have a wide range of potential applications. In the final results chapter, we demonstrate a novel optimization method for estimating the parameters of networks of bursting inhibitory neurons such that the network hosts the desired oscillatory modes. As a proof-of-principle, we apply the approach to the problem of designing a four-cell network generating the precise sequence of heart chamber contractions observed in mammalian ECG recordings.

Chapter 6

Designing functional inhibitory networks

6.1 Introduction

Central pattern generators (CPGs) are networks that generate rhythmic patterns in which the component neurons burst with fixed phasic relationships [73, 74]. Studies of living CPGs have demonstrated that these networks (i) are composed of fundamental building blocks based on mutual inhibition [268, 269]; (ii) are typically composed of neurons that undergo sequential activation, displaying what is known as winnerless competition dynamics [231]. More recently, hardware CPGs have been developed for various biomedical applications. An example in the field of neuroprosthetics is the demonstration by Sharma et al. of an artificial CPG emulating spinal cord CPG function that allowed the restoration of hand movement in a quadriplegic patient [270]. The participant was able to initiate, sustain, and switch between rhythmic and discrete finger movements of their own volition [271]. Another example comes from Nogaret et al., who recently used an analogue CPG device to reinstate respiratory sinus arrythmia (RSA) in rats, a natural form of coupling in which heart rate synchronizes to respiration [54, 206]. They drove RSA chronically in a conscious rat with induced heart failure, and found an improvement in cardiac function superior to that seen with monotonic cardiac pacing of traditional pacemaker devices [206].

In this context, there is a growing need for robust methods for designing artificial CPG networks that output desired phase-locked patterns. In a functional pattern-generating network, the phasic timing of the constituent neurons must be precisely tuned. The sequential bursting of neurons in these networks depends sensitively on the intrinsic dynamics of the component neurons themselves as well as on the strengths and time-dependent properties of the synapses which connect them [76]. This nonlinear dependence makes estimating all parameters of a network model a formidable problem [272]. In previous chapters, nonlinear optimization was used to estimate the parameters of single-neuron models (Chapters 3, 4), but such methods quickly become intractable when optimizing large networks of complex neurons [273, 274]. Recent work by Armstrong et al. attempted to estimate the parameters of a three-neuron network using nonlinear optimization, simultaneously fitting the full network model to membrane voltage time series traces of the three constituent neurons [272]. During twin experiments, it was observed that the cost function surface for this problem was riddled with local minima, a finding which highlights the challenging nature of high-dimensional nonlinear optimization [116].

In this chapter, we propose a solution to this challenge. We describe a novel optimization method that allows all neurons in a CPG network to be optimized individually by first reducing them to their individual phase resetting curves (PRCs) [78]. PRCs tabulate the extent to which a received synaptic input advances or delays the next firing (or bursting) time in an oscillating neuron as a function of where in the firing (bursting) cycle the input is received [79]. We show that the problem of designing a CPG with specific phase-lags between the neurons can be reduced to a problem concerning the properties of the individual neuron PRCs. Each oscillator in the network may then be optimized individually and sequentially such that each displays its required PRC. This method enables the estimation of all neuron and synapse parameters of the network while avoiding the challenges associated with searching the high-dimensional parameter space of a whole-network model. We apply our approach to the problem of estimating synaptic conductances for a four-cell CPG designed to match the sequence of heart chamber contractions in an ECG recording.

This chapter is organised as follows. The first section presents the background and methods required to arrive at the results, beginning with a description of the network model used throughout this chapter. We simulate the full dynamics available to the model CPG system, and present them using the same phase-lag mapping technique used in the previous chapter. In these simulated phase portraits, the phase-locked modes of the network correspond to fixed-point attractors. This is followed by a detailed overview of the concept of a phase resetting curve. In the next section, we justify our claim that the question of network phase-lags can be reduced to the properties of individual PRCs by showing that the PRCs alone contain all the information necessary to predict the full network dynamics. We do this by reproducing the simulated phase portraits with a model-free algorithm that takes in user-defined initial phase-lags and uses the network PRCs to predict firing times in subsequent cycles. We then turn to the main question of network design. We begin with an explanation of how the shape of the individual neuron PRCs determines the character of phase-locked network modes, and derive the set of criteria that neuron PRCs must fulfill for the network dynamics to be stable. We then describe the optimization-based method that we use to generate individual neurons with required PRCs, which we use in the final section to construct a four-cell CPG. Finally, we conclude with possible directions for future work.

6.2 Methods

6.2.1 Model system

In this chapter, we consider networks of identical neurons coupled by inhibitory chemical synapses. The neurons are described by an extended Morris-Lecar (ML) model that includes a Ca^{2+}-dependent K^{+} current that allows them to be parameterized in a bursting regime [275]. While the method we describe is applicable to both spiking and bursting CPGs, in this chapter we use bursting neurons, as this constitutes the more difficult of the two cases. In isolation, each individual neuron displays periodic bursting with period T_0 in response to a fixed stimulation current (Fig. 6.1(a)). The membrane voltages obey the current balance equation:

$$C_m \frac{dV}{dt} = -I_{\mathrm{Ca}} - I_{\mathrm{K}} - I_{\mathrm{KCa}} - I_L - I_{\mathrm{syn}} + I_{\mathrm{stim}}, \tag{6.1}$$

where $C_m = 20$ μF/cm^2 is the neuron membrane capacitance and $I_{\text{stim}} = 45$ μA/cm^2 is the injected current. The leak current $I_L = g_{\text{L}}(V - E_{\text{L}})$ has a conductance $g_{\text{L}} = 2.0$ mS/cm^2; $E_{\text{L}} = -60$ mV. The spike-generating Ca^{2+} and K$^+$ voltage-dependent ionic currents (I_{Ca} and I_{K}) are of the Hodgkin-Huxley type. The transient calcium current is given by $I_{\text{Ca}} = g_{\text{Ca}}m(V - E_{\text{Ca}})$, where the activation variable m is assumed to respond instantaneously to changes in membrane voltage and has a steady-state response given by $m_\infty = 0.5[1 + \tanh((V + 1.2)/18)]$; $g_{\text{Ca}} = 4.0$ mS/cm^2, $E_{\text{Ca}} = 120$ mV. The delayed rectifier current is given by $I_{\text{K}} = g_{\text{K}}n(V - E_{\text{K}})$, where the activation variable obeys the first-order kinetics: $dn/dt = \psi(0.5[1 + \tanh((V - 12)/17.4)] - n)/\tau_n$; $\tau_n = 1/\cosh((V - 12)/34.8)$; $\psi = 0.23$, $g_{\text{K}} = 8.0$ mS/cm^2, $E_{\text{K}} = -84$ mV. For bursting dynamics, we include $I_{\text{KCa}} = g_{\text{KCa}}z(V - E_{\text{K}})$, where $z = \text{Ca}/[\text{Ca} + 1]$ and Ca is the intracellular calcium concentration which obeys $d\text{Ca}/dt = \epsilon(-\mu I_{\text{Ca}} - \text{Ca})$; $\epsilon = 0.001$, $\mu = 0.02$, $g_{\text{KCa}} = 0.25$ mS/cm^2. The synaptic currents are given by

$$I_{\text{syn}} = g_{\text{syn}}s(V - E_{\text{syn}}), \tag{6.2}$$

where g_{syn} is the maximal synaptic conductance and $E_{\text{syn}} = -75$ mV is the synaptic reversal potential (Fig. 6.1(b)). The gating variable s represents the fraction of docked synaptic neurotransmitters and obeys the first-order kinetics $ds/dt = \alpha F(V_{\text{pre}})(1 - s) - s/\tau_{\text{syn}}$, where $\alpha = 6.25$ ms^{-1}, $\tau_{\text{syn}} = 100$ ms, and $F(V_{\text{pre}})$ is a sigmoid function of the presynaptic membrane voltage $F(V_{\text{pre}}) = 1/(1 + \exp(-(V_{\text{pre}} - \theta_{\text{syn}})/2))$. The threshold parameter θ_{syn} is the value that the presynaptic membrane voltage must exceed for neurotransmitter release to occur. Setting $\theta_{\text{syn}} = 0$ mV ensures that postsynaptic inhibition occurs only when the presynaptic cell spikes [276].

6.2.2 Network configuration and dynamics

Mutual synaptic inhibition in CPG circuits leads to stable patterns of oscillation in which the neurons phase-lock one another, bursting sequentially with fixed phasic relationships. When designing artificial CPG networks we are interested in tailoring the precise timings of these bursts relative to one another, correspond-

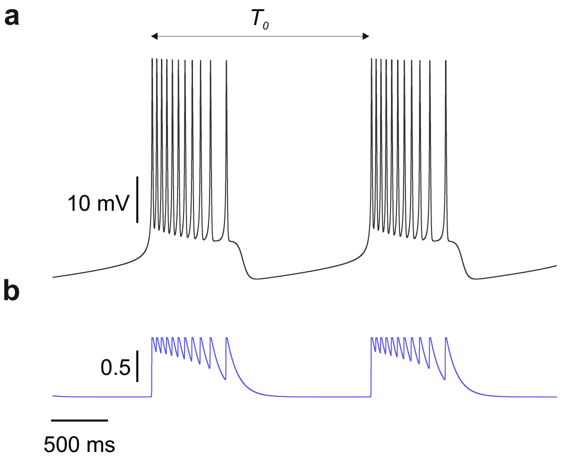

Figure 6.1: (a) Membrane voltage (black) evolution for an individual ML neuron injected with tonic stimulation current $I_{stim} = 45\ \mu\text{A/cm}^2$. The neuron displays bursting dynamics with period T_0. (b) Each spike from the presynaptic neuron (black) elicits neurotransmitter binding to receptors in the postsynaptic neuron, inducing an inhibitory postsynaptic current I_{syn} that acts on the postsynaptic neuron according to Eq. 6.1. The blue trace corresponds to the synaptic gating variable $s(t)$.

ing, for example, to specific gaits or the timings of heart chamber contractions. We first demonstrate these phase-locked dynamics by interconnecting three identical ML neurons with reciprocally inhibitory synapses (Fig. 6.2(a)). We simulate the network (Eqs. 6.1, 6.2) and plot the membrane voltage of the three interconnected cells over thirteen cycle periods (Fig. 6.2(b)), with the raster plot traces representing neuronal spike times.

This network initially stabilises in a steady-state mode labeled A, in which the bursting of N1 is followed by N2, which is followed by N3. In this stable mode the bursting of N2 and N3 are delayed relative to that of N1 by $\Delta\Phi = \frac{1}{3}T_1$ and $\Delta\Phi = \frac{2}{3}T_1$, respectively. We refer to these delays as phase lags. The network will maintain this stable mode unless it receives additional input. 'Multistable' CPG circuits can simultaneously support several stable modes, and transient perturbations may induce a transition from one stable pattern of behavior to another. We demonstrate this property by allowing the network to stabilize and applying a brief current pulse to neuron N2 (Fig. 6.2(b)). This perturbation switches the network to a second stable mode, labeled B, in which the neurons fire in a different order.

In order to simplify the circuit analysis, following the approach of Chapter 5, we visualize the full network dynamics in a two-dimensional phase lag map, recalling the notation of the previous chapter. First, we explicitly define the phase lag $\Delta\Phi_{\text{i1}}$ for each neuron i as the time delay in burst initiation relative to that of the

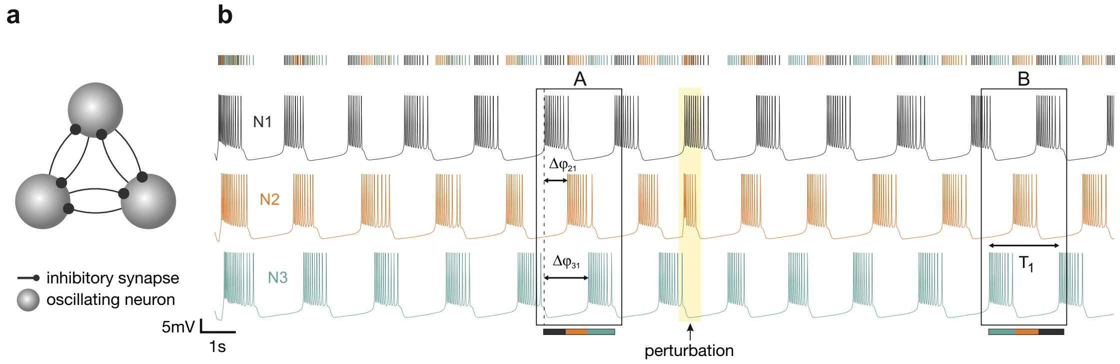

Figure 6.2: (a) Bursting Morris-Lecar neurons were interconnected with mutually inhibitory synapses, $g_{syn} = 10\ \mu\text{S/cm}^2$. (b) The network initially converged towards a phase-locked mode (N1→N2→N3) labeled A. The application of a brief depolarizing current pulse to neuron N2 switches the circuit to a second phase-locked mode, labeled B, in which the neurons burst in a different order. Both modes of activity are stable solutions of the network dynamics with a cycle period of $T = T_1$.

reference neuron N1, normalised by the bursting period T_1 (see Fig. 6.2(a)). Let the onset of bursting in N1 define the start of a new cycle. The state of the system in any given cycle may be defined as the the phase lag pair $\boldsymbol{\Delta\Phi} = (\Delta\Phi_{21}, \Delta\Phi_{31})$. We can initialize the network in a particular phase lag state by staggering the onset of stimulation I_{stim} for each cell. The phase lags in successive cycles can then be measured as the system tends towards a stable mode of oscillation and this set of evolving lags can be plotted as a trajectory in a 2D $(\Delta\Phi_{21}, \Delta\Phi_{31})$ coordinate system. Fig. 6.3(a) shows the phase portrait of trajectories for a reciprocally-coupled network with homogeneous synaptic strengths $g_{\text{syn}} = 1\ \mu\text{S/cm}^2$, where each trajectory emanates from a different initialization of $\boldsymbol{\Delta\Phi}$. The state trajectories converge towards five attracting fixed points (or attractors) in the phase map, each corresponding to a different stable mode of oscillation. Each attractor has a color-coded ‘basin of attraction’, the set of initial phase lags for which the network arrives in the corresponding stable mode. Fig. 6.3(b) shows the phase lag map for a ring network, similar to the reciprocal CPG, but with the conductances of the counterclockwise synapses set to $g_{\text{syn}} = 0\ \mu\text{S/cm}^2$. This CPG is still multistable, but a smaller range of dynamics is observed, with only two attractors present.

By simulating the model equations and generating these phase lag maps, the full dynamics of the networks have been visualized. In the first part of the results

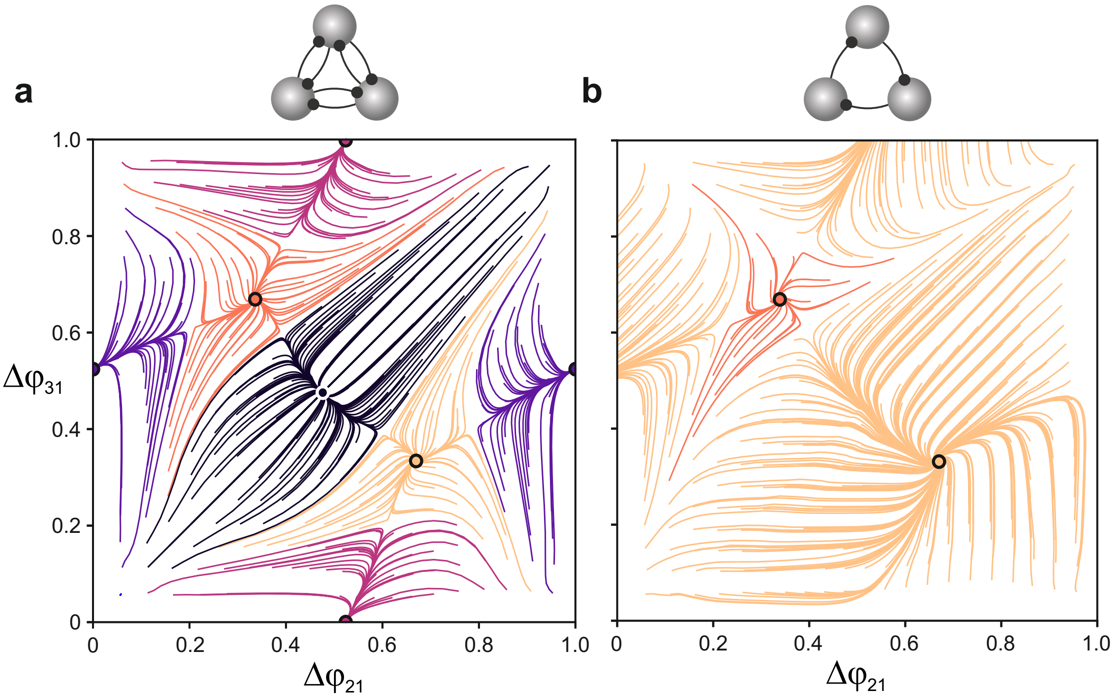

Figure 6.3: (a) Simulated phase lag map for the reciprocal network revealing five stable fixed points (FPs) at $(\Delta\Phi_{21}, \Delta\Phi_{31}) = (\frac{1}{2}, \frac{1}{2})$, $(0, \frac{1}{2})$, $(\frac{1}{2}, 0)$, $(\frac{1}{3}, \frac{2}{3})$, and $(\frac{2}{3}, \frac{1}{3})$. The basins of attraction of the FPs are color coded to match the color of the FP. (b) Phase lag map for the ring network showing the disappearance of the three partially-synchronous attractors, leaving only two attractors at $(\Delta\Phi_{21}, \Delta\Phi_{31}) = (\frac{1}{3}, \frac{2}{3})$, and $(\frac{2}{3}, \frac{1}{3})$.

section, we will show how the PRC of the constituent ML neurons contains all the information needed to fully reproduce these phase portraits, thus justifying our later reduction of network phase-lags to PRC properties. Before we do this, we first describe the process that we use to generate the PRC for a single ML neuron.

6.2.3 Generation of PRCs

In this section, we describe the process of generating a PRC, which is illustrated schematically in Fig. 6.4(a). In short, a single-oscillator PRC encodes the transient effect of synaptic inhibition on the cycle period of a running oscillator. Specifically, we wish to determine the effect of synaptic inhibition on a bursting ML neuron. To this end, two bursting ML neurons are connected as shown, with a presynaptic neuron N2 inhibiting a postsynaptic neuron N1. Initially, N1 is stimulated with

$I_{\text{stim}} = 45\ \mu\text{A/cm}^2$ and exhibits intrinsic bursting with a cycle period T_0. This constitutes our running oscillator. Subsequently, N2 is momentarily stimulated such that it produces a single burst that arrives at some phase $\varphi \in [0,1]$ into the bursting cycle of N1. The synaptic inhibition from N2 then acts to peturb N1, temporarily lengthening or shortening its cycle period by some time ΔT, causing its next burst to occur later or earlier than it otherwise would have. We denote the transiently adjusted period in which this perturbation is received as T_1. By expressing this delay as a fraction of the typical cycle period T_0, and repeating this process for multiple phases φ, the phase resetting curve $f(\varphi) = (T_1(\varphi) - T_0)/T_0$ of the neuron can be plotted. Fig. 6.4(b) shows the PRC calculated for the Morris-Lecar neuron at increasing synaptic strengths g_{syn}. The PRC for a given neuron is dependent both on the strength of the synaptic input and on the intrinsic properties of the neuron. To give a concrete example of how the PRC is computed for the Morris-Lecar neuron, Fig. 6.4(c) shows membrane potential time series used to calculate a single point of the PRC for synaptic strength $g_{\text{syn}} = 20\ \mu\text{S/cm}^2$. To begin with, $N1$ (red line) undergoes bursting with cycle period $T_0 = 2282.6$ ms, until it is briefly inhibited by $N2$, which initiates bursting when $N1$ is at a phase of $\varphi = 0.762$. If $N1$ had not received synaptic inhibition ($g_{\text{syn}} = 0\ \mu\text{S/cm}^2$), then it would have continued to burst uninterrupted (grey dashed line) with period T_0. Instead, the inhibition delays the onset of the next burst by $\Delta T = 176.05$ms. We calculate the phase resetting for this system to be $f(\varphi = 0.762) = \Delta T/T_0 = 7.71 \times 10^{-2}$. Computing the phase response for a range of values $\varphi \in [0,1]$ results in a phase resetting curve (Fig. 6.4(b)).

6.3 Results

6.3.1 PRCs predict network dynamics

It has recently been demonstrated that the existence of synchronous modes of a network can be predicted by an analysis of the PRCs of the constituent neurons [277]. In this section, we justify our later use of PRC properties to estimate neuron and synapse parameters by demonstrating that the PRCs of the constituent neurons contain sufficient information to predict both the stable *and* transient

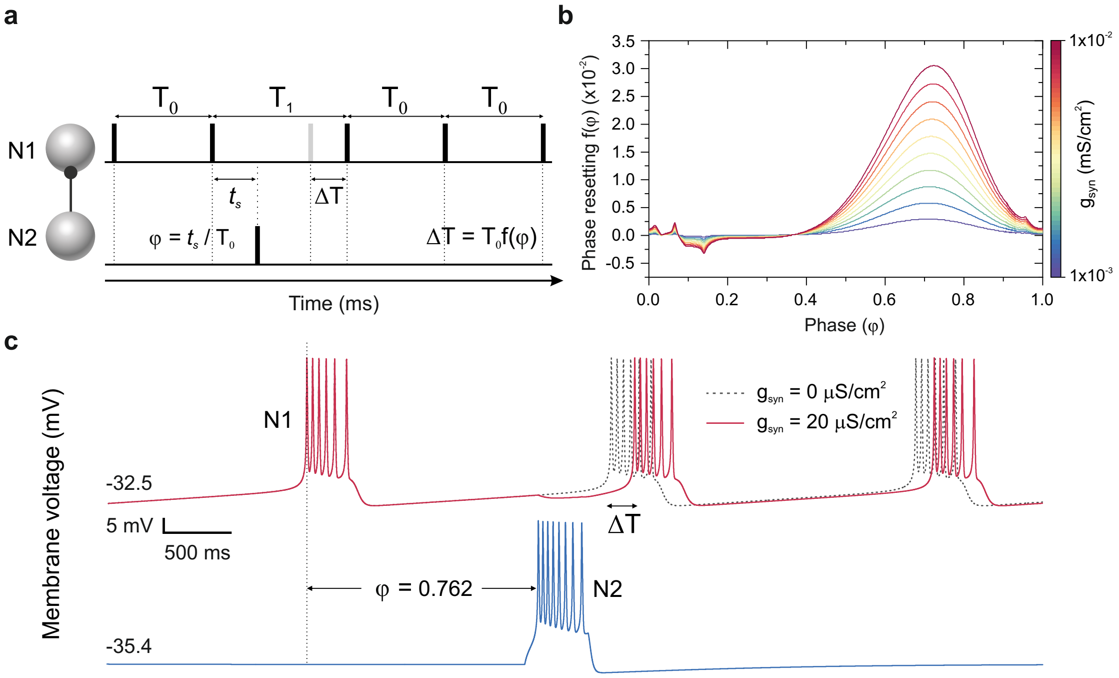

Figure 6.4: Generation of the phase resetting curve. (a) Solid vertical bars indicate the bursting times of the neurons to their left. N1 represents a regular bursting ML model neuron with intrinsic period T_0. A burst in the N2 causes N1 to burst later or earlier than it otherwise would have (grey bar), depending on when it occurs. The change ΔT in the period as a result of the perturbation received at a phase φ is used to generate the phase-resetting curve. T_1 represents the period of the cycle in which the stimulus is received. (b) Example phase resetting curves $f(\varphi)$ for an ML neuron at increasing synaptic strengths g_{syn}. Induced delays correspond to positive regions in the PRC and advances correspond to negative regions.

network dynamics shown in Fig. 6.3(a). We do this by successfully predicting the entire phase portrait solely using the neuron PRCs. We briefly describe the model-free iterative algorithm [222] that we use to extract information from the PRC, and show that it can successfully predict the full dynamics of our CPG network.

The only inputs to the algorithm are the PRCs of the component neurons, the initial phase lags $\mathbf{\Delta\Phi} = (\Delta\Phi_{21}, \Delta\Phi_{31})$ of the neurons, and the intrinsic bursting period of each neuron. The iterator begins by determining which neuron(s) will burst next (i.e. whichever oscillator has the shortest time remaining before reaching a phase of one). Any oscillators that do not burst at this moment have their phases incremented by the (normalised) time to this bursting event. Next, any phase resetting that occurs as a result of the bursting neuron is subtracted from these phases. Then, the phase of the bursting oscillator is reset to zero. This completes one iteration of the algorithm. Once the program has iterated over $N_B = 1000$ bursting events, we can calculate the associated phase lags in each cycle period and plot these evolving phase lags as a trajectory on a return map. By initialising this algorithm with a host of different initial neuron phases $\mathbf{\Delta\Phi}$, we can probe the entire phase space of the network, as before (see Sec. 6.2.1). This PRC-generated phase lag map is shown in Fig. 6.5, and it shows a remarkable likeness to the observed network dynamics (Fig. 6.3a). This is strong evidence in favour of our hypothesis that the PRC may be used to effectively analyse the behaviour of CPG networks.

6.3.2 Stable modes correspond to specific PRC properties

In the previous section, we demonstrated that the PRC contains sufficient information to predict the dynamics of a given network. In this section, we derive the necessary criteria that the individual PRCs must fulfil for a network to display stable oscillatory modes. We simplify our analysis by considering a ring network of N identical oscillators with intrinsic period T_0 in which each neuron is inhibited by the preceding neuron in the ring, as in Fig. 6.3(b). In any phase-locked oscillatory mode, by definition, the relative phases of the oscillators have ceased to change (Fig. 6.2b). This is only possible if the cycle period of all neurons in the network are equal *after* the phase resetting effects of synaptic inhibition are taken into ac-

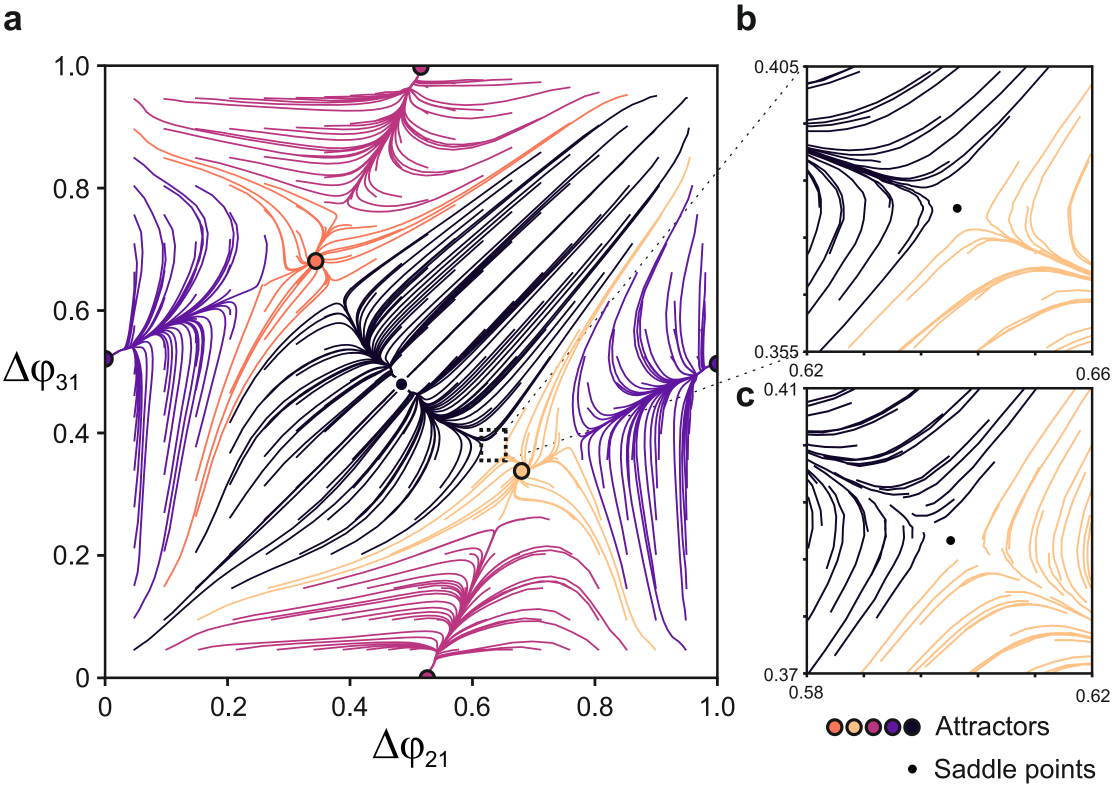

Figure 6.5: (a) PRC-generated phase lag map for the reciprocal network. Just as in the observed network phase-lag map, there are five stable FPs at $(\Delta\Phi_{21}, \Delta\Phi_{31}) = (0.5, 0.5)$, $(0, 0.5)$, $(0.5, 0)$, $(0.33, 0.66)$, and $(0.66, 0.33)$. In addition to correctly predicting the attractor locations, the PRC-generated map displays a strikingly similar trajectory flow globally. (b) Enlarged area of the PRC-generated phase lag map corresponding to a saddle point and its environment. (c) Enlarged area of the same saddle point in the observed network phase lag map. Note the slight repositioning of the saddle point.

count [222]. In this ring circuit, each neuron receives synaptic inhibition from the preceding neuron only once per cycle. Therefore, if each neuron i receives synaptic inhibition from the preceding neuron at a phase $\varphi_i \in \{\varphi_1, \varphi_2, \dots \varphi_N\}$, then the new 'entrained' cycle period of all neurons in the network must be equal to

$$T_1 = T_0[1 + f_i(\varphi_i)] \tag{6.3}$$

in the stable phase-locked mode. In our system, all (identical) cells have the same intrinsic period T_0, and so Eq. 6.3 is equivalent to:

$$f_1(\varphi_1) = f_2(\varphi_2) = ... = f_n(\varphi_n) = ... = f_N(\varphi_N). \tag{6.4}$$

This is our first existence criterion for phase-locked modes. In other words, all neurons must have equal values of $f_i(\varphi_i)$ in order to posess the same entrained period after phase resetting. It is important to note that the N values of φ_i need not be equal. The second existence criterion for phase-locked modes is the trivial fact that, since an oscillator must be in phase with itself, the sum of all the phase differences around the ring must add up to the common entrained period (or some integer multiple thereof). Our second existence criterion for a phase-locked mode is therefore:

$$\sum_{i=1}^{N} \varphi_i = m[1 + f_n(\varphi_n)], \tag{6.5}$$

for some integer $m \in [0, N]$. Recall that our aim is to design an N-cell ring network that converges to a specific stable rhythmic pattern. This is equivalent to the insistence that each neuron i in the ring be phase-locked with its preceding neuron such that it receives synaptic input at some desired phase φ. The above criteria inform us that: (1) each oscillator i must possess a PRC which passes through a specific $(\varphi_i, f_i(\varphi_i))$ coordinate, and that (2) all $f_i(\varphi_i)$ must be equal. We can then use this insight to perform N sequential parameter estimations, each one optimizing the parameters of a single neuron to produce an oscillator with the desired PRC characteristics. By analysing the network in terms of individual cells in this way, we are able to avoid difficulties associated with estimating parameters of an entire network simultaneously. Before demonstrating this sequential approach in Sec. 6.3.4, however, we first demonstrate the nonlinear optimization procedure used for each individual estimation.

6.3.3 Parameter estimation for phase response curves

We have shown that in order to build inhibitory networks with desired rhythmic behaviours, it suffices to optimize individual neuron models such that they each possess the required PRC characteristics. Assuming that we know what the required PRC properties are, we can design artificial target data, $V_{\text{data}}(t)$, that resembles the membrane voltage of a neuron with the required response, ΔT, to a synaptic current $I_{syn}(t)$ received at phase φ. Since the PRC is a function of both the synaptic strength and the neuron parameters, g_{syn} (Fig. 6.4(b)), the optimization problem can then be stated as follows: given a numerical model of the neuron and a parameter g_{syn} that scales the received synaptic current $\tilde{I}_{syn}(t)$, find the set of parameters that most closely reproduces the artificial target data, where $\tilde{I}_{syn}(t) = I_{syn}(t)/g_{syn}$ denotes the unscaled synaptic current (Eq. 6.2). We then use an optimization-based parameter estimation method to fit our neuron model to the target data. Just like in previous chapters, we use nonlinear optimization software IPOPT, which seeks to minimize a least-squares mismatch between the membrane voltage $V(t)$ of a neuron model and the target data $V_{\text{data}}(t)$ by adjusting the model neuron parameters $\boldsymbol{p}$ and the weight g_{syn} of the received synaptic current. The mismatch is represented by the following cost function:

$$C(\mathbf{x}(0), \mathbf{p}, g_{syn}) = \frac{1}{2} \sum_{i=0}^{N} (V_{\text{data}}(t_i) - V(t_i, \mathbf{x}(0), \mathbf{p}, g_{syn}))^2, \tag{6.6}$$

for discrete time points $t_i = iT/N, i = 0 \dots N$ across the assimilation window of duration T. This cost function is minimized subject to the neuron model equations of motion (Eq. 6.1), which are held as constraints on the optimization procedure. Note that the unscaled synaptic current $\tilde{I}_{syn}(t)$ provided to IPOPT replaces the complex current protocol of previous chapters. When the minimization has been performed, the adjusted set of K neuron parameters $\mathbf{p} = [p_0, p_1, ..., p_K]$ and the synaptic weight parameter g_{syn} should correspond to a neuron-synapse pair which matches the target data, producing a completed neuron model which possesses the desired PRC.

Ultimately, we wish to use parameter estimation to obtain neuron and synapse parameters for novel phase-locked modes. However, we first tested the ability of this method to correctly obtain the set of *known* parameters for the system shown in Fig. 6.4(c). In these time series, $N1$ was inhibited by $N2$ at a phase of $\varphi = 0.762$ with a synaptic strength $g_{syn} = 20$ μS/cm^2. To simulate the situation in which the parameters are unknown, we generated artificial target data by taking the unperturbed $N1$ membrane voltage trace (dashed line) and extending the first full cycle period by $\Delta T = 176.05$ ms to mimic the phase resetting effect of the synaptic inhibition $I_{syn}(t)$. This target data is shown in Fig. 6.6 (black trace), where the interpolated data of duration ΔT used to tune the phase response $f(\varphi)$ is highlighted in red. To reiterate, this is the target data that we would generate if we wished to optimize a neuron model with a phase response $f(0.762) = 7.71 \times 10^{-2}$ (Fig. 6.4(c)). We aim to confirm that the estimation procedure can estimate all neuron parameters in addition to the synaptic weight that would have generated such a phase response.

Figure 6.6 shows the best fit of the model (green line) to the artificial target data (black line) across a 8000-ms-long assimilation window. Note that the estimated membrane voltage displays hyperpolarization coincident with the onset of synaptic inhibition, as expected. The parameters extracted during the optimization procedure are listed in Table 6.1. All neuron parameters are estimated to a high level of accuracy, and a correct value of synaptic strength g_{syn} is obtained. This experiment validates our method of artificially constructing membrane voltage data to estimate neuron and synapse parameters corresponding to a desired phase response. It should be noted that since the PRC is a function of both neuron parameters and synaptic strength, the neuron parameters could be fixed during the minimization procedure, leaving g_{syn} as the only adjustable parameter. This has the benefit of reducing the estimation to a single-parameter optimization problem. In the following section, we demonstrate the practical use of this method for estimating synaptic parameters in a ring network of ML neurons.

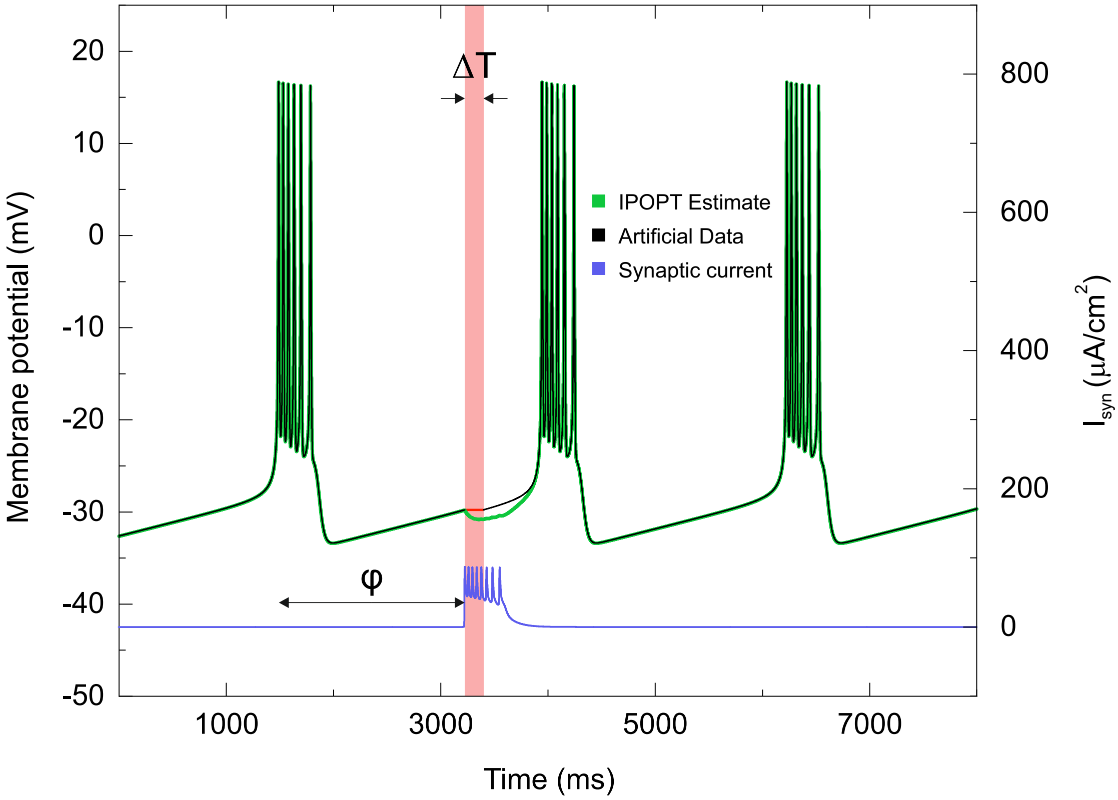

Figure 6.6: Assimilation of artificial ML target data. Membrane voltage oscillations (black trace) of a ML neuron were extended with linear interpolation (red highlight) of duration ΔT to mimic the phase resetting induced by (unscaled) synaptic inhibition $\tilde{I}_{syn}(t)$ (blue trace) received at phase φ. The optimization seeks to estimate the parameters giving rise to such a phase response by adjusting model parameters and a synaptic weight g_{syn} that scales the magnitude of $\tilde{I}_{syn}(t)$. The model was synchronized to the target membrane voltage over a T = 8000-ms-long assimilation window (green trace). The optimum fit produced an estimate of the model parameters shown in Table 6.1.

Parameter ID	Lower bound	Upper bound	True	Estimate
C_m (μF/cm^2)	20	20	20.0	20.0
g_{Ca} (mS/cm^2)	0	20	4.0	3.97
g_{K} (mS/cm^2)	0	20	8.0	8.00
g_{KCa} (mS/cm^2)	0	20	0.25	0.236
g_{L} (mS/cm^2)	0	20	2.0	1.98
E_{Ca} (mV)	100	200	120.0	122.7
E_{K} (mV)	-100	-50	-84.0	-84.2
E_{L} (mV)	-100	-50	-60.0	-59.3
ψ	0.1	1	0.23	0.229
ϵ ($\times 10^{-4}$)	1	100	10.0	9.82
μ	0.01	0.1	0.02	0.020
g_{syn} (μS/cm^2)	0	100	20.0	21.7

Table 6.1: Parameters extracted from artificial target data for the ML neuron compared with their true values (Sec. 6.2.1).

6.3.4 Application to ECG recordings

We now demonstrate how this approach can be used to design functional networks by successfully fitting the phases of a four-cell ring CPG to particular features of an ECG time series recording obtained from an anaesthetised dog. We build the CPG using four of the ML neurons previously described (Sec. 6.2.1, Eq. 6.1) and seek to find synaptic parameters that give rise to neuron dephasings matching the relative phase lags of four target ECG features. In the optimizations performed in this section, we therefore only allow the synaptic parameter g_{syn} to vary, holding all other neuron parameters fixed.

The obtained ECG recording is shown in Fig. 6.7(a). The four target features repeat every cycle, and we label each one in a consecutive cycle, for clarity. The features that we are interested in are: the start (P_i) and end (P_f) of the P wave, corresponding to atrial depolarization (black and orange dashed lines, respectively); the peak of the QRS complex (green line, Q_p), corresponding to ventricular depolarization; and, finally, the peak of the T wave (blue line, T_p), representing ventricular *re*polarization. We first determine the relative phases of the target features and choose to identify each of the four with the onset of bursting in a different ML neuron. Deciding which of the four neurons will burst in

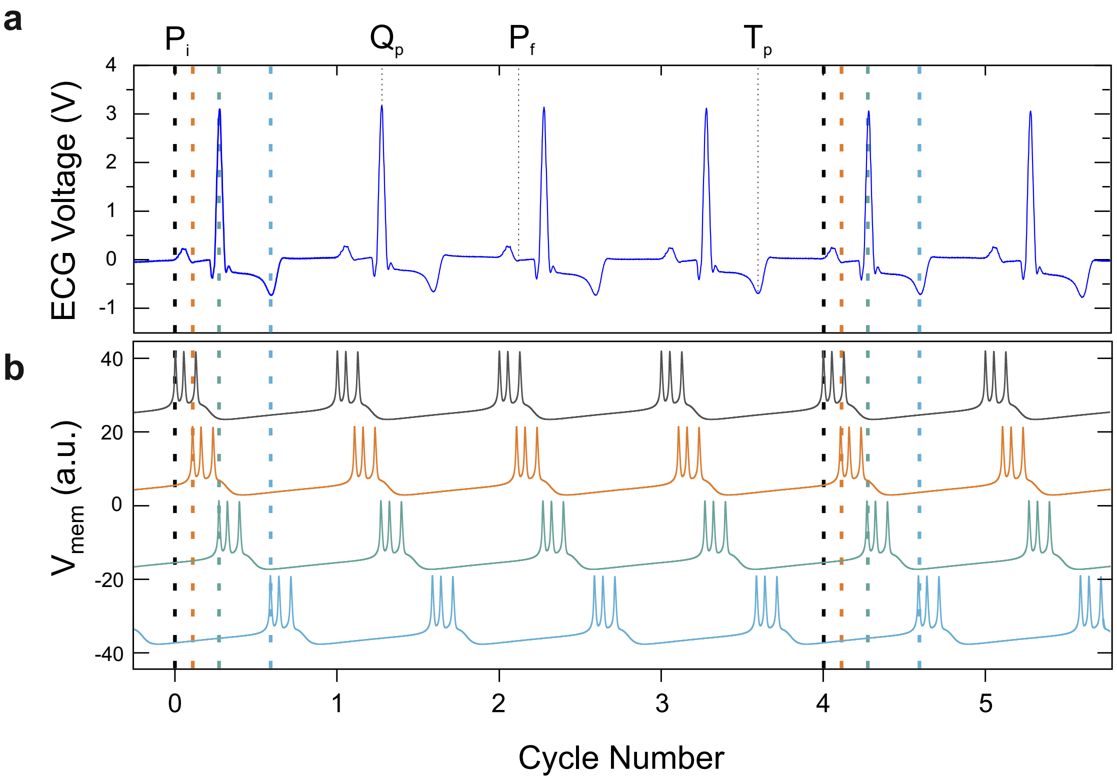

Figure 6.7: (a) Stable ECG recording obtained from an anaesthetised dog. We attempt to match four target features: the start (P_i) and end (P_f) of the P wave, corresponding to atrial depolarization; the peak of the QRS complex (Q_p), corresponding to ventricular depolarization; and the peak of the T wave (T_p), representing ventricular repolarization. (b) Stable four-phase rhythm of the 'completed' CPG. The onset of bursting in the four cells aligns exactly with the onset of the four target features of the ECG recording.

time with each target feature is an arbitrary choice. We choose to take $\mathrm{P}_i \equiv N1$ as the zero-phase reference and calculate the phase lags of the three other features relative to our reference to be:

$$\Delta\Phi_{P_f,P_i} = \Delta\Phi_{41} = 0.137 \tag{6.7}$$

$$\Delta\Phi_{Q_p,P_i} = \Delta\Phi_{31} = 0.296 \tag{6.8}$$

$$\Delta\Phi_{T_p,P_i} = \Delta\Phi_{21} = 0.614. \tag{6.9}$$

We begin by assuming that $N4$ inhibits $N1$ with a synaptic strength $g_{\text{syn}}^{4\to1} = 1$ μS/cm^2. The choice of this first synaptic strength is arbitrary, as the remaining synaptic parameters will be estimated relative to it. Next, we note that in desired network mode, $N1$ receives perturbations from $N4$ at a phase $\varphi = 0.137$ (Eq. 6.7). Having already generated the PRC of the ML neuron for $g_{\text{syn}} = 1$ μS/cm^2 (Fig. 6.4), we can see that the phase response of this cell is $f_1(\varphi_1 = 0.137) = -0.00321$. We then note that in the desired stable mode, $N2$ would receive perturbations from $N1$ at a phase of $\varphi_2 = (1 - 0.614) = 0.386$ (Eq. 6.9). We must therefore ensure that the synaptic weight $g_{\text{syn}}^{1\to 2}$ results in a phase response for N2 of $f_2(0.386) = -0.00321$, in order to satisfy the second criterion Eq. 6.4; namely, that all of the neurons must have equal values of $f_i(\varphi_i)$. In order to estimate $g_{\text{syn}}^{1\to 2}$, we use the target data shown in Fig. 6.6(b), tuning the delay ΔT and adjusting the onset of synaptic inhibition to a phase of $\varphi_2 = 0.386$. We then minimize the cost function (Eq. 6.6) to obtain an estimated synaptic weight $g_{syn}^{1\to 2} = 4.94$ μS/cm^2. Continuing this process around the ring, ensuring Eq. 6.4 is satisfied for each neuron, we obtain estimates for all remaining synapses, thus completing our CPG network model. The estimated parameters for the synaptic weights are listed in Table 6.2.

By forward-integrating the model completed with the estimated synaptic parameters, we can see whether the network predicts the ECG rhythm as desired. Fig. 6.7(b) shows that the network exhibits stable bursting precisely aligned with the ECG targets. It is important to note that while the phase-locked mode estimated here is clearly dynamically stable, the criteria in Eqs. 6.3 and 6.4 only guarantee the existence of such a mode. It is possible that such an estimation procedure would result in the existence of a mode which is unstable to dynamical perturbations and noise. Future work should address this issue by deriving further stability criteria that may be used when generating target data.

6.4 Discussion

Biological CPGs exhibit rhythic behaviour with precise phasic delays between the onset of activity in each constituent neuron. The ability to design artificial CPGs for integration with biological nervous systems requires robust methods for estimating parameters giving rise to this rhythmic behaviour. We have demon-

Parameter	Value (μS/cm^2)
$g_{\text{syn}}^{1\to2}$	4.94
$g_{\text{syn}}^{2\to3}$	7.53
$g_{\text{syn}}^{3\to4}$	2.80
$g_{\text{syn}}^{4\to1}$	1.00

Table 6.2: Synapse parameters for the four-cell identical neuron CPG estimated using the PRC-based optimization method. Forward integrating the completed network model with these parameters gives rise to a phase-locked mode that precisely matches the sequence of heart chamber contractions as recorded in the ECG data.

strated that by reducing the network dynamics to the phase resetting curves of its constituent neurons, one can estimate network parameters individually and sequentially, avoiding the prohibitive computational costs associated with the optimization of whole-network models [272]. By fitting a network rhythm to four target features of an ECG recording, we have demonstrated how this method can be used for the development of functional CPGs with desired phasic timings.

In this chapter, we have used parameter estimation to extract parameters of numerical conductance model neurons. This approach could be extended to construct hardware CPGs by configuring the parameters of a solid state neuron model instead. Hardware CPGs have recently been developed for biomedical applications, including for the modulation of respiratory sinus arrhythmia in rats [53, 206]. This CPG was inspired by the biological network that couples heartbeat and respiration in the mammalian brainstem, however the solid state neurons in the network represented the simple Hodgkin-Huxley model [54]. The component neurons of this biological CPG are well-known, and as such, membrane voltage data could easily be acquired from these respiratory cells [105]. Although the methods of Chapter 4 could be used to replicate the full dynamics of the individual neurons in-silico, the completed solid-state models would need to be coupled using appropriate synaptic parameters to replicate the respiratory CPG in full detail. We propose that the method presented here could be used to construct the full solid-state network that gives rise to the necessary phasic rhythms.

The estimation method developed in this chapter makes use of existence criteria to predict the steady state modes supported by the network. These criteria determine whether or not PRCs of a certain shape give rise to phase-locked dynamics, but give no indication whether or not these modes will be stable [222]. Dror et al. [278] established a criterion for determining the local stability of a steady-state mode of a ring network based on PRCs by deriving local stability results. They use an iterative algorithm, similar to the one used in Sec. 6.2.2, which they describe as a nonlinear discrete time map that defines the values of phase differences in the following cycle in terms of their values in the present cycle. They use the Stable Manifold Theorem [279], which relates the stability of the nonlinear map to that of its local linear approximation, and show that mode stability depends on the eigenvalues of the Jacobian matrix of the map itself [278]. Using these results, they calculate that large positive or negative PRC slopes generally decrease stability, while slopes in the range (0,1) usually increase stability. In practise, when designing CPGs, it suffices to test post-hoc whether the estimated parameter sets result in stable or unstable network modes. However, the work presented in this chapter could be extended to take additional stability criteria of the PRCs into account during the estimation process. This would correspond to further constraints on the construction of the artificial target data used to estimate synaptic parameters. The target data used in this chapter helps to construct a PRC which passes through a single $(\varphi, f(\varphi))$ point. Since these stability criteria relate to PRC slopes, the target data would need to constraint at least two points on the PRC. By using a longer assimilation window encompassing two separate synaptic perturbations in consecutive cycles, these more complex stability criteria could be incorporated.

In summary, the work in this chapter paves the way for a hardware implementation of artificial networks designed for integration with biological nervous systems. The CPG networks considered in this work were composed of identical ML neurons. Future work may seek to relax this assumption, which could enable the building of networks composed of different neuron types, further expanding the range of dynamics of artificial CPG designs. By combining this approach with the methods described in Chapter 4, robust hardware CPG networks can be designed.

Part III

Conclusions and Outlook

Chapter 7

Conclusions and Outlook

7.1 Conclusions

In this thesis, we have used constrained nonlinear optimization and neuromorphic engineering to address several outstanding questions relating to parameter estimation and neurophysiology. We began by studying the problem of multi-valued parameter solutions in the optimization of conductance-based neuron models, demonstrating that sub-optimal solutions can be distinguished from optimal parameter sets under appropriate external stimulation. We then analysed the topography of the cost function in nonlinear inverse problems, and quantified the effect of experimental and model error on local and global minima in the search space. Our results contrast with and complement earlier work which describes the difficulties associated with finding a single global minimum when estimating the parameters of biological systems [33, 136]. We describe the conditions under which these degeneracies can be broken and prescribe a novel method for improving convergence towards the optimal solution. We then applied this estimation framework to the optimization of neuromorphic hardware. By synchronizing solid state neuron models to recorded membrane voltage oscillations of hippocampal and respiratory neurons, we constructed silicon neurons that replicated the exact response of their biological counterparts. Previous attempts to build solid state neurons have managed to reproduce a number of qualitative features of membrane voltage dynamics such as bursting [280] and spike-frequency adaptation [46], but could not replicate the behaviour of individual cells in complete detail. In contrast, the novel neuromorphic ion channel design presented here allows our devices to quantitatively predict membrane oscillations to an unprecedented degree of accuracy [81]. These results pave the way towards the high-fidelity replication of synthetic neuromorphic circuits. We demonstrated the utility of these circuits for investigating open questions in the field of neuroscience by constructing mutually inhibitory networks to probe the mechanisms underlying recently observed inhibition-driven synchrony. We arrived at two complimentary mechanisms - synaptic inhibition delay, and high-frequency entrainment - that are consistent with experimental observations [70], by performing high-resolution parameter sweeps in real-time. These brute-force approaches are necessary for highly nonlinear systems, and the computational time associated with software simulations can be prohibitive [76]. When designing functional network models, this nonlinearity makes estimating synaptic parameters a challenge. We presented a novel estimation methodology that involves reducing neurons in inhibitory networks to their respective phase response curves, and avoids the well-known problem of cost function minima when optimizing an entire network model [272].

7.2 Future work

Throughout this thesis, we have been optimizing the parameters of conductance models composed of a single isopotential compartment. Although we find that these models are sufficient for predicting the dynamics of hippocampal and respiratory neurons, there may be many classes of neurons for which a single compartment model is insufficient. For example, in vivo, dendrites are the predominant receiving sites for synaptic signals. Incoming stimulation can activate dendritic calcium channels, eliciting spikes that forward propagate to the soma [210]. One natural extension of the work presented here would be to expand the conductance model to describe the active properties of dendritic compartments. Such models could have a closer correspondence with the underlying biophysical properties of neurons and could even embed molecular signaling pathway models which are important for studying synaptic plasticity and long-term potentiation of synaptic strengths [281]. Neuromorphic circuitry describing calcium AHP channels has been previously described [81], and could be combined with a dendritic leak current to mimic cell behaviour. By expanding the models in this way, additional complex dynamics that are missing from our implementation could be realized in-silico. Working with multi-compartmental models would certainly make the inference problem more challenging, with an increasing number of free parameters required to describe the larger system. Regardless, we suggest that the novel methodology proposed in the Chapter 3 could be utilised to improve convergence during optimization.

In Chapter 4, we characterised individual respiratory neurons on a neuromorphic chip using data assimilation. We noted that this achievement has relevance for bioelectronic medicine, which requires low power implants that adapt and respond to physiological feedback in real time and in an identical way to real neurons. The next step for this technology would be to characterise the multiple neurons that constitute the respiratory brain stem network [105]. These optimized respiratory neurons could then be coupled together using neuromorphic synapses [181], with the ultimate aim of interfacing functional silicon networks with biological nervous systems as a novel therapy for chronic biocircuit disease. Synthetic central pattern generator hardware has already shown promise in the case of cardiac pacemaking. Pacing with silicon neurons was recently found to increase cardiac output in rats with left ventricular dysfunction [206] by reinstating respiratory sinus arrhythmia, the loss of which is a strong prognostic indicator of cardiovascular pathology. By substituting the neurons in these devices with silicon networks embodying brainstem respiratory dynamics, it is hoped that these adaptive pacemakers would provide naturalistic cardiac pacing superior to the monotonic pacemaking of current cardiac pacemakers [53].

Bibliography

[1] Bruce P Bean. “The action potential in mammalian central neurons”. In: *Nature Reviews Neuroscience* 8.6 (2007), pp. 451–465.

[2] Fred Rieke et al. *Spikes: exploring the neural code.* Vol. 7. 1. MIT press Cambridge, 1999.

[3] Alan L Hodgkin and Andrew F Huxley. “A quantitative description of membrane current and its application to conduction and excitation in nerve”. In: *The Journal of physiology* 117.4 (1952), p. 500.

[4] Christof J Schwiening. “A brief historical perspective: Hodgkin and Huxley”. In: *The Journal of physiology* 590.Pt 11 (2012), p. 2571.

[5] Mark Nelson and John Rinzel. “The hodgkin—huxley model”. In: *The book of genesis.* Springer, 1998, pp. 29–49.

[6] Daniel Soudry and Ron Meir. “Conductance-based neuron models and the slow dynamics of excitability”. In: *Frontiers in Computational Neuroscience* 6 (2012), p. 4.

[7] Eric B Hendrickson, Jeremy R Edgerton, and Dieter Jaeger. “The capabilities and limitations of conductance-based compartmental neuron models with reduced branched or unbranched morphologies and active dendrites”. In: *Journal of computational neuroscience* 30.2 (2011), pp. 301–321.

[8] Frances K Skinner. “Conductance-based models”. In: *Scholarpedia* 1.11 (2006), p. 1408.

[9] Romain Brette. “What is the most realistic single-compartment model of spike initiation?” In: *PLoS Comput Biol* 11.4 (2015), e1004114.

[10] James M Bower. *Modeling the nervous system.* 1992.

[11] Astrid A Prinz, Cyrus P Billimoria, and Eve Marder. “Alternative to hand-tuning conductance-based models: construction and analysis of databases of model neurons”. In: *Journal of neurophysiology* 90.6 (2003), pp. 3998–4015.

[12] Pablo Achard and Erik De Schutter. “Complex parameter landscape for a complex neuron model”. In: *PLoS computational biology* 2.7 (2006), e94.

[13] Werner Van Geit, Erik De Schutter, and Pablo Achard. “Automated neuron model optimization techniques: a review”. In: *Biological cybernetics* 99.4-5 (2008), pp. 241–251.

[14] Henry DI Abarbanel et al. “Dynamical parameter and state estimation in neuron models”. In: *The dynamic brain: an exploration of neuronal variability and its functional significance* (2011).

[15] Jonathan W Pillow et al. “A model-based spike sorting algorithm for removing correlation artifacts in multi-neuron recordings”. In: *PloS one* 8.5 (2013), e62123.

[16] Christina M Weaver and Susan L Wearne. “The role of action potential shape and parameter constraints in optimization of compartment models”. In: *Neurocomputing* 69.10-12 (2006), pp. 1053–1057.

[17] Renaud Jolivet et al. “Predicting spike timing of neocortical pyramidal neurons by simple threshold models”. In: *Journal of computational neuroscience* 21.1 (2006), pp. 35–49.

[18] Liam Paninski, Eero P Simoncelli, and Jonathan W Pillow. “Maximum likelihood estimation of a stochastic integrate-and-fire neural model”. In: *Advances in Neural Information Processing Systems.* 2004, pp. 1311–1318.

[19] Renaud Jolivet et al. “The quantitative single-neuron modeling competition”. In: *Biological cybernetics* 99.4-5 (2008), p. 417.

[20] Bryan A Toth et al. “Dynamical estimation of neuron and network properties I: variational methods”. In: *Biological cybernetics* 105.3-4 (2011), pp. 217–237.

[21] C Daniel Meliza et al. “Estimating parameters and predicting membrane voltages with conductance-based neuron models”. In: *Biological cybernetics* 108.4 (2014), pp. 495–516.

[22] Alain Nogaret et al. “Automatic construction of predictive neuron models through large scale assimilation of electrophysiological data”. In: *Scientific reports* 6.1 (2016), pp. 1–14.

[23] Joseph D Taylor, Samuel Winnall, and Alain Nogaret. “Estimation of neuron parameters from imperfect observations”. In: *PLOS Computational Biology* 16.7 (2020), e1008053.

[24] Floris Takens. “Detecting strange attractors in turbulence”. In: *Dynamical systems and turbulence, Warwick 1980*. Springer, 1981, pp. 366–381.

[25] Lyle Noakes. “The Takens embedding theorem”. In: *International Journal of Bifurcation and Chaos* 1.04 (1991), pp. 867–872.

[26] Jingxin Ye et al. “Systematic variational method for statistical nonlinear state and parameter estimation”. In: *Physical Review E* 92.5 (2015), p. 052901.

[27] Randall D Hayes et al. “Estimation of single-neuron model parameters from spike train data”. In: *Neurocomputing* 65 (2005), pp. 517–529.

[28] Isao Tokuda et al. “Parameter estimation for neuron models”. In: *AIP Conference Proceedings*. Vol. 676. 1. American Institute of Physics. 2003, pp. 251–256.

[29] Christoph Zimmer, Frank T Bergmann, and Sven Sahle. “Reducing local minima in fitness landscapes of parameter estimation by using piecewise evaluation and state estimation”. In: *arXiv preprint arXiv:1601.04458* (2016).

[30] Henry DI Abarbanel, Mark Kostuk, and William Whartenby. “Data assimilation with regularized nonlinear instabilities”. In: *Quarterly Journal of the Royal Meteorological Society: A journal of the atmospheric sciences, applied meteorology and physical oceanography* 136.648 (2010), pp. 769–783.

[31] Astrid A Prinz, Dirk Bucher, and Eve Marder. “Similar network activity from disparate circuit parameters”. In: *Nature neuroscience* 7.12 (2004), pp. 1345–1352.

[32] Guillaume Drion, Timothy O’Leary, and Eve Marder. “Ion channel degeneracy enables robust and tunable neuronal firing rates”. In: *Proceedings of the National Academy of Sciences* 112.38 (2015), E5361–E5370.

[33] Timothy O’Leary, Alexander C Sutton, and Eve Marder. “Computational models in the age of large datasets”. In: *Current opinion in neurobiology* 32 (2015), pp. 87–94.

[34] Mark S Goldman et al. “Global structure, robustness, and modulation of neuronal models”. In: *Journal of Neuroscience* 21.14 (2001), pp. 5229–5238.

[35] Adam L Taylor, Jean-Marc Goaillard, and Eve Marder. “How multiple conductances determine electrophysiological properties in a multicompartment model”. In: *Journal of Neuroscience* 29.17 (2009), pp. 5573–5586.

[36] Thomas B Kepler, LF Abbott, and Eve Marder. “Reduction of conductance-based neuron models”. In: *Biological cybernetics* 66.5 (1992), pp. 381–387.

[37] Inga Blundell et al. “Automatically selecting a suitable integration scheme for systems of differential equations in neuron models”. In: *Frontiers in neuroinformatics* 12 (2018), p. 50.

[38] Dan FM Goodman and Romain Brette. “Brian: a simulator for spiking neural networks in python”. In: *Frontiers in neuroinformatics* 2 (2008), p. 5.

[39] William W Lytton, Mark Stewart, and Michael Hines. “Simulation of large networks: technique and progress”. In: *Computational neuroscience in epilepsy*. Elsevier, 2008, pp. 3–17.

[40] Romain Brette et al. “Simulation of networks of spiking neurons: a review of tools and strategies”. In: *Journal of computational neuroscience* 23.3 (2007), pp. 349–398.

[41] Misha Mahowald and Rodney Douglas. “A silicon neuron”. In: *Nature* 354.6354 (1991), pp. 515–518.

[42] Giacomo Indiveri and Timothy K Horiuchi. “Frontiers in neuromorphic engineering”. In: *Frontiers in neuroscience* 5 (2011), p. 118.

[43] Tor Sverre Lande. *Neuromorphic systems engineering: neural networks in silicon*. Vol. 447. Springer Science & Business Media, 1998.

[44] Steve Furber. “Large-scale neuromorphic computing systems”. In: *Journal of neural engineering* 13.5 (2016), p. 051001.

[45] Giacomo Indiveri. “Neuromorphic engineering”. In: *Springer Handbook of Computational Intelligence*. Springer, 2015, pp. 715–725.

[46] Giacomo Indiveri. “A low-power adaptive integrate-and-fire neuron circuit”. In: *Proceedings of the 2003 International Symposium on Circuits and Systems, 2003. ISCAS’03.* Vol. 4. IEEE. 2003, pp. IV–IV.

[47] Venkat Rangan et al. “A subthreshold aVLSI implementation of the Izhikevich simple neuron model”. In: *2010 Annual International Conference of the IEEE Engineering in Medicine and Biology*. IEEE. 2010, pp. 4164–4167.

[48] BERNABE Linares-Barranco et al. “A CMOS implementation of FitzHugh-Nagumo neuron model”. In: *IEEE Journal of Solid-State Circuits* 26.7 (1991), pp. 956–965.

[49] André Van Schaik et al. “A log-domain implementation of the Mihalas-Niebur neuron model”. In: *Proceedings of 2010 IEEE International Symposium on Circuits and Systems*. IEEE. 2010, pp. 4249–4252.

[50] Emre Ozgur Neftci et al. “Dynamic state and parameter estimation applied to neuromorphic systems”. In: *Neural computation* 24.7 (2012), pp. 1669–1694.

[51] Catherine D Schuman et al. “An evolutionary optimization framework for neural networks and neuromorphic architectures”. In: *2016 International Joint Conference on Neural Networks (IJCNN)*. IEEE. 2016, pp. 145–154.

[52] TS Lande. “Neuromorphic medical electronics”. In: *2001 IEEE International Symposium on Circuits and Systems (ISCAS)*. IEEE. 2001, pp. 1–6.

[53] Alain Nogaret et al. "Silicon central pattern generators for cardiac diseases". In: *The Journal of physiology* 593.4 (2015), pp. 763–774.

[54] Alain Nogaret et al. "Modulation of respiratory sinus arrhythmia in rats with central pattern generator hardware". In: *Journal of neuroscience methods* 212.1 (2013), pp. 124–132.

[55] Peter Uhlhaas et al. "Neural synchrony in cortical networks: history, concept and current status". In: *Frontiers in integrative neuroscience* 3 (2009), p. 17.

[56] Peter J Uhlhaas et al. "Neural synchrony and the development of cortical networks". In: *Trends in cognitive sciences* 14.2 (2010), pp. 72–80.

[57] Wolf Singer. "Time as coding space in the cerebral cortex". In: *Functional Neuroimaging of Visual Cognition.* Oxford University Press, 2004, pp. 99–123.

[58] Joachim Gross et al. "Modulation of long-range neural synchrony reflects temporal limitations of visual attention in humans". In: *Proceedings of the national Academy of Sciences* 101.35 (2004), pp. 13050–13055.

[59] Catherine Tallon-Baudry. "Attention and awareness in synchrony". In: *Trends in cognitive sciences* 8.12 (2004), pp. 523–525.

[60] Catherine Tallon-Baudry, Olivier Bertrand, and Catherine Fischer. "Oscillatory synchrony between human extrastriate areas during visual short-term memory maintenance". In: *Journal of Neuroscience* 21.20 (2001), RC177–RC177.

[61] Friedhelm Hummel and Christian Gerloff. "Larger interregional synchrony is associated with greater behavioral success in a complex sensory integration task in humans". In: *Cerebral Cortex* 15.5 (2005), pp. 670–678.

[62] Wolf Singer. "Binding by synchrony". In: *Scholarpedia* 2.12 (2007), p. 1657.

[63] Edward G Jones. "The thalamic matrix and thalamocortical synchrony". In: *Trends in neurosciences* 24.10 (2001), pp. 595–601.

[64] G Buzsáki et al. "Oscillatory and intermittent synchrony in the hippocampus: relevance to memory trace formation". In: *Temporal coding in the brain.* Springer, 1994, pp. 145–172.

[65] Mario Galarreta and Shaul Hestrin. “Spike transmission and synchrony detection in networks of GABAergic interneurons”. In: *Science* 292.5525 (2001), pp. 2295–2299.

[66] Roger D Traub et al. “Gap junctions between interneuron dendrites can enhance synchrony of gamma oscillations in distributed networks”. In: *Journal of Neuroscience* 21.23 (2001), pp. 9478–9486.

[67] Nicolas Brunel and Xiao-Jing Wang. “What determines the frequency of fast network oscillations with irregular neural discharges? I. Synaptic dynamics and excitation-inhibition balance”. In: *Journal of neurophysiology* 90.1 (2003), pp. 415–430.

[68] Bidesh K Bera, Dibakar Ghosh, and Tanmoy Banerjee. “Imperfect traveling chimera states induced by local synaptic gradient coupling”. In: *Physical Review E* 94.1 (2016), p. 012215.

[69] Jay R Gibson, Michael Beierlein, and Barry W Connors. “Functional properties of electrical synapses between inhibitory interneurons of neocortical layer 4”. In: *Journal of neurophysiology* (2005).

[70] Hang Hu, Yunyong Ma, and Ariel Agmon. “Submillisecond firing synchrony between different subtypes of cortical interneurons connected chemically but not electrically”. In: *Journal of Neuroscience* 31.9 (2011), pp. 3351–3361.

[71] Yunyong Ma et al. “Distinct subtypes of somatostatin-containing neocortical interneurons revealed in transgenic mice”. In: *Journal of Neuroscience* 26.19 (2006), pp. 5069–5082.

[72] Eve Marder and Adam L Taylor. “Multiple models to capture the variability in biological neurons and networks”. In: *Nature neuroscience* 14.2 (2011), pp. 133–138.

[73] Eve Marder and Dirk Bucher. “Central pattern generators and the control of rhythmic movements”. In: *Current biology* 11.23 (2001), R986–R996.

[74] Ronald M Harris-Warrick. “General principles of rhythmogenesis in central pattern generator networks”. In: *Progress in brain research.* Vol. 187. Elsevier, 2010, pp. 213–222.

[75] Eve Marder et al. “Invertebrate central pattern generation moves along”. In: *Current Biology* 15.17 (2005), R685–R699.

[76] Jeremy Wojcik et al. “Key bifurcations of bursting polyrhythms in 3-cell central pattern generators”. In: *PloS one* 9.4 (2014).

[77] THELMA L Williams et al. “Forcing of coupled nonlinear oscillators: studies of intersegmental coordination in the lamprey locomotor central pattern generator”. In: *Journal of neurophysiology* 64.3 (1990), pp. 862–871.

[78] Roberto F Galán, G Bard Ermentrout, and Nathaniel N Urban. “Efficient estimation of phase-resetting curves in real neurons and its significance for neural-network modeling”. In: *Physical review letters* 94.15 (2005), p. 158101.

[79] Carmen C Canavier. “Phase response curve”. In: *Scholarpedia* 1.12 (2006), p. 1332.

[80] Ashok S Chauhan, Joseph D Taylor, and Alain Nogaret. “Dual mechanism for the emergence of synchronization in inhibitory neural networks”. In: *Scientific reports* 8.1 (2018), pp. 1–9.

[81] Kamal Abu-Hassan et al. “Optimal solid state neurons”. In: *Nature communications* 10.1 (2019), pp. 1–13.

[82] B. Hille. *Ionic Channels of Excitable Membranes*. Sinauer Associates, 1984. ISBN: 9780878933228. URL: `https://books.google.co.uk/books?id=AU9RAAAAMAAJ`.

[83] Dale Purves et al. “Neuroscience. 4th”. In: *Sunderland, Mass.: Sinauer. xvii* 857 (2008), p. 944.

[84] John Rubenstein and Pasko Rakic. *Patterning and Cell Type Specification in the Developing CNS and PNS: Comprehensive Developmental Neuroscience*. Vol. 1. Academic Press, 2013.

[85] David C Gadsby. “Ion channels versus ion pumps: the principal difference, in principle”. In: *Nature reviews Molecular cell biology* 10.5 (2009), pp. 344–352.

[86] R Goldshlegger et al. "The effect of membrane potential on the mammalian sodium-potassium pump reconstituted into phospholipid vesicles." In: *The Journal of Physiology* 387.1 (1987), pp. 331–355.

[87] James S Trimmer and Kenneth J Rhodes. "Localization of voltage-gated ion channels in mammalian brain". In: *Annu. Rev. Physiol.* 66 (2004), pp. 477–519.

[88] David J Schulz, Jean-Marc Goaillard, and Eve Marder. "Variable channel expression in identified single and electrically coupled neurons in different animals". In: *Nature neuroscience* 9.3 (2006), pp. 356–362.

[89] Cengiz Günay, Jeremy R Edgerton, and Dieter Jaeger. "Channel density distributions explain spiking variability in the globus pallidus: a combined physiology and computer simulation database approach". In: *Journal of Neuroscience* 28.30 (2008), pp. 7476–7491.

[90] Michael C Vanier and James M Bower. "A comparative survey of automated parameter-search methods for compartmental neural models". In: *Journal of computational neuroscience* 7.2 (1999), pp. 149–171.

[91] Clay M Armstrong and Bertil Hille. "Voltage-gated ion channels and electrical excitability". In: *Neuron* 20.3 (1998), pp. 371–380.

[92] Walther Nernst. "Die elektromotorische wirksamkeit der jonen". In: *Zeitschrift für physikalische Chemie* 4.1 (1889), pp. 129–181.

[93] Walther Nernst. *Experimental and theoretical applications of thermodynamics to chemistry.* C. Scribner's sons, 1907.

[94] Martin Pospischil et al. "Minimal Hodgkin–Huxley type models for different classes of cortical and thalamic neurons". In: *Biological cybernetics* 99.4-5 (2008), pp. 427–441.

[95] Eric B Hendrickson, Jeremy R Edgerton, and Dieter Jaeger. "The use of automated parameter searches to improve ion channel kinetics for neural modeling". In: *Journal of computational neuroscience* 31.2 (2011), pp. 329–346.

[96] Alon Korngreen and Bert Sakmann. “Voltage-gated K+ channels in layer 5 neocortical pyramidal neurones from young rats: subtypes and gradients”. In: *The Journal of physiology* 525.3 (2000), pp. 621–639.

[97] Roger D Traub et al. “A model of a CA3 hippocampal pyramidal neuron incorporating voltage-clamp data on intrinsic conductances”. In: *Journal of neurophysiology* 66.2 (1991), pp. 635–650.

[98] David A McCormick et al. “Comparative electrophysiology of pyramidal and sparsely spiny stellate neurons of the neocortex”. In: *Journal of neurophysiology* 54.4 (1985), pp. 782–806.

[99] ER Kandel and WA Spencer. “Electrophysiology of hippocampal neurons: II. After-potentials and repetitive firing”. In: *Journal of Neurophysiology* 24.3 (1961), pp. 243–259.

[100] Jorge Golowasch et al. “Failure of averaging in the construction of a conductance-based neuron model”. In: *Journal of neurophysiology* 87.2 (2002), pp. 1129–1131.

[101] Ryota Kobayashi, Yasuhiro Tsubo, and Shigeru Shinomoto. “Made-to-order spiking neuron model equipped with a multi-timescale adaptive threshold”. In: *Frontiers in computational neuroscience* 3 (2009), p. 9.

[102] Peter Dayan, Laurence F Abbott, et al. “Theoretical neuroscience: computational and mathematical modeling of neural systems”. In: *Journal of Cognitive Neuroscience* 15.1 (2003), pp. 154–155.

[103] Shimon Marom and LF Abbott. “Modeling state-dependent inactivation of membrane currents”. In: *Biophysical journal* 67.2 (1994), pp. 515–520.

[104] Johan F Storm. “Action potential repolarization and a fast after-hyperpolarization in rat hippocampal pyramidal cells.” In: *The Journal of physiology* 385.1 (1987), pp. 733–759.

[105] Davi JA Moraes, Daniel B Zoccal, and Benedito H Machado. “Medullary respiratory network drives sympathetic overactivity and hypertension in rats submitted to chronic intermittent hypoxia”. In: *Hypertension* 60.6 (2012), pp. 1374–1380.

[106] Eugen M. Izhikevich. *Dynamical systems in neuroscience: the geometry of excitability and bursting.* MIT University Press, 2007.

[107] Christine Grienberger and Arthur Konnerth. “Imaging calcium in neurons”. In: *Neuron* 73.5 (2012), pp. 862–885.

[108] JR Huguenard. “Low-threshold calcium currents in central nervous system neurons”. In: *Annual review of physiology* 58.1 (1996), pp. 329–348.

[109] Kerry L Zbicz and Forrest F Weight. “Transient voltage and calcium-dependent outward currents in hippocampal CA3 pyramidal neurons”. In: *Journal of neurophysiology* 53.4 (1985), pp. 1038–1058.

[110] David A McCormick and John R Huguenard. “A model of the electrophysiological properties of thalamocortical relay neurons”. In: *Journal of neurophysiology* 68.4 (1992), pp. 1384–1400.

[111] John Rinzel and G Bard Ermentrout. “Analysis of neural excitability and oscillations”. In: *Methods in neuronal modeling* 2 (1998), pp. 251–292.

[112] G Bard Ermentrout and David H Terman. *Mathematical foundations of neuroscience.* Vol. 35. Springer Science & Business Media, 2010.

[113] Erik De Schutter. *Computational modeling methods for neuroscientists.* The MIT Press, 2010.

[114] Asaf Gal et al. “Dynamics of excitability over extended timescales in cultured cortical neurons”. In: *Journal of Neuroscience* 30.48 (2010), pp. 16332–16342.

[115] F Bouttier and P Courtier. “Data assimilation concepts and methods March 1999”. In: *Meteorological training course lecture series. ECMWF* 718 (2002), p. 59.

[116] Henry Abarbanel. *Predicting the future: completing models of observed complex systems.* Springer, 2013.

[117] Sebastian Reich and Colin Cotter. *Probabilistic forecasting and Bayesian data assimilation.* Cambridge University Press, 2015.

[118] Thomas Deneux et al. "Accurate spike estimation from noisy calcium signals for ultrafast three-dimensional imaging of large neuronal population in-vivo". In: *Nature Communications* 7 (2016), p. 12190.

[119] Agus Hartoyo et al. "Parameter estimation and identifiability in a neural population model for electro-cortical activity". In: *PLoS Computational Biology* 15 (2019), e1006694.

[120] Quentin JM Huys, Misha B Ahrens, and Liam Paninski. "Efficient estimation of detailed single-neuron models". In: *Journal of neurophysiology* 96.2 (2006), pp. 872–890.

[121] Agoston E Eiben, James E Smith, et al. *Introduction to evolutionary computing*. Springer, 2003.

[122] M. Pospischil et al. "Minimal Hodgkin-Huxley type models for different classes of cortical and thalamic neurons". In: *Biol. Cybern.* 99 (2008), p. 427.

[123] Louis M Pecora and Thomas L Carroll. "Synchronization in chaotic systems". In: *Physical review letters* 64.8 (1990), p. 821.

[124] Lorenz T Biegler and Victor M Zavala. "Large-scale nonlinear programming using IPOPT: An integrating framework for enterprise-wide dynamic optimization". In: *Computers & Chemical Engineering* 33.3 (2009), pp. 575–582.

[125] Philip E Gill, Walter Murray, and Michael A Saunders. "SNOPT: An SQP algorithm for large-scale constrained optimization". In: *SIAM review* 47.1 (2005), pp. 99–131.

[126] Stephen Boyd, Stephen P Boyd, and Lieven Vandenberghe. *Convex optimization*. Cambridge university press, 2004.

[127] Christian Darken and John Moody. "Towards faster stochastic gradient search". In: *Advances in neural information processing systems*. 1992, pp. 1009–1016.

[128] Henry DI Abarbanel et al. "Dynamical state and parameter estimation". In: *SIAM Journal on Applied Dynamical Systems* 8.4 (2009), pp. 1341–1381.

[129] Andreas Wächter. “Short tutorial: getting started with ipopt in 90 minutes”. In: *Dagstuhl Seminar Proceedings*. Schloss Dagstuhl-Leibniz-Zentrum für Informatik. 2009.

[130] William H Press et al. *Numerical recipes in C*. 1988.

[131] Edward N Lorenz. “Deterministic nonperiodic flow”. In: *Journal of the atmospheric sciences* 20.2 (1963), pp. 130–141.

[132] Jan Schumann-Bischoff and Ulrich Parlitz. “State and parameter estimation using unconstrained optimization”. In: *Physical Review E* 84.5 (2011), p. 056214.

[133] Alain Nogaret et al. “Automatic construction of predictive neuron models through large scale assimilation of electrophysiological data”. In: *Scientific Reports* 6 (2016), p. 32749.

[134] C. Daniel Meliza et al. “Estimating parameters and predicting membrane voltages with conductance-based neuron models”. In: *Biological Cybernetics* 108 (2014), p. 495.

[135] Timothy O’Leary, Alexander C. Sutton, and Eve Marder. “Computational models in the age of large datasets”. In: *Current opinion in neurobiology* 32 (2015), pp. 87–94.

[136] Ryan N Gutenkunst et al. “Universally sloppy parameter sensitivities in systems biology models”. In: *PLoS computational biology* 3.10 (2007), e189.

[137] Adriane G. Otopalik et al. “When complex neuronal structures may not matter”. In: *eLife* (2017), e23508.

[138] Astrid A. Prinz, Dirk Bucher, and Eve Marder. “Similar network activity from disparate circuit parameters”. In: *Nature neuroscience* 7 (2004), p. 1345.

[139] J. M. Goaillard et al. “Functional consequences of animal-to-animal variation in circuit parameters”. In: *Nature Neuroscience* 12 (2009), p. 1424.

[140] Eve Marder and Jean-Marc Goaillard. “Variability, compensation and homeostasis in neuron and network function”. In: *Nature Reviews Neuroscience* 7 (2006), pp. 563–574.

[141] Michele Migliore and Gordon M. Shepherd. "An integrated approach to classifying neuronal phenotypes". In: *Nature Reviews Neuroscience* 6 (2005), p. 810.

[142] B. J. Molyneaux et al. "Neuronal subtype classification in the cerebral cortex". In: *Nature Reviews Neuroscience* 8 (2007), p. 427.

[143] Hongkui Zeng and Joshua R. Sanes. "Neuronal cell-type classification: challenges opportunities and path forward". In: *Nature Reviews Neuroscience* 18 (2017), p. 530.

[144] C. Savio Chan et al. "HCN channelopathy in external globus pallidus neurons in models of Parkinson's disease". In: *Nature Neuroscience* 14 (2011), p. 85.

[145] J. T. Brown et al. "Altered intrinsic neuronal excitability and reduced Na+ currents in a mouse model of Alzheimer's disease". In: *Neurobiology of aging* 32 (2011), 2109.e1–2109.e14.

[146] Bruce L. Kagan et al. "The channel hypothesis of Alzheimer's disease: current status". In: *Peptides* 23 (2002), p. 1311.

[147] Chakroborty Shreaya and Grace E. Stutzmann. "Calcium channelopathies and Alzheimer's disease: insight into therapeutic success and failure". In: *European Journal of Pharmacology* 739 (2014), pp. 83–95.

[148] Floris Takens. "Detecting strange attractors in turbulence". In: *Dynamical systems and turbulence, Warwick 1980*. Springer, 1981, pp. 366–381.

[149] Dirk Aeyels. "Generic observability of differentiable systems". In: *SIAM Journal on Control and Optimization* 19.5 (1981), pp. 595–603.

[150] Christophe Letellier, Luis Aguirre, and Jean Maquet. "How the choice of the observable may influence the analysis of nonlinear dynamical systems". In: *Communications in Nonlinear Science* 11 (2006), pp. 555–576.

[151] Ulrich Parlitz, Jan Schumann-Bischoff, and Stefan Luther. "Local observability of state variables and parameters in nonlinear modeling quantified by delay reconstruction". In: *Chaos: An Interdisciplinary Journal of Nonlinear Science* 24.2 (2014), p. 024411.

[152] Ulrich Parlitz, Jan Schumann-Bischoff, and Stefan Luther. “Quantifying uncertainty in state and parameter estimation”. In: *Physical Review E* 89.5 (2014), p. 050902.

[153] J. Schumann-Bischoff, S. Luther, and U. Parlitz. “Estimability and dependency analysis of model parameters based on delay estimates”. In: *Physical Review E* 94 (2016), p. 032221.

[154] Jingxin Ye et al. “Systematic variational method for statistical nonlinear state and parameter estimation”. In: *Phys. Rev. E* 92 (2015), p. 052901.

[155] Alan L. Hodgkin and Andrew F. Huxley. “A quantitative description of membrane current and its application to conduction and excitation in nerve”. In: *The Journal of Physiology* 117.4 (1952), pp. 500–544.

[156] Davi J. A. Moraes et al. “Electrophysiological properties of rostral ventrolateral medulla presympathetic neurons modulated by the respiratory network in rats”. In: *Journal of Neuroscience* 33.49 (2013), pp. 19223–19237.

[157] Stephen Wolfram et al. *The MATHEMATICA® book, version 4*. Cambridge university press, 1999.

[158] Daniel R. Creveling, Philip E. Gill, and Henry D. I. Abarbanel. “State and parameter estimation in nonlinear systems as an optimal tracking problem”. In: *Physics Letters A* 372.15 (2008), pp. 2640–2644.

[159] Kevin H Hobbs and Scott L Hooper. “Using complicated, wide dynamic range driving to develop models of single neurons in single recording sessions”. In: *Journal of neurophysiology* 99.4 (2008), pp. 1871–1883.

[160] Pauli Virtanen et al. “SciPy 1.0: fundamental algorithms for scientific computing in Python”. In: *Nature methods* 17.3 (2020), pp. 261–272.

[161] Linda Petzold. “Automatic selection of methods for solving stiff and nonstiff systems of ordinary differential equations”. In: *SIAM journal on scientific and statistical computing* 4.1 (1983), pp. 136–148.

[162] Henry D. I. Abarbanel, Mark Kostuk, and William Whartenby. “Data assimilation with regularized nonlinear instabilities”. In: *Quarterly Journal of the Royal Meteorological Society* 136.648 (2010), pp. 769–783.

[163] A. N. Tikhonov. “On the stability of inverse problems”. In: *Doklady Akademii Nauk SSSR* 39 (1943), pp. 195–198.

[164] Andrew White et al. “The limitations of model-based experimental design and parameter estimation in sloppy systems”. In: *PLoS computational biology* 12.12 (2016), e1005227.

[165] J. B. Johnson. “Thermal agitation of electricity in conductors”. In: *Phys. Rev.* 32 (1928), p. 97.

[166] H. Nyquist. “Thermal agitation of electric charge in conductors”. In: *Phys. Rev.* 32 (1928), p. 110.

[167] Andreas Wächter and Lorenz T Biegler. “On the implementation of an interior-point filter line-search algorithm for large-scale nonlinear programming”. In: *Mathematical programming* 106.1 (2006), pp. 25–57.

[168] Eric Blayo et al. *Advanced data assimilation for geosciences: Lecture notes of the Les Houches school of Physics: Special Issue.* Oxford University Press, 2012.

[169] I. Hoteit. “A reduced-order simulated annealing approach for four-dimensional variational data assimilation in meteorology and oceanography”. In: *International journal for numerical methods in fluids* 58 (2008), p. 1181.

[170] Eve Marder et al. “Memory from the dynamics of intrinsic membrane currents”. In: *Proc. Nat. Acad. Sci.* 93 (1996), pp. 13481–13486.

[171] Tim Sauer, James A. Yorke, and Martin Casdagli. “Embedology”. In: *Journal of Statistical Physics* 65 (1991), p. 579.

[172] Ori Hillel, Eve Marder, and Shimon Marom. “Cellular function given parametric variation in the Hodgkin and Huxley model of excitability”. In: *Proc. Nat. Acad. Sci.* 115 (2018), E8211.

[173] Dahlia Kushinsky, Ekaterina Morozova, and Eve Marder. “In-vivo effects of temperature on the heart and pyloric rhythms in the crab Cancer borealis”. In: *Journal of Experimental Biology* 222 (2019), jeb199190.

[174] Nikolaus Kriegeskorte and Pamela K Douglas. “Cognitive computational neuroscience”. In: *Nature neuroscience* 21.9 (2018), pp. 1148–1160.

[175] F Gregory Ashby and Vivian V Valentin. “Computational cognitive neuroscience: Building and testing biologically plausible computational models of neuroscience, neuroimaging, and behavioral data”. In: *Statistical and process models for cognitive neuroscience and aging* (2007), pp. 15–58.

[176] Giacomo Indiveri et al. “Neuromorphic silicon neuron circuits”. In: *Frontiers in neuroscience* 5 (2011), p. 73.

[177] Carver Mead. “How we created neuromorphic engineering”. In: *Nature Electronics* 3.7 (2020), pp. 434–435.

[178] Rodney Douglas, Misha Mahowald, and Carver Mead. “Neuromorphic analogue VLSI”. In: *Annual review of neuroscience* 18.1 (1995), pp. 255–281.

[179] Carver Mead. “Neuromorphic electronic systems”. In: *Proceedings of the IEEE* 78.10 (1990), pp. 1629–1636.

[180] R Jacob Vogelstein et al. “Dynamically reconfigurable silicon array of spiking neurons with conductance-based synapses”. In: *IEEE transactions on neural networks* 18.1 (2007), pp. 253–265.

[181] Elisabetta Chicca, Giacomo Indiveri, and Rodney Douglas. “An adaptive silicon synapse”. In: *Proceedings of the 2003 International Symposium on Circuits and Systems, 2003. ISCAS’03.* Vol. 1. IEEE. 2003, pp. I–I.

[182] Michael A Arbib. “Brains, machines and buildings: towards a neuromorphic architecture”. In: *Intelligent Buildings International* 4.3 (2012), pp. 147–168.

[183] Abdullah M Zyarah and Dhireesha Kudithipudi. “Neuromorphic architecture for the hierarchical temporal memory”. In: *IEEE Transactions on Emerging Topics in Computational Intelligence* 3.1 (2019), pp. 4–14.

[184] Yoeri van De Burgt et al. “Organic electronics for neuromorphic computing”. In: *Nature Electronics* 1.7 (2018), pp. 386–397.

[185] Jacob Torrejon et al. “Neuromorphic computing with nanoscale spintronic oscillators”. In: *Nature* 547.7664 (2017), pp. 428–431.

[186] Yongtae Kim, Yong Zhang, and Peng Li. “A digital neuromorphic VLSI architecture with memristor crossbar synaptic array for machine learning”. In: *2012 IEEE International SOC Conference*. IEEE. 2012, pp. 328–333.

[187] Kaushik Roy, Akhilesh Jaiswal, and Priyadarshini Panda. “Towards spike-based machine intelligence with neuromorphic computing”. In: *Nature* 575.7784 (2019), pp. 607–617.

[188] Evgeny Katz. “Implantable bioelectronics–editorial introduction”. In: *Implantable bioelectronics. Wiley, Weinheim. https://doi. org/10* 1002.9783527673148 (2014).

[189] Emre Neftci et al. “A systematic method for configuring VLSI networks of spiking neurons”. In: *Neural computation* 23.10 (2011), pp. 2457–2497.

[190] Shaul Druckmann et al. “A novel multiple objective optimization framework for constraining conductance-based neuron models by experimental data”. In: *Frontiers in neuroscience* 1 (2007), p. 1.

[191] Nathan F Lepora, Paul G Overton, and Kevin Gurney. “Efficient fitting of conductance-based model neurons from somatic current clamp”. In: *Journal of computational neuroscience* 32.1 (2012), pp. 1–24.

[192] Pierre Baldi, Michael C Vanier, and James M Bower. “On the use of Bayesian methods for evaluating compartmental neural models”. In: *Journal of Computational Neuroscience* 5.3 (1998), pp. 285–314.

[193] Ulrich Parlitz and Christian Merkwirth. “Prediction of spatiotemporal time series based on reconstructed local states”. In: *Physical review letters* 84.9 (2000), p. 1890.

[194] Jun Wang et al. “Assimilation of biophysical neuronal dynamics in neuromorphic VLSI”. In: *IEEE Trans. on Biomed. Circ.* 11 (2017), p. 1258.

[195] Laure Buhry, Michele Pace, and Sylvain Saighi. “Global parameter estimation of an Hodgkin–Huxley formalism using membrane voltage recordings: application to neuro-mimetic analog integrated circuits”. In: *Neurocomputing* 81 (2012), pp. 75–85.

[196] Christof Rasche and Rodney Douglas. “An improved silicon neuron”. In: *Analog integrated circuits and signal processing* 23.3 (2000), pp. 227–236.

[197] Safieddine Bouali. “A 3D Strange Attractor with a Distinctive Silhouette. The Butterfly Effect Revisited”. In: *arXiv preprint arXiv:1311.6128* (2013).

[198] EDUARDO N Warman, DOMINIQUE M Durand, and GL Yuen. “Reconstruction of hippocampal CA1 pyramidal cell electrophysiology by computer simulation”. In: *Journal of Neurophysiology* 71.6 (1994), pp. 2033–2045.

[199] HJMWWJ Karst, M Joels, and WJ Wadman. “Low-threshold calcium current in dendrites of the adult rat hippocampus”. In: *Neuroscience letters* 164.1-2 (1993), pp. 154–158.

[200] SM Thompson and RK Wong. “Development of calcium current subtypes in isolated rat hippocampal pyramidal cells.” In: *The Journal of physiology* 439.1 (1991), pp. 671–689.

[201] TJ Ashwood, B Lancaster, and HV Wheal. “Intracellular electrophysiology of CA1 pyramidal neurones in slices of the kainic acid lesioned hippocampus of the rat”. In: *Experimental brain research* 62.1 (1986), pp. 189–198.

[202] Ning Gu et al. “Kv7/KCNQ/M and HCN/h, but not KCa2/SK channels, contribute to the somatic medium after-hyperpolarization and excitability control in CA1 hippocampal pyramidal cells”. In: *The Journal of physiology* 566.3 (2005), pp. 689–715.

[203] D. A. McCormick and H. -C. Pape. “Properties of a hyperpolarization-activated cation current and its role in rhythmic oscillation in thalamic relay neurons”. In: *J. Physiol. Lond.* 431 (1990), p. 291.

[204] Cuiyong Yue et al. “Proximal persistent Na+ channels drive spike afterdepolarizations and associated bursting in adult CA1 pyramidal cells”. In: *Journal of Neuroscience* 25.42 (2005), pp. 9704–9720.

[205] Christopher A Del Negro et al. "Sodium and calcium current-mediated pacemaker neurons and respiratory rhythm generation". In: *Journal of Neuroscience* 25.2 (2005), pp. 446–453.

[206] Erin L O'Callaghan et al. "Enhancing respiratory sinus arrhythmia increases cardiac output in rats with left ventricular dysfunction". In: *The Journal of Physiology* 598.3 (2020), pp. 455–471.

[207] Filippo Grassia et al. "Tunable neuromimetic integrated system for emulating cortical neuron models". In: *Frontiers in NEUROSCIENCE* 5 (2011), p. 134.

[208] Jun Wang et al. "Assimilation of biophysical neuronal dynamics in neuromorphic VLSI". In: *IEEE Transactions on Biomedical Circuits and Systems* 11.6 (2017), pp. 1258–1270.

[209] Chi-Sang Poon and Kuan Zhou. "Neuromorphic silicon neurons and large-scale neural networks: challenges and opportunities". In: *Frontiers in neuroscience* 5 (2011), p. 108.

[210] Philipp Vetter, Arnd Roth, and Michael Häusser. "Propagation of action potentials in dendrites depends on dendritic morphology". In: *Journal of neurophysiology* 85.2 (2001), pp. 926–937.

[211] Greg Stuart et al. "Action potential initiation and backpropagation in neurons of the mammalian CNS". In: *Trends in neurosciences* 20.3 (1997), pp. 125–131.

[212] C Bernard and D Johnston. "Distance-dependent modifiable threshold for action potential back-propagation in hippocampal dendrites". In: *Journal of neurophysiology* 90.3 (2003), pp. 1807–1816.

[213] Jeffrey C Magee and Daniel Johnston. "A synaptically controlled, associative signal for Hebbian plasticity in hippocampal neurons". In: *Science* 275.5297 (1997), pp. 209–213.

[214] Y Kawaguchi and Y Kubota. "Neurochemical features and synaptic connections of large physiologically-identified GABAergic cells in the rat frontal cortex". In: *Neuroscience* 85.3 (1998), pp. 677–701.

[215] Hua Hu, Jian Gan, and Peter Jonas. “Fast-spiking, parvalbumin+ GABAergic interneurons: From cellular design to microcircuit function”. In: *Science* 345.6196 (2014).

[216] Erika E Fanselow and Barry W Connors. “The roles of somatostatin-expressing (GIN) and fast-spiking inhibitory interneurons in UP-DOWN states of mouse neocortex”. In: *Journal of neurophysiology* 104.2 (2010), pp. 596–606.

[217] Alan Chow et al. “K+ channel expression distinguishes subpopulations of parvalbumin-and somatostatin-containing neocortical interneurons”. In: *Journal of Neuroscience* 19.21 (1999), pp. 9332–9345.

[218] Takaichi Fukuda and Toshio Kosaka. “Gap junctions linking the dendritic network of GABAergic interneurons in the hippocampus”. In: *Journal of Neuroscience* 20.4 (2000), pp. 1519–1528.

[219] Gábor Tamás, Peter Somogyi, and Eberhard H Buhl. “Differentially interconnected networks of GABAergic interneurons in the visual cortex of the cat”. In: *Journal of neuroscience* 18.11 (1998), pp. 4255–4270.

[220] Barry W Connors. “Synchrony and so much more: Diverse roles for electrical synapses in neural circuits”. In: *Developmental neurobiology* 77.5 (2017), pp. 610–624.

[221] Abraham R Schneider, Timothy J Lewis, and John Rinzel. “Effects of correlated input and electrical coupling on synchrony in fast-spiking cell networks”. In: *Neurocomputing* 69.10-12 (2006), pp. 1125–1129.

[222] Carmen C Canavier et al. “Control of multistability in ring circuits of oscillators”. In: *Biological cybernetics* 80.2 (1999), pp. 87–102.

[223] Gábor Tamás et al. “Input and frequency-specific entrainment of postsynaptic firing by IPSPs of perisomatic or dendritic origin”. In: *European Journal of Neuroscience* 20.10 (2004), pp. 2681–2690.

[224] Pascal Fries. “Neuronal gamma-band synchronization as a fundamental process in cortical computation”. In: *Annual review of neuroscience* 32 (2009), pp. 209–224.

[225] Shane Lee and Stephanie R Jones. “Distinguishing mechanisms of gamma frequency oscillations in human current source signals using a computational model of a laminar neocortical network”. In: *Frontiers in human neuroscience* 7 (2013), p. 869.

[226] Christoph Börgers, Steven Epstein, and Nancy J Kopell. “Background gamma rhythmicity and attention in cortical local circuits: a computational study”. In: *Proceedings of the National Academy of Sciences* 102.19 (2005), pp. 7002–7007.

[227] Christoph Börgers and Nancy Kopell. “Synchronization in networks of excitatory and inhibitory neurons with sparse, random connectivity”. In: *Neural computation* 15.3 (2003), pp. 509–538.

[228] Alain Destexhe et al. “A model of spindle rhythmicity in the isolated thalamic reticular nucleus”. In: *Journal of neurophysiology* 72.2 (1994), pp. 803–818.

[229] Nancy Kopell and Bard Ermentrout. “Chemical and electrical synapses perform complementary roles in the synchronization of interneuronal networks”. In: *Proceedings of the National Academy of Sciences* 101.43 (2004), pp. 15482–15487.

[230] Timothy J Lewis and John Rinzel. “Dynamics of spiking neurons connected by both inhibitory and electrical coupling”. In: *Journal of computational neuroscience* 14.3 (2003), pp. 283–309.

[231] M Rabinovich et al. “Dynamical encoding by networks of competing neuron groups: winnerless competition”. In: *Physical review letters* 87.6 (2001), p. 068102.

[232] Henri Korn and Philippe Faure. “Is there chaos in the brain? II. Experimental evidence and related models”. In: *Comptes rendus biologies* 326.9 (2003), pp. 787–840.

[233] Le Zhao and Alain Nogaret. “Experimental observation of multistability and dynamic attractors in silicon central pattern generators”. In: *Physical Review E* 92.5 (2015), p. 052910.

[234] Chiara Bartolozzi and Giacomo Indiveri. "Synaptic dynamics in analog VLSI". In: *Neural computation* 19.10 (2007), pp. 2581–2603.

[235] Gary W Johnson. *LabVIEW graphical programming*. Tata McGraw-Hill Education, 1997.

[236] Cleve B Moler. *Numerical computing with MATLAB*. SIAM, 2004.

[237] Silvia Daun, Jonathan E Rubin, and Ilya A Rybak. "Control of oscillation periods and phase durations in half-center central pattern generators: a comparative mechanistic analysis". In: *Journal of computational neuroscience* 27.1 (2009), p. 3.

[238] Ronald L Calabrese. "Half-center oscillators underlying rhythmic movements". In: *Nature* 261 (1995), pp. 146–148.

[239] David A McCrea and Ilya A Rybak. "Organization of mammalian locomotor rhythm and pattern generation". In: *Brain research reviews* 57.1 (2008), pp. 134–146.

[240] Tiaza Bem and John Rinzel. "Short duty cycle destabilizes a half-center oscillator, but gap junctions can restabilize the anti-phase pattern". In: *Journal of Neurophysiology* 91.2 (2004), pp. 693–703.

[241] Anca Doloc-Mihu and Ronald L Calabrese. "A database of computational models of a half-center oscillator for analyzing how neuronal parameters influence network activity". In: *Journal of biological physics* 37.3 (2011), pp. 263–283.

[242] Carmen C Canavier, Fatma Gurel Kazanci, and Astrid A Prinz. "Phase resetting curves allow for simple and accurate prediction of robust N: 1 phase locking for strongly coupled neural oscillators". In: *Biophysical journal* 97.1 (2009), pp. 59–73.

[243] Wolfgang Klimesch. "The frequency architecture of brain and brain body oscillations: an analysis". In: *European Journal of Neuroscience* 48.7 (2018), pp. 2431–2453.

[244] Tomislav Stankovski et al. “Alterations in the coupling functions between cortical and cardio-respiratory oscillations due to anaesthesia with propofol and sevoflurane”. In: *Philosophical Transactions of the Royal Society A: Mathematical, Physical and Engineering Sciences* 374.2067 (2016), p. 20150186.

[245] Shuoguo Wang et al. “Short conduction delays cause inhibition rather than excitation to favor synchrony in hybrid neuronal networks of the entorhinal cortex”. In: *PLoS Comput Biol* 8.1 (2012), e1002306.

[246] Randall D Beer, Hillel J Chiel, and John C Gallagher. “Evolution and analysis of model CPGs for walking: II. General principles and individual variability”. In: *Journal of computational neuroscience* 7.2 (1999), pp. 119–147.

[247] Pierre Meyrand, John Simmers, and Maurice Moulins. “Construction of a pattern-generating circuit with neurons of different networks”. In: *Nature* 351.6321 (1991), pp. 60–63.

[248] Sharene D Bungay and Sue Ann Campbell. “Modelling a respiratory central pattern generator neuron in Lymnaea stagnalis”. In: *Can. Appl. Math. Quart* 17 (2009), pp. 283–291.

[249] EM Quinlan and AD Murphy. “Plasticity in the multifunctional buccal central pattern generator of Helisoma illuminated by the identification of phase 3 interneurons”. In: *Journal of neurophysiology* 75.2 (1996), pp. 561–574.

[250] Jian Jing and Klaudiusz R Weiss. “Neural Mechanisms of Motor Program Switching inAplysia”. In: *Journal of Neuroscience* 21.18 (2001), pp. 7349–7362.

[251] Peter T Morgan et al. “Interneuronal and peptidergic control of motor pattern switching in Aplysia”. In: *Journal of Neurophysiology* 87.1 (2002), pp. 49–61.

[252] Alvaro Lozano, Marcos Rodriguez, and Roberto Barrio. “Control strategies of 3-cell Central Pattern Generator via global stimuli”. In: *Scientific reports* 6.1 (2016), pp. 1–10.

[253] Pranay Goel and Bard Ermentrout. “Synchrony, stability, and firing patterns in pulse-coupled oscillators”. In: *Physica D: Nonlinear Phenomena* 163.3-4 (2002), pp. 191–216.

[254] Wulfram Gerstner et al. “Neural codes: firing rates and beyond”. In: *Proceedings of the National Academy of Sciences* 94.24 (1997), pp. 12740–12741.

[255] Alexander Borst and Frédéric E Theunissen. “Information theory and neural coding”. In: *Nature neuroscience* 2.11 (1999), pp. 947–957.

[256] Kenji Doya et al. *Bayesian brain: Probabilistic approaches to neural coding.* MIT press, 2007.

[257] Andreas S Tolias et al. “Recording chronically from the same neurons in awake, behaving primates”. In: *Journal of neurophysiology* 98.6 (2007), pp. 3780–3790.

[258] Marie Vandecasteele et al. “Large-scale recording of neurons by movable silicon probes in behaving rodents”. In: *JoVE (Journal of Visualized Experiments)* 61 (2012), e3568.

[259] Hiroyuki Nakahara and Shun-ichi Amari. “Information-geometric measure for neural spikes”. In: *Neural computation* 14.10 (2002), pp. 2269–2316.

[260] Kenway Louie and Matthew A Wilson. “Temporally structured replay of awake hippocampal ensemble activity during rapid eye movement sleep”. In: *Neuron* 29.1 (2001), pp. 145–156.

[261] Robert Gütig et al. “Learning input correlations through nonlinear temporally asymmetric Hebbian plasticity”. In: *Journal of Neuroscience* 23.9 (2003), pp. 3697–3714.

[262] John J Hopfield. “Pattern recognition computation using action potential timing for stimulus representation”. In: *Nature* 376.6535 (1995), pp. 33–36.

[263] Guo-qiang Bi and Mu-ming Poo. “Synaptic modifications in cultured hippocampal neurons: dependence on spike timing, synaptic strength, and postsynaptic cell type”. In: *Journal of neuroscience* 18.24 (1998), pp. 10464–10472.

[264] WB Levy and O Steward. "Temporal contiguity requirements for long-term associative potentiation/depression in the hippocampus". In: *Neuroscience* 8.4 (1983), pp. 791–797.

[265] Henry Markram et al. "Regulation of synaptic efficacy by coincidence of postsynaptic APs and EPSPs". In: *Science* 275.5297 (1997), pp. 213–215.

[266] Alain Nogaret and Alastair King. "Inhibition delay increases neural network capacity through stirling transform". In: *Physical Review E* 97.3 (2018), p. 030301.

[267] Daniel J Amit, Hanoch Gutfreund, and Haim Sompolinsky. "Storing infinite numbers of patterns in a spin-glass model of neural networks". In: *Physical Review Letters* 55.14 (1985), p. 1530.

[268] Attila Szucs et al. "Robust microcircuit synchronization by inhibitory connections". In: *Neuron* 61.3 (2009), pp. 439–453.

[269] Sten Grillner et al. "Microcircuits in action–from CPGs to neocortex". In: *Trends in neurosciences* 28.10 (2005), pp. 525–533.

[270] Gaurav Sharma et al. "Using an artificial neural bypass to restore cortical control of rhythmic movements in a human with quadriplegia". In: *Scientific reports* 6 (2016), p. 33807.

[271] David A Friedenberg et al. "Neuroprosthetic-enabled control of graded arm muscle contraction in a paralyzed human". In: *Scientific reports* 7.1 (2017), pp. 1–10.

[272] Eve Armstrong. "Statistical data assimilation for estimating electrophysiology simultaneously with connectivity within a biological neuronal network". In: *Physical Review E* 101.1 (2020), p. 012415.

[273] Zhengxing Wu, Junzhi Yu, and Min Tan. "CPG parameter search for a biomimetic robotic fish based on particle swarm optimization". In: *2012 IEEE International Conference on Robotics and Biomimetics (ROBIO)*. IEEE. 2012, pp. 563–568.

[274] Jeong-Jung Kim, Jun-Woo Lee, and Ju-Jang Lee. "Central pattern generator parameter search for a biped walking robot using nonparametric estimation based particle swarm optimization". In: *International Journal of Control, Automation and Systems* 7.3 (2009), pp. 447–457.

[275] Matthew J Moye and Casey O Diekman. "Data assimilation methods for neuronal state and parameter estimation". In: *The Journal of Mathematical Neuroscience* 8.1 (2018), p. 11.

[276] Xiao-Jing Wang and György Buzsáki. "Gamma oscillation by synaptic inhibition in a hippocampal interneuronal network model". In: *Journal of neuroscience* 16.20 (1996), pp. 6402–6413.

[277] Srisairam Achuthan and Carmen C Canavier. "Phase-resetting curves determine synchronization, phase locking, and clustering in networks of neural oscillators". In: *Journal of Neuroscience* 29.16 (2009), pp. 5218–5233.

[278] RO Dror et al. "A mathematical criterion based on phase response curves for stability in a ring of coupled oscillators". In: *Biological cybernetics* 80.1 (1999), pp. 11–23.

[279] J Guckenheimer. "Holmes P.(1983)". In: *Nonlinear oscillations, dynamical systems, and bifurcations of vector fields* (1988), pp. 92–102.

[280] Fernando Castanos and Alessio Franci. "The transition between tonic spiking and bursting in a six-transistor neuromorphic device". In: *2015 12th International Conference on Electrical Engineering, Computing Science and Automatic Control (CCE)*. IEEE. 2015, pp. 1–6.

[281] Charles F Stevens. "Quantal release of neurotransmitter and long-term potentiation". In: *Cell* 72 (1993), pp. 55–63.